LUMINESCENCE IN LITHIUM BORATES

DISSERTATION

Brant E. Kananen, Lieutenant Colonel, USA

AFIT- ENP-DS-17-S-027

DEPARTMENT OF THE AIR FORCE
AIR UNIVERSITY

AIR FORCE INSTITUTE OF TECHNOLOGY

Wright-Patterson Air Force Base, Ohio

AFIT- ENP-DS-17-S-027

LUMINESCENCE IN LITHIUM BORATES

DISSERTATION

Presented to the Faculty
Department of Engineering Physics
Graduate School of Engineering and Management
Air Force Institute of Technology
Air University
Air Education and Training Command
In Partial Fulfillment of the Requirements for the
Degree of Doctor of Philosophy

Brant E. Kananen, BS, MS
Lieutenant Colonel, USA

July 2017

AFIT- ENP-DS-17-S-027

LUMINESCENCE IN LITHIUM BORATES

Brant E. Kananen, BS, MS
Lieutenant Colonel, USA

Committee Membership:

John W. McClory, PhD
Chairman

Nancy C. Giles, PhD
Member

Benjamin Akers, PhD
Member

Eric M. Golden, PhD
Member

ADEDJI B. BADIRU, PhD
Dean, Graduate School of Engineering and Management

AFIT- ENP-DS-17-S-027

Abstract

Electron paramagnetic resonance, photoluminescence, photoluminescence excitation, thermoluminescence (TL), optically stimulated luminescence (OSL) and absorption spectrometry are used to identify and characterize point defects in single crystals of lithium tetraborate ($Li_2B_4O_7$) and lithium triborate (LiB_3O_5) doped with silver or copper, and explore the role of these point defects in luminescence. Previously unknown defects are identified in Ag-doped $Li_2B_4O_7$ including: lithium vacancy substitutional-silver-ion defect-pairs (hole trap); isolated lithium vacancies (hole trap); isolated oxygen vacancies (electron trap); interstitial-silver-ion substitutional-silver-ion defect pairs (electron trap); isolated interstitial silver ions (electron trap); and interstitial-silver-ion lithium-vacancy defect pairs (electron trap). Defect models are proposed for each new defect, and implications on defect models developed for previously known defects. The role of each defect in TL and OSL radiation dosimetry is examined.

Defects in Ag-doped LiB_3O_5 and Cu-doped LiB_3O_5 are identified including: two species of interstitial-silver-ions (electron traps); isolated-substitutional-silver-ion (hole trap); lithium vacancy substitutional-silver-ion defect pairs (hole trap); interstitial-silver-ion substitutional-silver-ion defect pairs (electron trap); a species of interstitial-copper-ion (electron trap); isolated-substitutional-copper-ion (hole trap); and lithium vacancy substitutional-copper-ion defect pairs (hole trap). The role of each of these defects in TL and OSL is examined. Based on this assessment, Ag-doped LiB_3O_5 is a promising TL and OSL dosimetry material while Cu-doped LiB_3O_5 is not.

AFIT- ENP-DS-17-S-027

Lele Ka Moa No Na Puali

Acknowledgments

I thank my advisor Dr. John McClory for his help and guidance in completing the work. Additionally, I thank the members of my committee Dr. Eric Golden, Dr. Benjamin Akers, and Dr. Nancy Giles for their help, and Mr. Greg Smith, Mr. Mike Ranft, and Mr. Eric Taylor for the assistance they gave me in completing my research. To Mr. John Hixenbaugh Semper Fitadas! A special thanks to Dr. Larry Halliburton for all the hours helping me understand EPR and the other techniques used, many sessions discussing results, and his invaluable guidance. To my fellow students, thanks, and congratulations. Lastly, to my wife and children you were right, I simply had to write down what came out of that machine.

Brant E. Kananen

Table of Contents

List of Figures

Figure Page

LUMINESCENCE IN LITHIUM BORATES

I. Introduction

Lithium borates, both lithium tetraborate single crystals ($Li_2B_4O_7$ or LTB) and lithium triborate single crystals (LiB_3O_5 or LBO), have non-linear optical character, and can expand the frequency range of laser sources [1, 2]. In this role, $Li_2B_4O_7$ and LiB_3O_5 are well studied and characterized. In recent years, $Li_2B_4O_7$ has also been studied as a possible thermally stimulated luminescence (TL) dosimeter, optically stimulated luminescence (OSL) dosimeter, and as a material suited for neutron detection [3-10]. It is important to note from the references that the incorporation of monovalent ions, Cu or Ag, into single crystals of $Li_2B_4O_7$ is critical to the efficient detection of radiation. What is not apparent from the references is how the incorporation of these two monovalent ions facilitates the detection of radiation thru TL or OSL. In other works, the incorporation sites of Ag and Cu into $Li_2B_4O_7$ is described, and the role the ions play in the TL process is generally assessed [11-14]. There is need to develop a more subtle understanding of the role of these ions in the TL process, as well as to explore the role of these ions in the OSL process.

Likewise, there has been some study of the mechanism of thermally stimulated luminescence in LiB_3O_5 [15-18], although it has not been studied as extensively as $Li_2B_4O_7$. In any scheme to detect radiation, understanding the specific mechanisms which facilitate detection is fundamental to optimizing device performance and to enable the identification of radiation type in a mixed radiation environment. Characterizing intrinsic and extrinsic point defects is necessary to understand the TL and OSL mechanisms in these oxide crystals. Identifying the role of each defect, as transient or long-lived electron or hole traps, provides the knowledge necessary to begin optimization of growth processes in order to produce the most efficient materials for radiation detection.

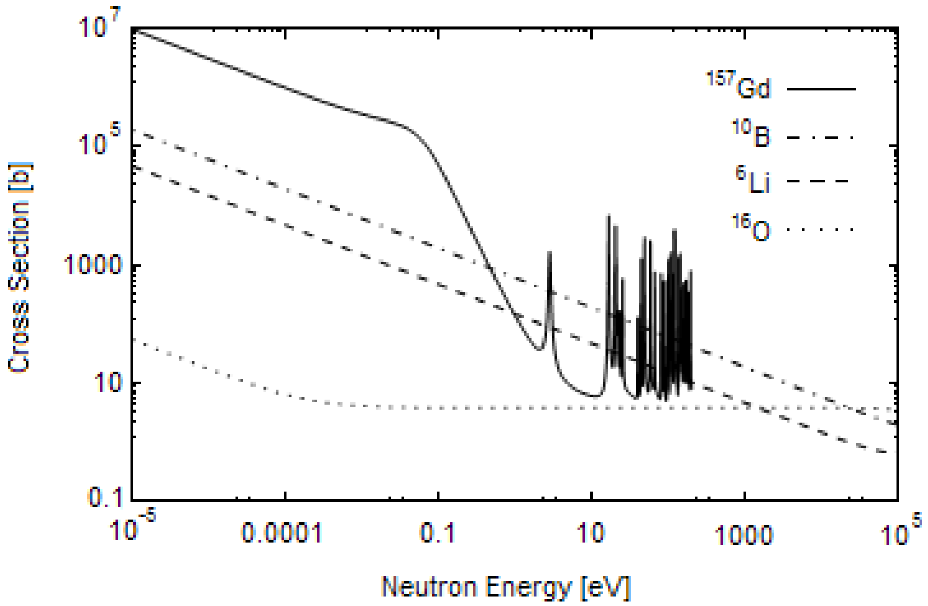

Figure 1. Neutron absorption cross-sections for selected isotopes. ^{157}Gd is not present in LTB or LBO crystals. It is included for comparison. ^{6}Li and ^{10}B have cross-sections over two orders of magnitude larger than ^{16}O for thermal neutron (~0.0258 eV). Plot data taken from ENDF data from the NNDC [19].

In addition, $Li_2B_4O_7$ and LiB_3O_5 are both potential candidates for neutron detection due to the presence of lithium and boron in each crystal. More specifically, the ^{6}Li and ^{10}B isotopes have large thermal neutron absorption cross sections as shown in Figure 1, and the (n,α) reaction for both ^{6}Li and ^{10}B are exothermic with the excess energy of reaction available as detectable kinetic energy in the resulting ^{3}H, α, and ^{7}Li particles as shown in equations 1 and 2.

$$^{6}\text{Li} + \text{n} \rightarrow\ ^{3}\text{H} + \alpha + 4.78\ \text{MeV} \qquad (1)$$

$$^{10}\text{B} + \text{n} \rightarrow\ ^{7}\text{Li} + \alpha + 2.8\ \text{MeV} \qquad (2)$$

Figure 1 shows the relative probability of neutron absorption by ^{6}Li and ^{10}B compared to other nuclei available in un-doped $Li_2B_4O_7$ or un-doped LiB_3O_5 (^{7}Li, ^{11}B, ^{17}O and ^{18}O have similar cross sections as ^{16}O). Note that the cross sections for neutron absorption by ^{6}Li (7.5 % abundant) and ^{10}B (19.9 % abundant) are quite large compared to other isotopes present in $Li_2B_4O_7$ or LiB_3O_5, and therefore they efficiently convert thermal neutrons into more readily detectable particles and energy.

Both $Li_2B_4O_7$ and LiB_3O_5 have potential as dosimetry materials. This work focuses on evaluating the utility of these two materials for use in radiation detection and dosimetry. The approach taken is not to quantify the material response to interaction with ionizing radiation, but to identify the point defects responsible for potential detection mechanisms. This approach demands a greater understanding of the fundamental properties of each material and how those properties facilitate the TL and OSL processes. The specific research goals are as follows: Identify the point defects responsible for high temperature TL in Ag-doped $Li_2B_4O_7$; Identify the point defects responsible for OSL in Ag-doped $Li_2B_4O_7$; Identify the extrinsic point defects caused by copper doping LiB_3O_5; Identify the point defects responsible for TL in Cu-doped LiB_3O_5; Identify the extrinsic point defects caused by silver doping LiB_3O_5; and Identify the point defects responsible for TL in Ag-doped LiB_3O_5.

In this work, chapter II describes a method used to gauge the effect of thermal quenching on photoluminescence. After chapter II, all chapters are prepared as publishable work according to the standards of the Journal of Luminescence in accordance with the Style Guide for AFIT Dissertations, Thesis and Graduate Research Papers dated July 2015. The chapters are presented not in the chronological order of publication, rather they are ordered to facilitate a logical flow of reading assuming the reader is familiar with the subject matter, but has not reviewed all previously published material. Chapter IV is already published in the Journal of Luminescence describing the point defects principally responsible for optically stimulated luminescence in Ag-doped $Li_2B_4O_7$. Chapter VI concerning the role point defects play in thermoluminescence in Cu-doped LiB_3O_5 is currently under review for publication in the Journal of Luminescence. Chapters III, V and VII have not yet been submitted for publication. Chapter III reviews and reexamines intrinsic defects in $Li_2B_4O_7$, identifies variations on those intrinsic defects in Ag and Cu doped $Li_2B_4O_7$, proposes defect models, and identifies the thermal stability of all previously unknown defects. Chapter V identifies two new silver related electron traps in Ag-doped $Li_2B_4O_7$ and proposes defect models for both of these two new traps as well as the one previously reported Ag related electron trap. The chapter also details the role of all point defects in Ag-doped $Li_2B_5O_7$ in the thermoluminescence process above room temperature. Chapter VII is analogous to Chapter VI, but the subject is Ag-doped LiB_3O_5.

II. Gauging thermal quenching of photoluminescence

Luminescence is the process by which a material emits longer wavelength light (Stoke Shift) when exposed to incident radiation [20]. The identifying name of the type incident radiation is used as a prefix to the word “luminescence” to identify the excitation source. As examples, x-ray-luminescence is emission of light upon exposure to x ray radiation and radioluminescence is emission of light upon exposure to nuclear radiation. When the incident radiation is optical or ultra-violet photons, the luminescence is called photoluminescence. Figure 2 shows a configuration coordinate diagram for the photoluminescence process. The lower curve is the ground state for an atomic electron, and the upper curve is an excited state. Photons excite the electron from the ground state at point A to the excited state, point B. Through release of phonons to the material lattice, the electron loses energy from point B to point C. The electron then returns to the ground state transitioning from point C to point D by emission of a photon of lower energy than the exciting photon. Again, the electron loses energy to the lattice via phonons and returns from point D to point A. The process may be repeated by absorption of another exciting photon [21].

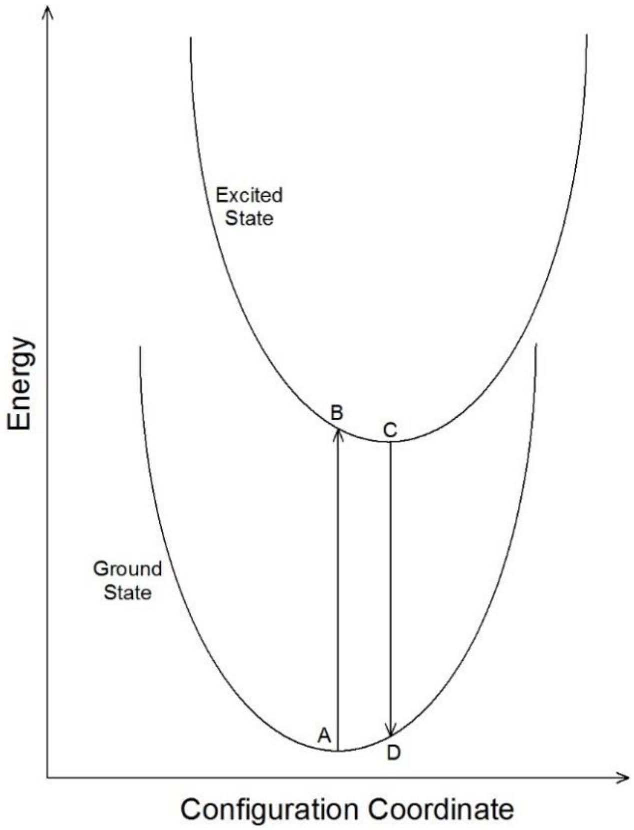

Figure 2. Photoluminescence configuration coordinate diagram.

Thermoluminescence differs from photoluminescence in several ways. Thermoluminescence requires thermal stimulation to release electrons trapped at material defects to facilitate recombination with holes trapped at separate defects. Upon excitation of an electron by a radiation interaction the electron is elevated to an excited state and a hole is created in the ground state as shown in Figure 3, and the process of releasing phonons and photons to return to the ground state is the same as described for photoluminescence. However, thermal stimulation is required due to the trapping of the electrons and holes in material defects.

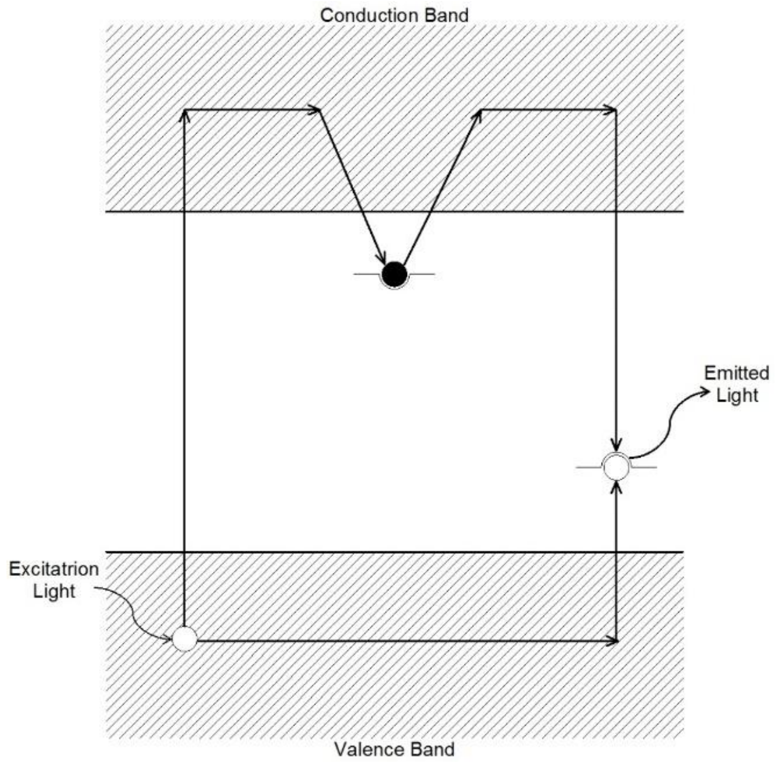

Figure 3. Thermoluminescence diagram.

Figure 3 shows a diagram of the thermoluminescence process in the one trap-one recombination center model. Ionizing radiation creates an electron-hole pair which may recombine immediately, or travel through the conduction band (electrons) and valence band (holes) and become trapped at material defects (Figure 3 shows an electron trap as a black circle and a hole trap as an open circle). If the traps are far enough in energy from the conduction and valence bands that room temperature thermal energy cannot free them, the charges remain trapped until thermal stimulation is provided to de-trap the electron or hole. In thermoluminescence, heat is used to stimulate the electron out of the electron trap. Once released to the conduction band, the electron recombines with the hole at the hole trap (luminescence center). The recombination of electron and hole frequently leaves the electron in an excited energy state, point B in Figure 2. The light emission continues via the same process described for photoluminescence [22-24].

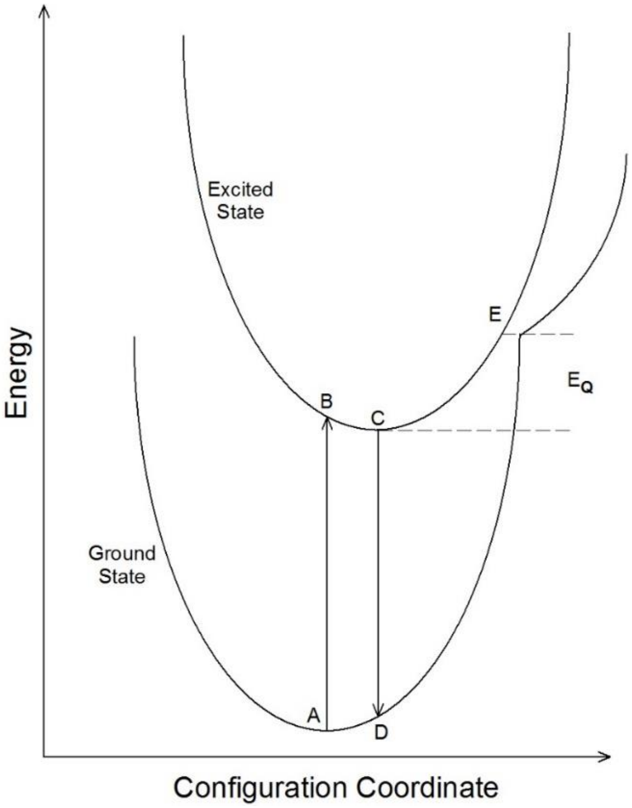

Figure 4. Thermal quenching of photoluminescence configuration coordinate diagram.

One of the limitations to thermoluminescence output is the phenomenon of thermal quenching of photoluminescence [21, 25-27]. The very thermal energy that is used to stimulate the release of trapped electrons inhibits the light emission of the luminescence center. Figure 4 displays a configuration coordinate diagram for the quenching of photoluminescence. The process by which photoluminescence absorbs photons and emits photons of lower energy is unchanged from the process describe in Figure 2. The difference in the quenching process is the proximity of the ground to excited states located at point E. At point E an electron in the excited state may return to the ground state by emitting a phonon instead of a photon. The electron then returns to the low energy point in the ground state, point A, via release of additional phonons. Note that point E is higher in energy than point C by E_Q. E_Q represents the thermal energy required to quench the release of photons. The stimulating heat used in thermoluminescence, inhibits the light emission process at sufficiently high temperatures. Optically stimulated luminescence does not share this limitation as heat is not the stimulation energy source [28].

In order to measure the quenching of photoluminescence, a photo luminescent material must be continually excited while under controlled heating, and the intensity of light emission recorded as a function of material temperature. A Horiba Fluorolog-3 spectrometer operating in kinetics mode was used to excite photoluminescence as well as detect the intensity of emitted light. This spectrometer has a xenon lamp as the excitation source, two double-grating monochromators to measure emission and excitation spectra, and a Hamamatsu R928 photomultiplier as a detector. An Instec HCS621G stage was used to control sample temperature. An ANDOR Shamrock 193i spectrograph coupled to an iDus 420 CCD camera was used to simultaneously detect the intensity and spectrum of emitted light.

Figure 5 shows a schematic of the spectrometer, stage, and sample alignment used to obtain photoluminescence quenching curves. The laboratory jack in Figure 5 was used to align the stage and sample with excitation light of the spectrometer. The block placed between the stage and the lab jack on the side away from the excitation light source was used to incline the thermal stage containing the sample toward the excitation light. Without inclination, the sample lies is a shadow cast by the lip of the stage casing. The inclination also ensures that light emitted from the sample passes over the same lip in the stage to the detecting lens of the detector.

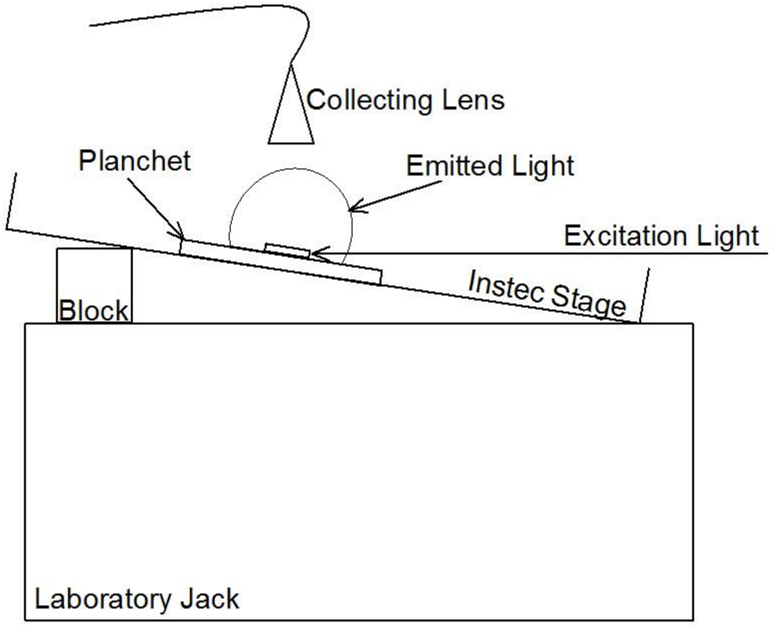

Figure 5. Schematic representation of device setup for gauging the thermal quenching of photoluminescence.

When placing the sample on the cooling/heating planchet of the Instec stage, maximum thermal coupling is ensured by placing the broadest face of the sample in direct contact with the planchet. Efforts to balance the sample on a narrow side on the planchet to reduce the required inclination provided inconsistent emission results due to the poor thermal coupling of sample to the planchet through the small area of contact. The sample also tends to fall over during heating.

In Figure 5 the collecting lens and fiber of the ANDOR spectrograph lies directly over the sample. This position yielded positive results, and was the easiest to mount and align. Placing the lens and fiber on the level of the sample off to one side at an angle perpendicular to the excitation light source also worked well, and allowed for the insertion of high or low pass filters between the sample and the collecting lens. Note that if the spectrometer is only being used to measure the intensity of the emitted light, the collecting lens and fiber may be eliminated from the setup.

Once the spectrometer (excitation light source), stage, spectrograph and sample are placed into position, the spectrometer, stage and spectrograph must be programed with experimental parameters. The stage must be set to hold the starting temperature. Then it must be programed to control the temperature of the sample from the starting temperature to the ending temperature at a desired heating rate. The heating rate should allow for sufficient time at each temperature to collect sufficient emitted light to optimize the signal-to-noise ratio. If an analysis of hysteresis is desired, the temperature may be ramped from the starting point to the high temperature end point, and then back to the starting point all while emitted light intensity is being monitored. Heating should not be started until the excitation light has been turned on, and collection of emitted light has commenced.

The spectrometer should be set for kinetics mode, and the input monochromator set to illuminate the sample with the desired excitation wavelength. The kinetics mode of the spectrometer operates the spectrometer at a fixed excitation wavelength and fixed detection wavelength for a fixed time. The length of the kinetics run should be set somewhat longer than the required collection time to allow time to turn on the spectrograph and start the heating of the sample. If the detection leg of the spectrometer is to be used to monitor the intensity of emitted light, then the detection monochromator of the spectrometer must be set to the wavelength of light emitted by the sample, and the duration of each collected data point must be set. The heating rate of the sample and the collection time of each data point should be synchronized. If a greater signal-to-noise ratio is required due to low light emission by the sample, the collection time for each data point should be lengthened and the heating rate slowed accordingly. Averaging several collections at each temperature can also improve the signal-to-noise ratio. Additionally, the excitation light should be turned on prior to turning on the spectrograph or initiating heating within the Instec stage.

The spectrograph must be set up similarly to the detection leg of the Flourolog. The range of wavelengths to be monitored, and the length of collecting time for each data point must be set. The same methods for improving signal-to-noise ratio may be used with the spectrograph as suggested for the spectrometer, ie. longer collection times per data point or averaging several data point; in either case with slower heating rates. Note, if background corrected data is to be collected with the spectrograph, then background data must be collected prior to turning on the excitation source.

A correlation of temperature and data point number for both the Instec stage to Flourolog spectrometer and the Instec to Shamrock spectrograph must be made at least once during collection. This is achieved by noting the stage temperature for one of the spectrograph data points. If a linear heating rate is used, this correlation will allow registration of the temperature to each collected data point. If the detection leg of the spectrometer is to be used to quantify emitted light, then care must be taken to shield the detection leg from any additional sources of light. The background light can be subtracted from spectrograph data as a part of the background, but the spectrometer) has no such capability.

III. Identification of $V_{Li} - Ag_{Li}^{+}$ defect pairs and isolated oxygen vacancies in $Li_2B_4O_7$:Ag with electron paramagnetic resonance

Abstract

Electron paramagnetic resonance (EPR) and thermoluminescence (TL) are used to identify and characterize $V_{Li}^{+} - Ag_{Li}^{2+}$ hole traps and isolated V_O^{-}electron traps in Ag-doped lithium tetraborate ($Li_2B_4O_7$) crystals. In as grown Ag-doped $Li_2B_4O_7$, Ag^+ ions substitute for Li^+ ions, and Ag^+ ions also occupy interstitial sites. Ag^+ ions substituting for Li^+ ions act as hole traps and interstitial Ag^+ ions act as electron traps when the crystal is exposed to ionizing radiation. The substitutional Ag^+ ions may be isolated from other defects in the crystal lattice, or they may pair with lithium vacancies. The $V_{Li} - Ag_{Li}^{+}$ defect pairs can, when exposed to ionizing radiation at 77 K, trap two holes forming $V_{Li}^{+} - Ag_{Li}^{2+}$ in which the holes trapped at both the V_{Li} and the holes trapped at the Ag_{Li} are more stable than holes trapped at either isolated defect. When exposed to ionizing radiation at room temperature, holes only trap at the substitutional Ag^+ ion forming $V_{Li} - Ag_{Li}^{2+}$ defects. In diffusion doped $Li_2B_4O_7$:Ag, oxygen vacancies with no other nearby defects form. When exposed to ionizing radiation, the isolated V_O traps an electron forming V_O^{-}. The electron trapped at the isolated oxygen vacancy is stable to 225 °C while electrons trapped at V_O perturbed by nearby Ag ions are only stable to near 75 °C.

1. Introduction

Silver doped lithium tetraborate ($Li_2B_4O_7$:Ag) crystals show potential for radiation dosimetry with intrinsic neutron sensitivity by either thermally stimulated luminescence (TL) or optically stimulated luminescence (OSL) [9,13,15-16,18, 29].

Enriching in either ^{6}Li or ^{10}B would increase sensitivity to thermal neutron interactions for the same quantity of material. In Ag doped $Li_2B_4O_7$, as grown or diffusion doped, Ag^+ ($4d^{10}$) occupies lithium sites and interstitial sites. When exposed to ionizing radiation at room temperature, interstitial silver ions trap an electron becoming Ag^0 silver atoms. These silver trapped electrons are stable up to approximately 150 °C [6,13], and may be optically released by near 400 nm light [30]. Whether released thermally or optically, subsequent recombination with holes yields TL and OSL light emission. Also during room temperature irradiation, the substitutional silver ions trap a hole becoming Ag^{2+} ($4d^9$), and forming one of two similar paramagnetic defects. One defect is in an otherwise defect free lattice (Ag_{Li}^{2+}) and one has a nearby perturbing defect. The angular dependence of the EPR spectra of both species of substitutional silver trapped holes and their role in thermoluminescence and optically stimulated luminescence has been established [6,13,30]. It has also been shown that the intrinsic oxygen vacancy serves as a short lived electron trap in Ag doped $Li_2B_4O_7$ [30].

In the present paper, we use electron paramagnetic resonance and thermoluminescence to show that the defect associated with the perturbed Ag_{Li}^{2+} is a nearby lithium vacancy, and that when exposed to ionizing radiation at 77 K the defect pair traps two holes forming an $S = 0$ spin system. The thermal stability of both trapped holes are explored, and a defect model for the $V_{Li} - Ag_{Li}^+$ defect pairs is proposed. Additionally, a model for a self-trapped hole, previously reported to be a lithium vacancy trapped hole [31], is proposed. Finally, a new highly stable isolated oxygen vacancy electron trap is identified in diffusion doped $Li_2B_4O_7$.

2. Experimental

Lithium tetraborate crystals have a tetragonal structure (space group I41cd) with a point group of 4mm. The lattice constants for the crystal, at room temperature, are a=9.475 Å and c=10.283 Å. There are two inequivalent boron sites and four inequivalent oxygen sites. All of the lithium sites are equivalent. There are 104 atoms in the unit cell organized in eight formula units. The formula units transform one to another in accordance with the symmetry of the crystal [32-35]. The basic repeating group, $(B_4O_9)^{6-}$, consists of two boron ions, B2, tetrahedrally coordinated by oxygen and two boron ions, B1, triangularly coordinated by oxygen [32]. Each of the oxygen ions is coordinated to two boron ions. Further, the boron-oxygen framework creates channels along the c-axis which are filled by LiO_4 polyhedra, in which, the O3 and O4 oxygen ions are coordinated by two lithium ions, and the O1 and O2 oxygen ions are coordinated by one lithium ion [34]. Figure 6 shows a crystal model of $Li_2B_4O_7$ consisting of two $(B_4O_9)^{6-}$ groups and two adjacent lithium ions.

The diffusion doped sample used for TL and EPR experiments was rectangular in shape with nominal dimensions of 3 mm along the a axes and 1.5 mm along the b axis. Silver was diffused into an undoped $Li_2B_4O_7$ crystal by wrapping a single crystal in silver foil (0.25 mm thick) and placing the wrapped crystal in one-zone tube furnace. The crystal was held at 870 °C for 11.5 h in a flowing nitrogen atmosphere. The melting point of $Li_2B_4O_7$ is 917 °C [36]. After diffusion, the crystal was rapidly cooled to room temperature. At the high temperature, silver enter the crystal as close-shelled singly ionized Ag^+ state and occupy Li^+ sites and interstitial spaces. It is not known if the silver dopant is uniformly distributed within the diffused crystal.

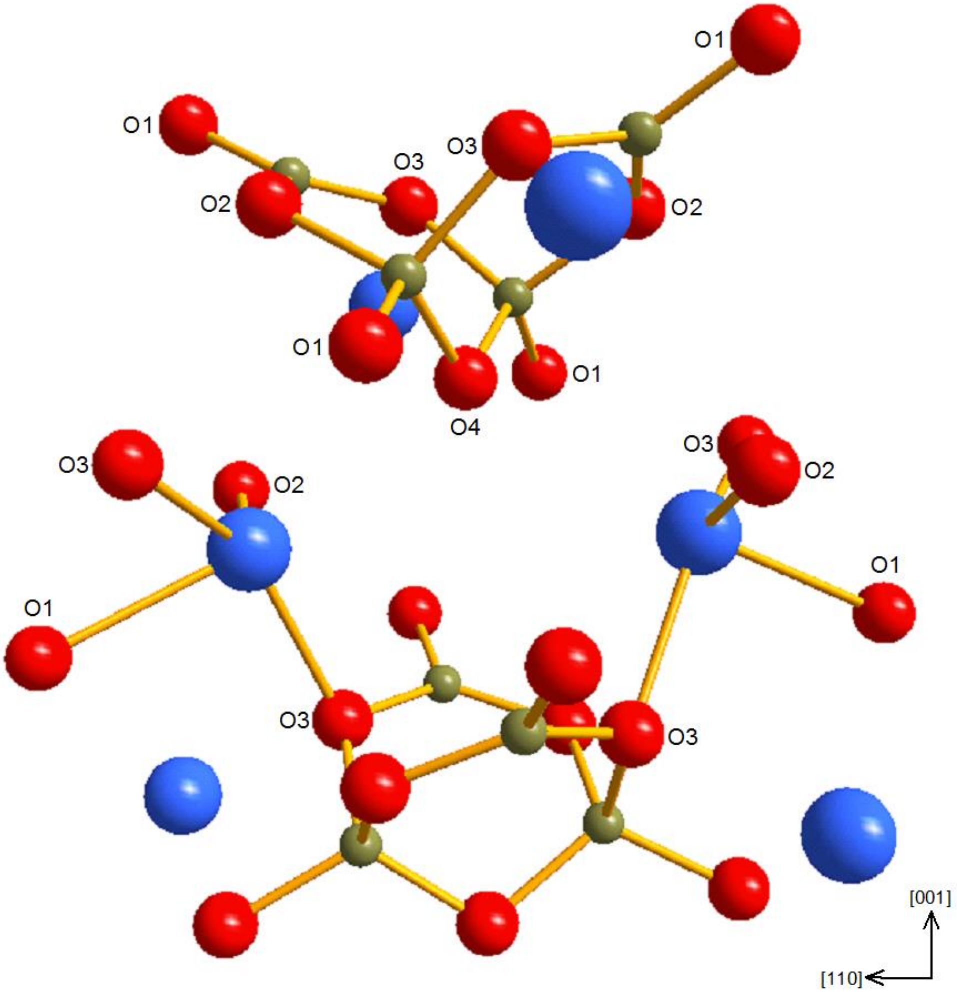

Figure 6. Ball and stick model of $Li_2B_4O_7$. The model contains two $(B_4O_9)^{6-}$ groups and six nearest lithium ions. Lithium ions are blue, boron ions are green, and oxygen ions are red.

As grown silver doped and copper doped crystals were cut from larger boules. The as grown silver doped crystal had nominal dimensions of 0.83 × 3 × 6.5 mm^3. The [001] direction was normal to the broad faces. The as grown copper doped crystal had nominal dimensions of 0.5 × 1.5 × 2.5 mm^3. The [001] direction was normal to the broad faces. The as grown doped samples was grown by the Czochralski method at the Institute of Physical Optics (L'viv, Ukraine). A congruent melt, exposed to air, was contained in a Pt crucible. The growth axis was [001] and the pulling and rotation velocities did not exceed 0.3 mm/h and 10 revolutions/min, respectively. The concentration of Ag in the Ag-doped sample is estimated, from the starting materials, to be 0.02 at. %. While the concentration of Cu in the Cu-doped sample is estimated, from starting materials, to be 0.015 at. %.

EPR data were collected using a Bruker EMX spectrometer operating near 9.4 GHz. An Oxford helium-gas flow system controlled the temperature of the sample and magnetic fields were measured using a Bruker teslameter. A proton NMR gaussmeter was used to obtain static magnetic field values, and a small Cr-doped MgO crystal was used to correct the magnetic field for the difference between the sample position and the position of the gaussmeter. Crystals where irradiated using a Varian OEG-67H x ray tube operating at 60 kV and 30 mA. Irradiation times were 3 min. A single zone furnace was used to heat irradiated crystals above room temperature. The furnace was heated to the annealing temperature and the crystal was inserted. After heating, the crystal was rapidly cooled to room temperature.

Interstitial defects are denoted with a subscript i and substitutional defects are denoted with a subscript Li or subscript O for defects at lithium or oxygen sites, respectively. Superscripts are used to denote the charge state of individual ions or defects when the superscript is adjacent to the ion or defect symbol. As an example, Ag_{Li}^{+}, is a 1+ silver ion on a lithium site. If the superscript is adjacent to a pair of defects inside square braces, then the superscript denotes the charge state of the defect pair relative to a defect free lattice. As an example, $[V_{Li}^{-} - Ag_{Li}^{+}]^{-}$ is a lithium vacancy 1− adjacent to a substitutional 1+ silver. The defect pair has a 1− charge state relative to a defect free lattice.

3. Results

Large concentrations of paramagnetic defects were produced in Ag-doped $Li_2B_4O_7$ single crystals, both as grown and silver diffused, with ionizing radiation (x rays). The x rays produce mobile electrons and holes in the $Li_2B_4O_7$ lattice. Most of these electrons and holes recombine immediately, but some are trapped at intrinsic and extrinsic defects in the crystal lattice.

3.1 $V_{Li} - Ag_{Li}$ Defect Pairs

When the as grown Ag-doped crystal in irradiated at 77 K, three holel-like centers and two electronlike centers are formed. Figure 7 shows each of these centers. The data was taken at 30 K with the magnetic field aligned parallel to the [001] direction of the crystal and a microwave frequency of 9.39 GHz. There is a doublet centered at 290 mT which is a hole trapped at an Ag^{+} located at a Li^{+} site in the crystal lattice forming a Ag^{2+} paramagnetic center [6]. The perturbed Ag^{2+} center is not observed when the crystal is irradiated at 77 K [13, 30]. There is also a seven line spectrum located at 335 mT which Swinney [31] identified as a hole trapped at the site of a lithium vacancy. Swinney identified that the hole traps at an oxygen atom, and the seven line hyperfine pattern is due to the equal interaction of two boron nuclei. The two 3/2+ spin boron nuclei create a 6+ spin system resulting in 7 equally spaced hyperfine lines, 2I +1, with intensity ratios of 1:2:3:4:3:2:1 [31]. It seems as likely now that this seven line spectrum is due to a hole trapped at an oxygen ion in an otherwise un-perturbed lattice, or a self-trapped hole. The third hole-like center is visible as a broad shoulder in the low field and high field sides of the self-trapped hole in Figure 7. There are also two electron-like centers, an Ag trapped electron consisting of 16 lines centered at 335 mT and an oxygen vacancy trapped electron consisting of 4 lines centered at 335 mT.

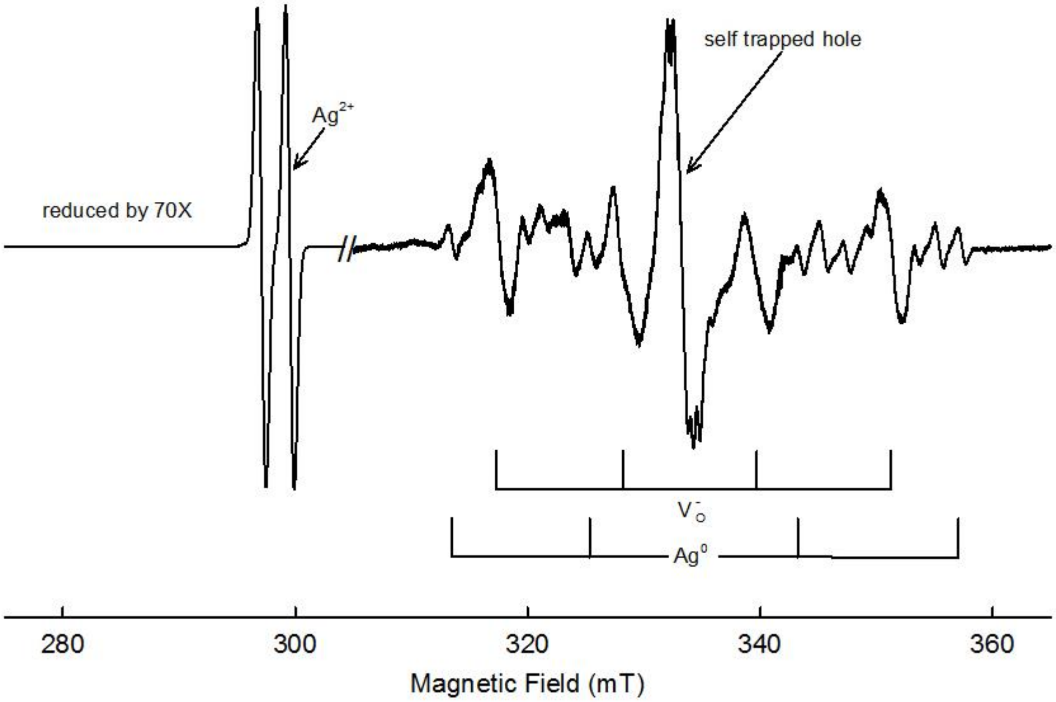

Figure 7. EPR spectrum showing isolated Ag^{2+} ions, self-trapped holes, electrons trapped at oxygen vacancies, and Ag^0 centers. The magnetic field was along the [001] direction and the microwave frequency was 9.39 GHz at 30 K. The isolated Ag^{2+} portion of the spectrum was reduced by 70 times.

Figure 8 Swinney reported the g-value for the trapped hole as 2.0116 (±0.0001), with an average separation between adjacent lines of 5.8 G. He further determined that the trapped holes became unstable near 90 K. He suggests that the hole is likely trapped on an O4 adjacent to a lithium vacancy and that the hole trapped in LiB_3O_5 described in reference [37] is analogous [31]. The low thermal stability of the trapped hole center, and the low thermal stability of the self-trapped hole in LiB_3O_7 [37], suggest that the trapped hole center described by Swinney may be a self-trapped hole in $Li_2B_4O_7$.

Figure 8 shows a model of a self-trapped hole in $Li_2B_4O_7$ localized on an O4 oxygen ion. The O4 oxygen ion is the only oxygen ion in $Li_2B_4O_7$ in which both coordinating boron ions are equivalent, B2, and the bond lengths between O4 ion and the two B2 ions are equal. As such, the interaction with each of the two B2 ions could be equal. All other oxygen sites have a short and long bond with the two coordinating boron ions, and would not likely have equal boron interactions. The distance from the O4 ion to adjacent lithium ions represents the greatest Li-O separation in the $Li_2B_4O_7$ crystal. Furthermore, the Li-O4 bond distance is equal for both lithium ions coordinating the O4 ion [34]. As shown in Figure 8, a p_z orbital containing the unpaired electron on the O4 ion aligned with the c-axis of the $Li_2B_4O_7$ crystal would be equidistant from the two coordinating B2 ions, and equidistant from the two coordinating lithium ions. This orientation gives equal interaction at the two coordinating boron sites, and gives the greatest separation between the trapped hole and neighboring positive ions reducing the total energy.

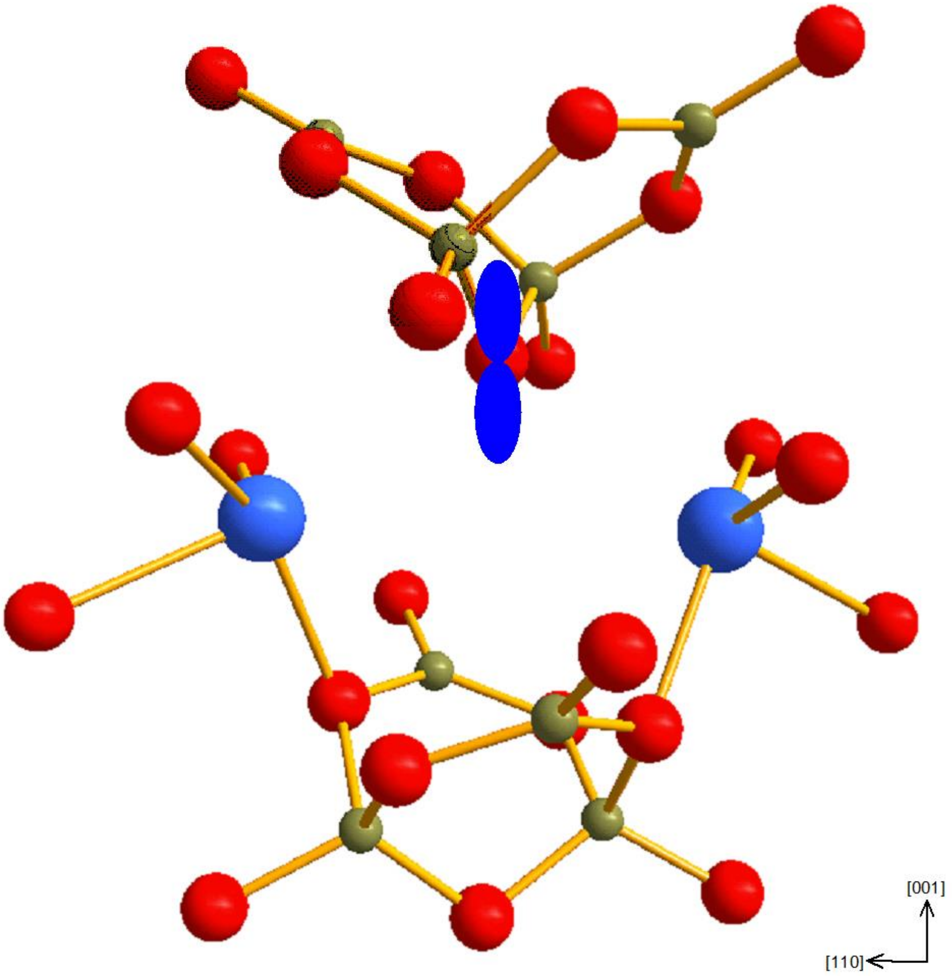

Figure 8. Model of the self-trapped hole in $Li_2B_4O_7$. During irradiation with ionizing x rays at 77 K, a hole is trapped at the O4 oxygen. Lithium ions are blue, boron ions are green, and oxygen ions are red.

Figure 9 (b) was taken after warming the crystal to 150 K while illuminating the crystal with 442 nm laser light and cooling it again to 30 K. The seven line self-trapped hole spectrum became unstable near 90 K, and completely disappeared by 100 K. A second spectrum appears at a slightly higher field position. Warming to 150 K without laser illumination and cooling back to 30 K eliminated the self-trapped hole spectrum, but does not produce the second spectrum. The new laser induced spectrum has a g-value of

2.0070 (±0.0001). This shifts the g-value higher than the free electron value of 2.0023 demonstrating that the spectrum is due to a trapped hole. The spectrum has a width of 2.013 mT. Further, the spectrum has some unresolved hyperfine structure. A similar lithium vacancy spectrum was reported for ^{6}Li enriched $^6Li_2B_4O_7$ after irradiation with fast neutrons [38]. In the case of the neutron-irradiated crystal, the lithium vacancies were stable at temperatures in excess of 100 °C. Lithium vacancies were either formed by knock-on damage caused by high energy neutrons, or by transmutation of Li thru the $^6Li(n,{}^3H)\alpha$ reaction outlined in Equation 1.

The laser induced hyperfine spectrum at 335 mT is likely a pair of adjacent defects, a lithium vacancy adjacent to a Ag^{1+} ion located on a lithium site, $[V_{Li} - Ag_{Li}]$. Prior to x ray irradiation, the defect pair traps no holes, and the substitutional silver is in the 1+ state, and the lithium vacancy is in the neutral state. The defect pair is, therefore, in the 1− state relative to the defect free crystal. When x ray irradiated at room temperature, a hole is trapped by the substitutional silver creating a perturbed Ag_{Li}^{2+}. This state of the defect has been well described previously [6, 13, 30, 39]. When the crystal is x ray irradiated at 77 K, two holes are trapped at the defect pair. The first hole is trapped on an oxygen ion coordinating the V_{Li}^{-} creating a V_{Li}^{0}, and the second hole is trapped on the substitutional silver creating a Ag_{Li}^{2+}. The defect pair being $[V_{Li}^{0} - Ag_{Li}^{2+}]^{+}$ is a net 1+ defect after trapping two holes. The hole trapped at the lithium vacancy is likely trapped on the coordinating oxygen most distant from the substitutional silver. If the V_{Li} and Ag_{Li} are on the two Li sites adjacent to a single O4 as depicted in Figure 10, the Li vacancy trapped hole would be present on a O1 ion, represented by the dashed box, and the distance between trapped holes would be 6.165 Å. This is the most distant, and most likely model. The unresolved hyperfine spectrum may result from the unequal bonds length between the O1 and its two boron neighbors, thereby creating unequal interactions.

An Ag^{2+} ion ($4d^9$) has one unpaired electron in the d-shell. As shown in Figure 10, the nearest five oxygen ions surround a substitutional Ag ion resulting in distorted trigonal bipyramidal symmetry. The two O3 and single O2 are in the xy plane representing the equatorial ligands, while the coordinating O1 and O4 ions represent the axial ligands. Crystal field theory estimates that the d_{z^2} orbital is the highest energy d orbital in trigonal bipyramidal symmetry [40, p. 405]. Therefore the trapped hole on the Ag^{2+} ion should be in this orbital. A slight shift of the d_{z^2} orbital away from the O4 toward the adjacent lithium vacancy in the $[V_{Li}{}^{-} - Ag_{Li}{}^{+}]^{-}$defect pair would nearly place the unpaired spin along the [110] direction of the crystal. This also, by symmetry, places other distinguishable orientations of the d_{z^2} Ag^{2+} orbital nearly aligned with the [−110]. This orientation of the trapped hole agrees with the angular dependence of the $[V_{Li}{}^{-} - Ag_{Li}{}^{2+}]^{0}$ trapped hole reported by Buchanan [13]. The d_{z^2} orbital of the four distinguishable orientations of the $[V_{Li}{}^{-} - Ag_{Li}{}^{2+}]^{0}$ site would all lie in the (001) plane of the crystal. Aligning the unpaired spin in the d_{z^2} orbital parallel with the applied magnetic field would yield the lowest g value which is evident in Buchanan’s work [13].

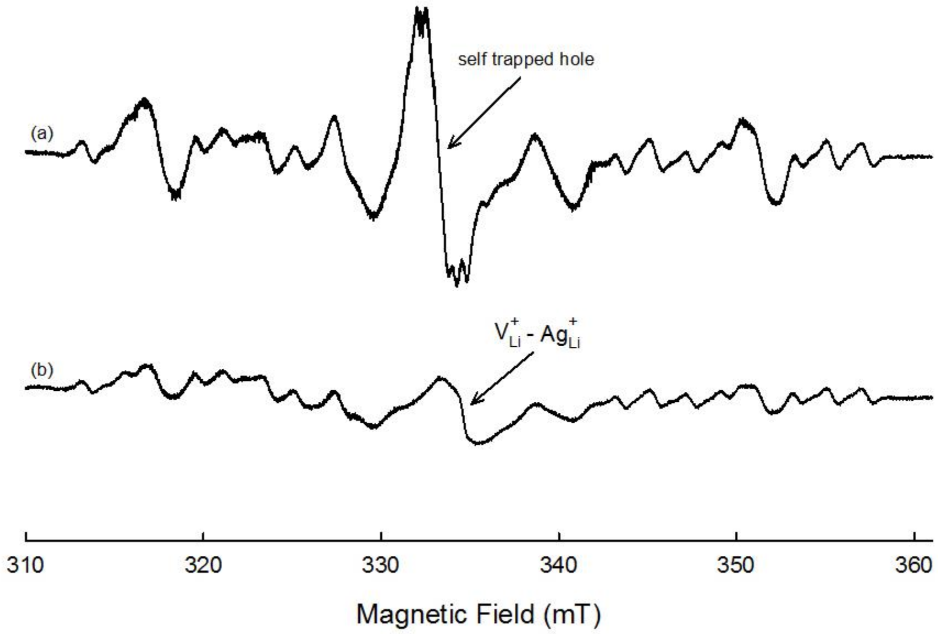

Figure 9. EPR spectrum of self-trapped holes and holes trapped at isolated lithium vacancies in $Li_2B_4O_7$. The magnetic field was along the [001] direction with a microwave frequency of 9.39 GHz at 30 K. (a) Spectrum taken after irradiation with x-rays at 77 K. (b) Spectrum taken after warming the crystal to 150 K while illuminating with 442 nm laser light and cooling again to 30 K.

If the V_{Li} and the Ag_{Li} are in closest coordination, at two adjacent Li sites in the LO_4 polyhedra wound along the c-axis, the hole could trap on either the O3 site or the O4 site. The O4 site would produce a seven line hyperfine spectrum much like the self-trapped hole. The O3 site coordinates with neighboring boron ions via two unequal bonds, thereby producing unequal hyperfine interactions from the two coordinating boron neighbors. The O3 site would not place the trapped hole in the d_z^2 orbital, and would therefore represent an excited state, which isunlikely. In either model, the pair of trapped holes could assume the singlet (S = 0) or triplet (S = 1) state. If in the singlet state, the pair of trapped holes would not be visible in the EPR spectrum. If in the triplet state, the pair of trapped holes might not be visible in the EPR spectrum. In the triplet state, the resulting spectrum created by two hole trapping sites with significantly different g values, hyperfine structure, and levels of covalence would be difficult to predict or recognize. If fact, the defect pair is not visible in the EPR spectrum when trapping two holes due to x ray irradiation at 77 K.

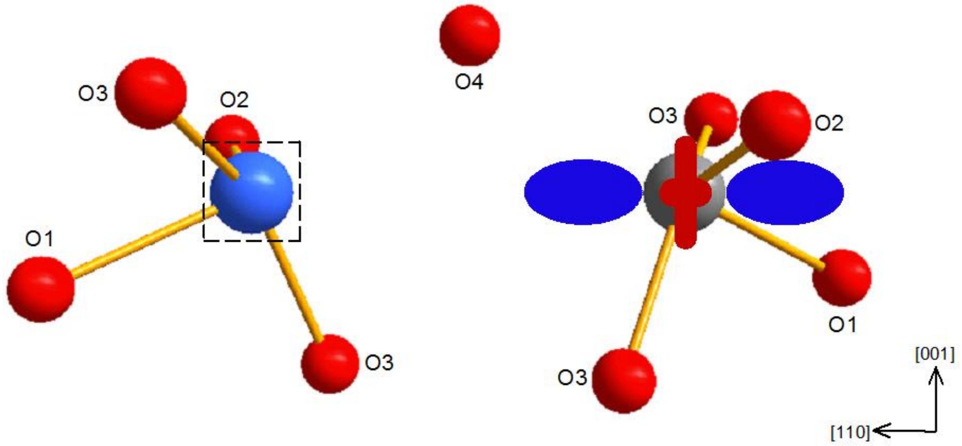

Figure 10. Model of a V_{Li}–Ag_{Li} defect pair. The lithium vacancy is in the dashed box. Lithium ions are blue, boron ions are green, oxygen ions are red, and the silver ion is grey.

The $[V_{Li}^{+} - Ag_{Li}^{2+}]^{2+}$ charge state of the defect is not stable at room temperature and therefore is not produced when the crystal is x ray irradiated at room temperature. Also, when the crystal is x ray irradiated at 77 K and then warmed, the hole trapped by the lithium vacancy is released as the temperature rises toward room temperature, and only the perturbed Ag_{Li}^{2+} defect remains [13]. Hole release from the lithium vacancy in the $[V_{Li}^{+} - Ag_{Li}^{2+}]^{2+}$ defect charge state occurs near 200 K. If the crystal is illuminated by 442 nm laser light at low temperature, electrons released by the 442 nm light from interstitial Ag^{0} sites recombine with a holes trapped on the $[V_{Li}^{+} - Ag_{Li}^{2+}]^{+}$ defect pair. The result is a $[V_{Li}^{+} - Ag_{Li}^{+}]^{0}$ pair in a net neutral charge state. At low temperature, the trapped hole prefers the oxygen site in coordination with the lithium vacancy. When a crystal with defect pairs in the $[V_{Li}^{+} - Ag_{Li}^{+}]^{0}$ charge state is left at room temperature for 10 hours some, but not all, of the holes trapped at the lithium vacancy are lost. This indicates that the $[V_{Li}^{+} - Ag_{Li}^{+}]^{0}$ trapped hole is stable to temperatures near 100 ℃. Whereas, the $[V_{Li}^{-} - Ag_{Li}^{2+}]^{0}$ trapped hole is stable to temperatures greater than 200 ℃. In Cu-doped $Li_2B_4O_7$, the $[V_{Li}^{-} - Cu_{Li}^{2+}]^{0}$ trapped hole does not anneal [11]. When the lithium vacancy in the $[V_{Li}^{+} - Ag_{Li}^{+}]^{0}$ releases a hole, it may simply move across the lithium vacancy from the coordinating oxygen ion and re-trap at the perturbed-Ag_{Li} site. Or, it may move about the crystal until it traps at an isolated-Ag_{Li} site or recombines at a trapped electron site (either V_{O}^{-} or Ag^{0}).

In a $Li_2B_4O_7$ crystal Ag-doped via diffusion, the number of $[V_{Li}^{-} - Ag_{Li}^{2+}]^{0}$ trapped holes exceeds the number of Ag_{Li}^{2+} trapped holes by 20 times after irradiation with x rays at room temperature. This is opposite of the same relationship in as grown Ag-doped $Li_2B_4O_7$ where Ag_{Li}^{2+} trapped holes exceed the number of $[V_{Li}^{-} - Ag_{Li}^{2+}]^{0}$ trapped holes by 13 times. Furthermore, after the diffusion doped crystal has set at room temperature for two months, the number of $[V_{Li}^{-} - Ag_{Li}^{2+}]^{0}$ trapped holes is nearly equal to the number of Ag_{Li}^{2+} trapped holes after irradiation with x rays at room temperature. The V_{Li} likely diffuses away from the substitutional Ag^{+} over time at room temperature toward more positively charged defects such as oxygen vacancies converting the $[V_{Li}^{-} - Ag_{Li}^{+}]^{-}$ defect into a Ag_{Li}^{+} defect.

3.2 Isolated Oxygen Vacancies

Figure 11 shows the room temperature EPR spectrum of x ray irradiated copper doped lithium tetraborate ($Li_2B_4O_7$:Cu). Note that neither of the two 16 line EPR spectra for electrons trapped at the interstitial copper atoms (Cu_A^0 or Cu_B^0 [11]) are visible in the spectra. Individual lines in both 16 line spectra have broadened due to elevated temperature and, therefore, are not visible. The only visible spectrum in this region of the magnetic field is due to an electron trapped at an oxygen vacancy (V_O^-). The EPR spectra for both species of Cu_{Li}^{2+} are also broadened and not visible at room temperature. The four lines in the V_O^- EPR spectrum are due to ^{11}B hyperfine, and the smaller lines inside the four line spectrum are due to the lesser abundant ^{10}B isotope [31]. In fact, in LiB_3O_7 crystals, the V_O^- EPR spectrum clearly shows resolved hyperfine for two unequal boron nuclei [41].

With the magnetic field aligned parallel to the [001] direction of the crystal, the average separation between adjacent lines in Figure 11 (a) is 9.85 mT, with a line width of 2.83 mT. The average separation between adjacent lines while the magnetic field is aligned parallel to the [100] direction of the crystal is 11.38 mT with a line width of 2.49 mT in Figure 11 (b). The ratio of average separation [100] to [001] is 1.16. At low temperature, Swinney found that the same ratio was 0.837 [31]. The g value for the V_O spectrum in Figure 11 (a) is 2.0049 (± 0.001) with very little variation in the g value when the magnetic field is rotated to align with the [100] crystal direction [31].

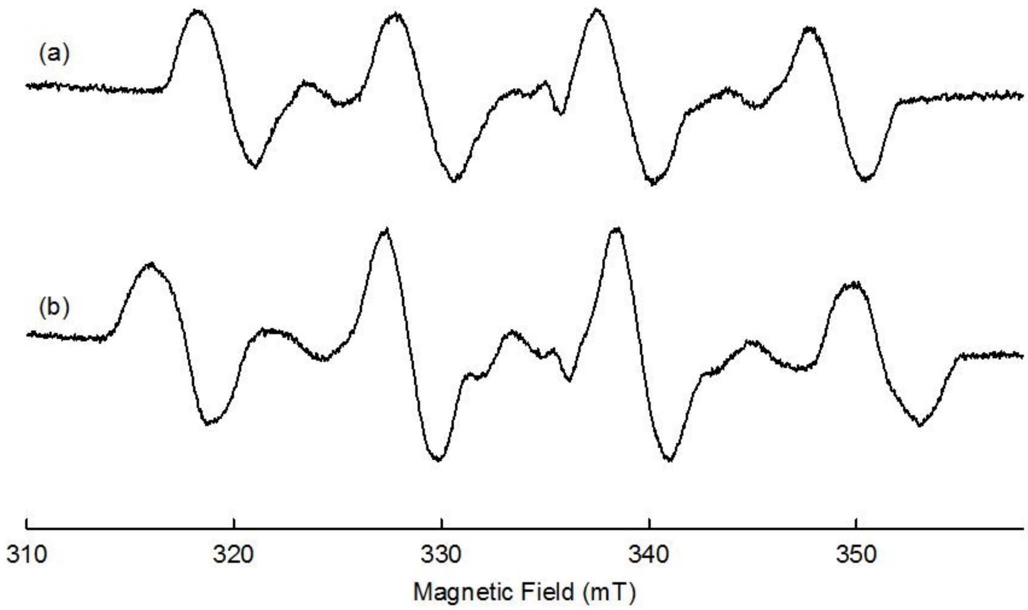

Figure 11. Oxygen vacancy EPR spectrum in x ray irradiated $Li_2B_4O_7$:Cu. EPR spectrum taken at room temperature with the (a) magnetic field aligned with the [001] direction of the crystal and (b) magnetic field aligned with the [100] direction of the crystal.

Thermoluminescence glow curves for $Li_2B_4O_7$:Cu are known and have been presented in many publications [4-5, 10, 42-49]. The main glow peak is at 200 °C, with a lesser intense peak near 100 °C [11]. The 100 °C glow peak is due to electrons released from V_O^- recombining with holes trapped at Cu_{Li}^{2+} sites. The EPR spectrum for an x ray irradiated $Li_2B_4O_7$:Cu crystal left at room temperature for greater than 10 hours does not have any spectrum for oxygen vacancy trapped electrons, and there is no 100 °C peak in the TL glow curve. Furthermore, the wavelength spectrum of the TL emission at 100 °C peaks near 370 nm indicate a Cu^{1+} related emission [11]. Brant's third unobserved and unidentified defect releasing electrons near 100 °C is an oxygen vacancy. In fact, the defect is not simply an oxygen vacancy, it is an oxygen vacancy that is perturbed by a dopant Cu ion. As presented by Hunda, increasing the concentration of copper dopant decreased the temperature of the lesser intense TL peak from near 160 °C, 0.0009 wt. %, to only 100 °C, 0.381 wt. % [49]. As the concentration of copper dopant increases the average distance between copper ions and intrinsic oxygen vacancies decrease. At low dopant concentrations, 0.0009 wt. %, the 160 °C TL peak most likely represents the intrinsic oxygen vacancy which may be perturbed by a nearby lithium vacancy. At high dopant concentrations, 0.381 wt. %, the 100 °C, TL peak most likely represents an oxygen vacancy perturbed by a nearby copper ion. In fact, in silver doped $Li_2B_4O_7$ the first less intense TL peak caused by release of electrons from oxygen vacancy traps is at even lower temperature 75 °C [29], and the oxygen vacancy EPR spectrum disappears within minutes at room temperature [30]. This dopant (type and concentration) dependence of the lowest temperature and less intense TL peak strongly suggests the oxygen vacancy is perturbed by a nearby dopant ion. Furthermore, the relatively broad EPR line shape of 20 mT [31] and the larger width at half maximum and asymmetry of the 100 °C TL [49] peak suggest more than one species of similar copper-perturbed oxygen vacancy. It seems likely that the oxygen vacancies observed by Swinney had a nearby perturbing defect. The perturbing defect is most likely a lithium vacancy. In the as grown, undoped crystal the opposite charge of the lithium and oxygen vacancies would encourage the two defects to diffuse together and form defect pairs.

Figure 12 (a) shows the EPR spectrum of a new oxygen vacancy species in Ag diffusion doped $Li_2B_4O_7$. The EPR spectrum consists of a telltale four line ^{11}B hyperfine spectrum centered at 334 mT with a g value of 2.0076 (±0.0001). The expected ^{10}B

hyperfine is not visible between the four ^{11}B lines due to lines from other defects. Some interstitial Ag^0 trapped electrons are also still visible in the spectrum. The spectrum line width was 0.74 mT with an average interline spacing of 8.86 mT when the magnetic field is aligned with the [001] direction of the crystal. With the magnetic field aligned parallel to the crystal [100] direction, Figure 12 (b), the line width was 1.27 mT with and average interline spacing of 7.71 mT. The ratio of average separation [100] to [001] is 0.888 which is in good agreement with the value reported by Swinney for what are likely oxygen vacancies perturbed by a nearby lithium vacancy. Figure 12 (a) and (b) were taken after room temperature irradiation with x ray radiation, and warming the crystal to 170 °C for two minutes. The new oxygen vacancy spectrum was visible before the anneal, and the $V_{Li} - Ag_{Li}^{2+}$ spectrum was also visible before and after the anneal. Of note, this new oxygen vacancy spectrum is not visible in the same EPR spectrum when the EPR spectrum is taken at 30 K. It is likely that the spectrum is saturated due to the low temperature. Furthermore, the same new oxygen vacancy spectrum is also visible in $Li_2B_4O_7$ crystals doped with copper via diffusion. Burak noted the same spectrum in isotopically enriched $^6Li_2{}^{11}B_4O_7$ and $^7Li_2{}^{11}B_4O_7$ crystals after irradiation with thermal neutrons [50].

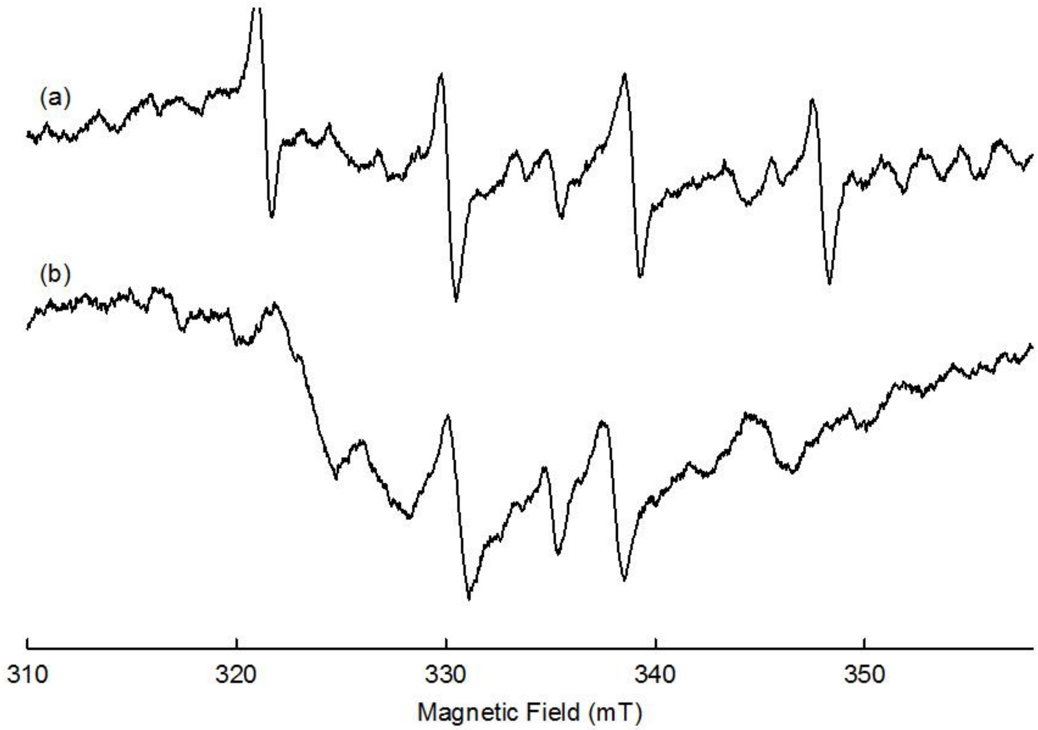

Figure 12. EPR spectrum of isolated oxygen vacancies in $Li_2B_4O_7$:Ag. Spectrum taken at room temperature after warming to 170 °C with the (a) magnetic field aligned with the [001] direction of the crystal and (b) magnetic field aligned with the [100] direction of the crystal.

Having very similar hyperfine and angular dependence as the intrinsic oxygen vacancy identified by Swinney, and also oxygen vacancies perturbed by copper or silver dopants, this new spectrum is most likely due to a new species of oxygen vacancy. The narrower line width, 0.71 mT versus 2.0 mT, suggests that the new oxygen vacancy has only one species, and no nearby additional defect. Taken along with the high thermal stability compared to the other know oxygen vacancies, the new oxygen vacancy is likely in an otherwise defect free lattice. When the crystal is rapidly cooled after diffusion doping, the isolated oxygen vacancy is likely "frozen" in the crystal lattice. When the crystal is grown and cooled slowly from melt temperatures, oxygen vacancies and other oppositely charged defects likely move within the lattice and form complexes. This movement time is not available in the diffusion doped crystal because the crystal is cooled rapidly.

The presence of isolated oxygen vacancies and the relatively high thermal stability of the $[V_{Li}^{-} - Ag_{Li}^{2+}]^{0}$ trapped hole may give rise to the TL glow peaks at temperatures above the main TL peak near 150 °C with a 1°C per second heating rate for Ag-doped $Li_2B_4O_7$ crystals [15, 29, 51-53]. Both charge traps demonstrate thermal stability greater than that of the main TL peak, and recombination of electrons and holes at the $[V_{Li}^{-} - Ag_{Li}^{2+}]^{+}$ trapped hole could produce luminescence near 270 nm.

4. Summary

Silver doping of $Li_2B_4O_7$ single crystals produces electron and hole traps with subtle yet significant variation for understanding $Li_2B_4O_7$:Ag based thermoluminescence dosimetry. The present paper clarifies the assignment of defect models for previously known electron and hole traps in $Li_2B_4O_7$:Ag, and identifies a new highly stable oxygen vacancy electron trap by using the EPR technique. In unirradiated as-grown crystals of $Li_2B_4O_7$, silver is all in the Ag^{+} charge state. The silver ions occupy both lithium sites as well as interstitial sites. Irradiation with x rays converts the substitutional silver ions to the Ag^{2+} charge state (trapped hole) and the interstitial silver ions to Ag^{0} atoms (trapped electron). Of the substitutional silver ions, some are in an otherwise defect free lattice, Ag_{Li}. While others form defect pairs with an adjacent lithium vacancy, $[V_{Li}^{-} - Ag_{Li}^{+}]^{0}$. The relative concentration of the two defects can be controlled via the doping process. Diffusion doping produces more $V_{Li} - Ag_{Li}$ defect pairs than doping during growth.

These hole traps serve as the recombination site for all TL peaks above room temperature in Ag-doped $Li_2B_4O_7$.

Two species of oxygen vacancies trap electrons during x ray irradiation of diffusion doped $Li_2B_4O_7$;Ag. Oxygen vacancies perturbed by a silver ion is unstable near 75 °C and is responsible for the lesser TL peak at the same temperature. These silver perturbed oxygen vacancies are responsible for the rapid fading of TL signals in the first few minutes after irradiation. Elimination of these oxygen vacancies would improve material performance in TL dosimetry. Other oxygen vacancies are in an otherwise defect free lattice, but are only formed by rapid cooling of the crystal after diffusion doping. The isolated oxygen vacancy is stable to 275 °C. Such a high temperature electron trap creates a high temperature TL peak in Ag-doped $Li_2B_4O_7$, which reduces fading in TL dosimetry, and enables dosimetry comparison to the main thermoluminescence peak near 150 °C.

IV. Optically stimulated luminescence (OSL) from Ag-doped $Li_2B_4O_7$ crystals

Abstract

Optically stimulated luminescence (CW-OSL) is observed from Ag-doped lithium tetraborate ($Li_2B_4O_7$) crystals. Photoluminescence, optical absorption, and electron paramagnetic resonance (EPR) are used to identify the defects participating in the OSL process. As-grown crystals have Ag^+ ions substituting for Li^+ ions. They also have Ag^+ ions occupying interstitial sites. During a room-temperature exposure to ionizing radiation, holes are trapped at the Ag^+ ions that replace Li^+ ions and electrons are trapped at the interstitial Ag^+ ions, i.e., the radiation forms Ag^{2+} ($4d^9$) ions and Ag^0 ($4d^{10}5s^1$) atoms. These Ag^{2+} and Ag^0 centers have characteristic EPR spectra. The Ag^0 centers also have a broad optical absorption band peaking near 370 nm. An OSL response is observed when the stimulation wavelength overlaps this absorption band. Specifically, stimulation with 400 nm light produces an intense OSL response when emission is monitored near 270 nm. Electrons optically released from the Ag^0 centers recombine with holes trapped at Ag^{2+} ions to produce the ultraviolet emission. The OSL response is progressively smaller as the stimulation light is moved to longer wavelengths (i.e., away from the 370 nm peak of the absorption band of the Ag^0 electron traps). Oxygen vacancies are also present in the Ag-doped $Li_2B_4O_7$ crystals, and their role in the OSL process as a secondary relatively short-lived electron trap is described.

1. Introduction

Lithium tetraborate ($Li_2B_4O_7$), known simply as LTB, has emerged in recent years as an important and versatile radiation-detector material. The primary focus thus far has been on the thermoluminescence (TL) properties of $Li_2B_4O_7$ [1-7, 9-15, 54]. Only recently has optically stimulated luminescence (OSL) been reported from this material [16-18, 55]. These TL and OSL investigations have shown that light emission is greatly enhanced when $Li_2B_4O_7$ is doped with either Cu^+ or Ag^+ ions. These monovalent dopants are unique in $Li_2B_4O_7$, as they serve as both a hole trap and an electron trap during exposures to ionizing radiation [6, 11]. When substituting for Li^+ ions, the Cu^+ and Ag^+ ions trap holes and become Cu^{2+} and Ag^{2+} ions. The Cu^+ and Ag^+ ions also occupy interstitial sites in this material where they trap electrons and become Cu^0 and Ag^0 atoms. After being thermally or optically released, these electrons recombine with holes at Cu^{2+} and Ag^{2+} ions and produce large TL and OSL signals. There is also interest in $Li_2B_4O_7$ because the ^6Li and ^{10}B nuclei have large cross-sections for thermal neutron absorption. Enrichment with either or both of these isotopes may allow $Li_2B_4O_7$ to be used as a neutron detector.

In the present paper, we investigate the fundamental mechanisms responsible for OSL in Ag-doped $Li_2B_4O_7$ crystals. One of the primary goals of our study is to establish the properties of the optical absorption band that allows OSL stimulation light to release electrons at room temperature. Photoluminescence (PL), photoluminescence excitation (PLE), electron paramagnetic resonance (EPR), and optical absorption are used to identify the electron and hole traps that are participating in the OSL process. The dependence of the OSL intensity on the wavelength of the stimulation light is determined and the specific recombination site for the OSL is identified. In addition to the primary interstitial Ag0 electron trap, unintentionally present oxygen vacancies are identified as a second active electron trap in the Ag-doped $Li_2B_4O_7$ crystals. These oxygen vacancies decrease the rate at which OSL light is emitted during stimulation, and thus reduce the OSL sensitivity of the material. Taken together, our results suggest that Ag-doped $Li_2B_4O_7$ will be a highly sensitive OSL-based radiation detector with commercial promise.

2. Experimental

A single crystal of $Li_2B_4O_7$ doped with Ag was grown by the Czochralski method at the Institute of Physical Optics (L'viv, Ukraine). A congruent melt, exposed to air, was contained in a Pt crucible. The growth axis was [001] and the pulling and rotation velocities did not exceed 0.3 mm/h and 10 revolutions/min, respectively. This method produces $Li_2B_4O_7$ crystals of high optical quality with sizes up to 25 mm in diameter and 40 mm in length. All of the OSL, PL, optical absorption, and EPR data reported in this paper were taken from one sample cut from the larger as-grown boule. The concentration of Ag in this sample is estimated, from the starting materials, to be 0.02 at.%. Its dimensions are approximately 0.83 × 3 × 6.5 mm3, with the [001] direction normal to the broad faces.

The symmetry of $Li_2B_4O_7$ crystals is tetragonal (space group I41cd and point group 4mm) with lattice constants a = 9.475 Å and c = 10.283 Å at room temperature [34-35, 56-57]. There are 104 atoms (eight formula units) in a unit cell. A $(B_4O_9)^{6-}$

anionic group, consisting of two BO_3 and two BO_4 units, serves as the repeating structural building block. In general, $Li_2B_4O_7$ crystals have two inequivalent boron sites and four inequivalent oxygen sites. All the lithium sites are crystallographically equivalent. Each oxygen ion has two boron neighbors, whereas each lithium ion has four close oxygen neighbors (arranged asymmetrically around it) and two additional slightly more distant oxygen neighbors. Figure 13 shows a $(B_4O_9)^{6-}$ group along with one nearby Li^+ ion and its additional neighboring oxygen ions.

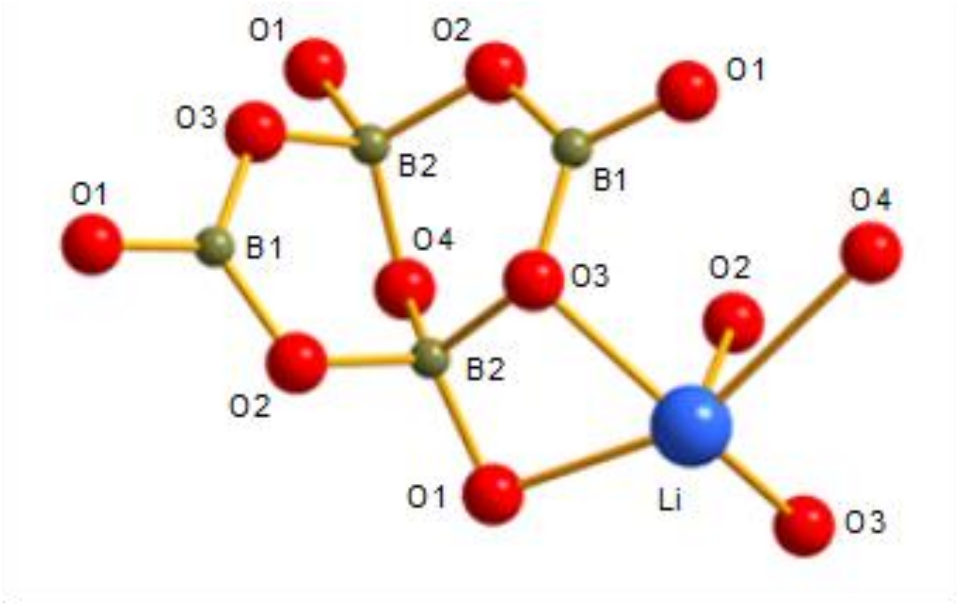

Figure 13. Schematic representation of the $(B_4O_9)^{6-}$ basic anionic group used to construct the tetragonal $Li_2B_4O_7$ crystal. Also shown are a lithium ion and its additional surrounding oxygen ions. Lithium ions are blue, boron ions are green, and oxygen ions are red. The ions are labeled according to the scheme used in Refs. [31, 34, 35].

An Horiba Fluorolog-3 spectrometer was used to obtain the PL, PLE, and OSL data. This spectrometer has a xenon lamp as the excitation source, a Hamamatsu R928 photomultiplier as a detector, and two double-grating monochromators to measure emission and excitation spectra. The spectrometer was operated in a kinetics mode when acquiring OSL data (i.e., emission data were collected as a function of time while using fixed excitation and monitoring wavelengths). In all experiments, the slit widths were set at 10 nm resolution for the excitation monochromator and 5 nm resolution for the emission monochromator.

Optical absorption data were obtained with a Cary 5000 dual-beam spectrophotometer from Varian. The absorption spectra were taken at room temperature with corrections made for surface reflective losses. A Bruker EMX spectrometer operating near 9.38 GHz was used to take the EPR data. The crystal was irradiated at room temperature using an x-ray tube (Varian OEG-76H) operating at 60 kV and 30 mA. Irradiation times were 2 min. Before each exposure to the x rays, the crystal was held at 400 ºC for 3 min to remove any effects of previous irradiations.

3. Results

A comprehensive set of experiments was performed on a Ag-doped $Li_2B_4O_7$ crystal. The goals were to identify the defects participating in the OSL response, determine the site where the OSL radiative recombination occurs, and find the optimum stimulation wavelengths that produce OSL. The following subsections describe the results obtained from these PL, PLE, OSL, optical absorption, and EPR experiments.

3.1. Photoluminescence (PL and PLE)

Figure 14 shows the PL and PLE spectra obtained at room temperature from our Ag-doped $Li_2B_4O_7$ crystal. Prior to taking these data, the sample was reset to its as-grown state by heating to 400 ºC. The PL band has a peak at 270 nm and a full width at half maximum (FWHM) of 0.54 eV, whereas the corresponding PLE band has a peak near 210 nm and a FWHM of 0.41 eV. Earlier studies [7, 10, 16] have assigned these PL and PLE bands to Ag^+ ions occupying Li^+ sites in the $Li_2B_4O_7$ crystals. The excitation band corresponds to a $4d^{10}$ to $4d^95s^1$ intracenter transition of the Ag^+ ion while the emission band is a Stokes-shifted $4d^95s^1$ to $4d^{10}$ transition back to the ground state (excitations and emissions of this type are usually described by a two-level configurational coordinate diagram). The observation of this 270 nm emission peak and 210 nm excitation peak in our crystal before an x-ray irradiation verifies that Ag^+ ions are present.

The PL spectrum in Figure 14 was acquired by operating the emission monochromator of the Fluorolog-3 spectrometer in second order (i.e., this monochromator was scanned from 470 to 630 nm while detecting the actual emission in the 235 to 315 nm region). Also, the PLE spectrum in Figure 14 has not been corrected either for the rapidly decreasing intensity of the xenon lamp in the 220 to 200 nm region or for the wavelength dependence of the excitation monochromator. These corrections (that account for changes in incident photon flux) will shift the PLE peak closer to the 205 nm value that has been reported by earlier investigators [7, 10, 16]. We do not attempt to make these corrections in our PLE data because a calibrated power meter was not available for use in determining the wavelength dependence of the combined output of our xenon lamp and excitation monochromator in this short-wavelength region. The lack of a correction is not a significant deficiency since the optical absorption data presented in Section 3.3.2 verifies that the excitation band producing the PL has a peak at 205 nm.

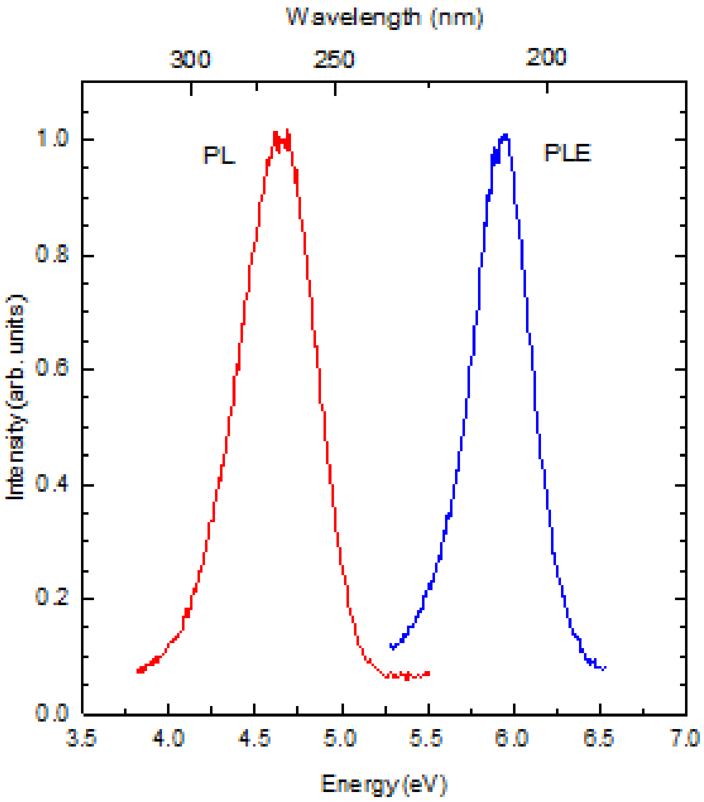

Figure 14. PL and PLE spectra obtained at room temperature from Ag^+ ions in a $Li_2B_4O_7$ crystal. The PL spectrum (red curve) was taken with 210 nm excitation light and the PLE spectrum (blue curve) was obtained by monitoring (in second order) the emission at 270 nm.

3.2. Optically stimulated luminescence (OSL)

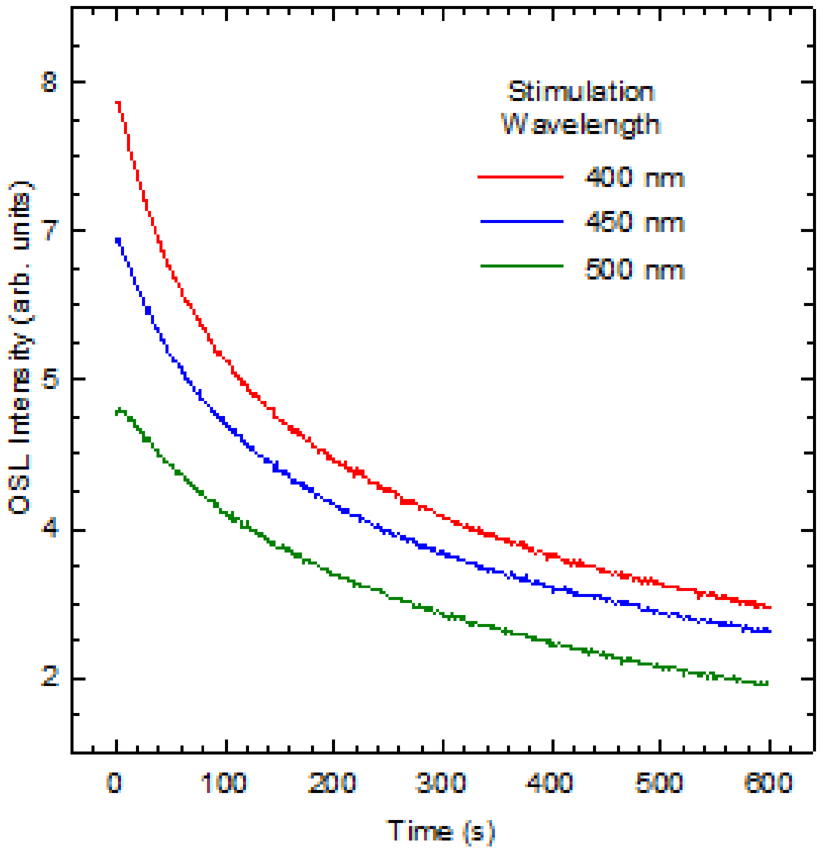

Figure 15. OSL response curves taken at room temperature from an x-ray-irradiated Ag-doped $Li_2B_4O_7$ crystal, while using 400, 450, and 500 nm stimulation light and monitoring (in second order) the emission at 270 nm. The initial OSL intensity decreases as the stimulation light moves to longer wavelengths.

A large OSL response was observed from our Ag-doped $Li_2B_4O_7$ crystal after exposing it to ionizing radiation (i.e., x-rays) at room temperature. Three OSL decay curves are shown in Figure 15. These OSL data were taken with our Fluorolog-3 spectrometer operating in the kinetics mode. The excitation monochromator was set for 10 nm resolution and centered at either 400, 450, or 500 nm, while the emission monochromator was set at 5 nm resolution and used to monitor (in second order) the emission at 270 nm. As seen in Figure 15, the 400 nm stimulation light is more efficient than the 450 or 500 nm light at generating an OSL signal. Although not shown, the OSL response is even larger when 350 nm stimulation light is used. Our optical absorption curves in Section 3.3.2 provide an explanation for this dependence on stimulation wavelength. The OSL decay curves in Figure 15 are nonexponential and a cursory examination suggests that fast and slow components may be present. As described in Section 3.4, oxygen vacancies serving as electron traps may be partly responsible for the slow component.

The series of spectra in Figure 16 illustrate the wavelength dependence of the OSL emission. As the OSL signal was decaying as a function of time during stimulation with 400 nm light, the emission monochromator in the Fluorolog-3 spectrometer was set to scan repeatedly from 470 to 630 nm, thus allowing detection of the 270 nm emission band in second order. Each scan took 12 s with 4 s required to reset the monochromator. The five spectra shown in Figure 16 were taken 6, 38, 86, 278, and 630 s after turning on the 400 nm stimulation light. These scans show no significant change in the wavelength dependence of the emission during the OSL decay which, in turn, suggests that the recombination site remains the same during the decay. The most intense (i.e., the first) emission curve in Figure 16 has a peak near 270 nm and a FWHM of 0.53 eV. This and the other OSL emission curves in Figure 16 strongly resemble the PL emission curve in Figure 14. The same peak position and shape suggests that these two emissions have a common origin (i.e., the recombination that gives rise to the PL and OSL emissions in our $Li_2B_4O_7$ crystal occurs at a Ag ion that occupies a Li^+ site).

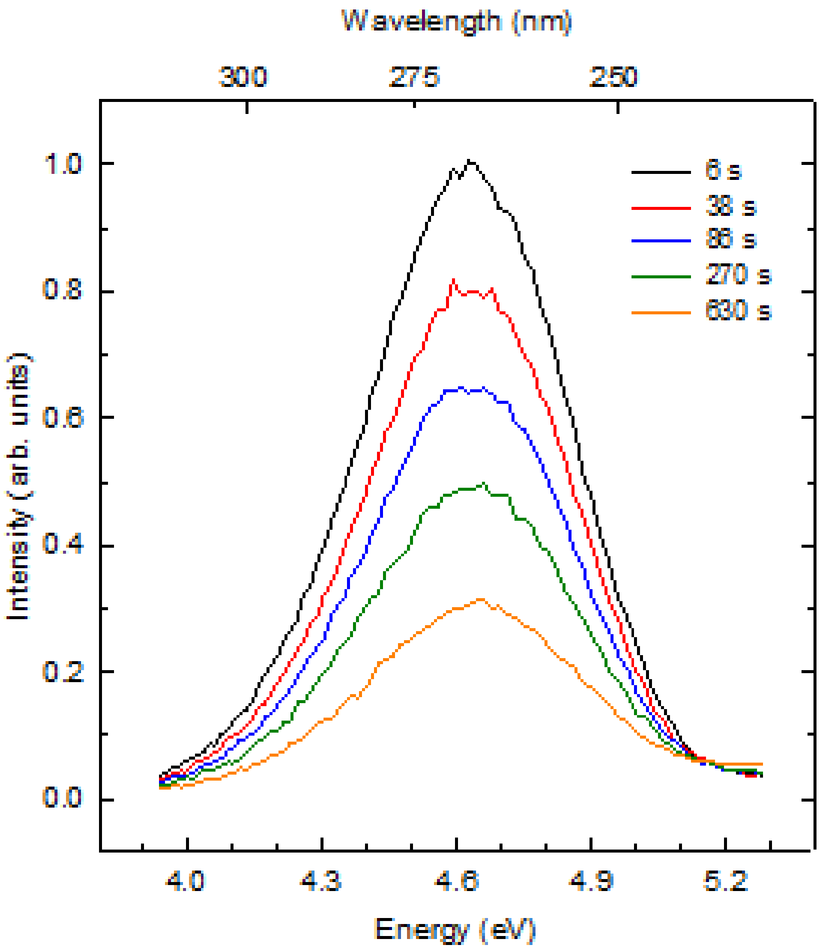

Figure 16. Spectral dependence of the emitted OSL light from the Ag-doped $Li_2B_4O_7$ crystal. The peaks in these emission scans were reached 6, 38, 86, 278, and 630 s after starting the OSL decay. All of the OSL emission curves have a maximum near 270 nm, thus demonstrating that the OSL emission has the same spectral dependence as the PL spectrum in Figure 14.

As expected, the OSL signal from our Ag-doped $Li_2B_4O_7$ crystal was much larger when a 65 mW diode laser emitting 405 nm light was used as a stimulation source. The intensity of this laser light was significantly greater than the intensity of the 400 nm light from the coupled xenon lamp and excitation monochromator in the Fluorolog-3 spectrometer. With the stronger stimulation light from the laser, the OSL decay occurred in a shorter time and the signal-to-noise ratio of the OSL signal was much greater than in

Figure 15. A second factor affecting the OSL signal is our use of a monochromator on the detection side of the Fluorolog-3 spectrometer (when recording the OSL response in second order, the resolution of this emission monochromator was set at 5 nm). The signal-to-noise ratio of the OSL light will be larger if this monochromator is removed and all the emitted light is incident on the photomultiplier tube (with perhaps one or more filters to eliminate unwanted light).

3.3. Primary defects involved in OSL

3.3.1. Electron paramagnetic resonance (EPR)

Two trapped-hole centers and one trapped-electron center, each with an unpaired spin, are formed when our Ag-doped $Li_2B_4O_7$ crystal is irradiated at room temperature with x rays [6, 13]. Figure 17(a) shows the EPR signals from each of these S = 1/2 centers. This spectrum was taken at 32 K with the magnetic field along the [001] direction. The two distinct hole centers (which we have labeled isolated Ag^{2+} and perturbed Ag^{2+}) are observed in the low-field region of Figure 17(a). These labels, respectively, refer to a Ag^{2+} ion with no other defect nearby and a Ag^{2+} ion with an adjacent defect. These trapped hole centers are formed when Ag^+ ($4d^{10}$) ions at Li^+ sites trap the radiation-induced holes and become Ag^{2+} ($4d^9$) ions. Direct evidence that the two EPR spectra represent Ag^{2+} ions comes from their large positive *g* shifts, their small hyperfine splittings, and the unambiguous electron-nuclear double resonance (ENDOR) identification of ^{107}Ag and ^{109}Ag as the nuclei responsible for the hyperfine splittings [6]. In previous papers [6, 13], these trapped-hole centers were simply labeled Center A and Center B, respectively. Our new labels are more informative. The perturbing entity associated with Center B was suggested, in the past, to be a Na^+ or Ag^+ ion at an adjacent regular lithium site [13]. Our observations of how OSL stimulation light affects the two EPR signals (these results are described in Section 3.3.3) now suggest that an adjacent lithium vacancy is a third, and very likely, possibility for the perturbation. Analogous defects, i.e., isolated Cu^{2+} ions and Cu^{2+}-V_{Li} centers, have been previously observed in $Li_2B_4O_7$ and $LiAlO_2$ crystals [11, 58].

The electron center in Figure 17(a) has a 16-line EPR spectrum centered at 335.4 mT. This defect is formed during the x-ray irradiation when an interstitial Ag^+ ($4d^{10}$) ion traps an electron and becomes a Ag^0 ($4d^{10}5s^1$) center. As described previously [6], the trapped-electron spectrum in Figure 17(a) has 16 lines because of resolved hyperfine interactions with ^{107}Ag and ^{109}Ag nuclei and one additional $I = 3/2$ nucleus. A comparison of our spectrum with the analogous spectrum from radiation-induced Cu^0 centers in Cu-doped $Li_2B_4O_7$ crystals [11] strongly suggests that the $I = 3/2$ nucleus in our Ag^0 spectrum is a ^{11}B neighbor. In the Cu^0 centers, the participating $I = 3/2$ nucleus must be ^{11}B because resolved less intense hyperfine lines from ^{10}B nuclei are also seen (^{11}B nuclei are 80.1% abundant with $I = 3/2$ while the ^{10}B nuclei are 19.9% abundant with $I = 3$).

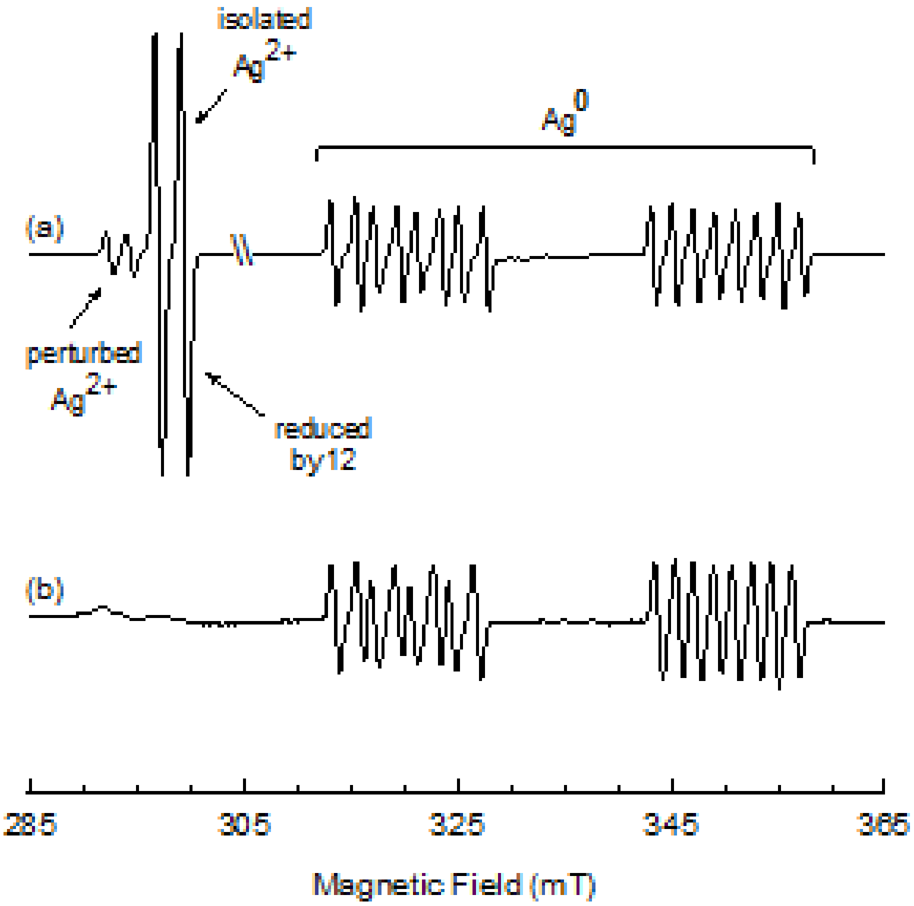

Figure 17. EPR spectra of isolated Ag^{2+} ions, perturbed Ag^{2+} ions, and Ag^0 centers. These data were taken after the Ag-doped $Li_2B_4O_7$ crystal was irradiated at room temperature with x rays. The magnetic field was along the [001] direction and the microwave frequency was 9.38 GHz. (a) Spectrum taken at 32 K (the intensities of the Ag^{2+} ions at low field have been reduced by a factor of 12). (b) Spectrum taken at room temperature.

The large hyperfine interaction of approximately 3.9 mT with the neighboring ^{11}B nucleus in the Ag^0 trapped-electron center provides supporting evidence that this Ag^0 center is located at an interstitial position in the Ag-doped $Li_2B_4O_7$ crystals. Such a large hyperfine interaction is not expected if the Ag^0 atom occupies a regular Li^+ site in the crystal (this is because of the relatively large separation distance of 2.7 Å between a Li^+ site and the nearest B^{3+} site). Having the Ag^0 center at an interstitial position is, however, consistent with one large ^{11}B hyperfine interaction. In as-grown or reset crystals (i.e., before an x-ray irradiation), Ag^+ ions will occupy interstitial positions that are preferentially located near a $(BO_3)^{3-}$ or $(BO_4)^{5-}$ unit, since the positive charge of the Ag^+ ion is attracted to the negative charge of the borate unit. After an irradiation, the 5*s* electron in the interstitial Ag^0 atom will have significant overlap with this one nearest-neighbor boron (a result in agreement with the EPR hyperfine data). In addition to this boron hyperfine result, the relative sizes of the Li^+ and Ag^+ ions also support having Ag^+ ions occupy interstitial positions during growth. The ionic radius of Ag^+ (1.15 Å) is greater than the ionic radius of Li^+ (0.76 Å) in six fold coordination, and thus replacement of regular Li^+ ions with Ag^+ ions requires significant distortion in the surrounding lattice.

Interestingly, the EPR spectra from the trapped-hole and trapped-electron centers can be observed at room temperature after an x-ray irradiation (see Figure 17(b)). Comparing the spectra in Figure 17(a) and Figure 17(b) shows that the EPR signals from the two trapped-hole centers broaden significantly, but are still easily recognizable, at the higher temperature. As the temperature increases, lines from the isolated Ag^{2+} centers broaden at a slightly greater rate than lines from the perturbed Ag^{2+} centers. In contrast, the signals from the trapped-electron centers broaden only slightly as the temperature increases. The option of observing these EPR spectra at room temperature allows easier monitoring of the trapped holes and trapped electrons when searching for correlations with OSL and TL emissions (i.e., there is no need to have access to low-temperature EPR capabilities).

3.3.2. Optical absorption

Figure 18 shows the optical absorption spectrum of the Ag-doped $Li_2B_4O_7$ crystal before and after an irradiation at room temperature with x rays, and also after exposures to OSL stimulation light. These data were taken at room temperature using unpolarized light propagating along the [001] direction in the crystal. The sample thickness was 0.83 mm and the two broad faces of the crystal were polished. Known values of the refractive indices of crystalline $Li_2B_4O_7$ in the 800 to 195 nm region [59] were used to correct the spectra for surface reflective losses. Before the irradiation with x rays (trace a), the only absorption feature present is a band peaking near 205 nm (6.05 eV). This band has been widely reported and is assigned to Ag^+ ions at Li^+ sites [7, 10, 16].

After the x-ray irradiation, the optical absorption spectrum is very different (see trace b in Figure 18). The x-rays have introduced four addition absorption bands that extend across the visible and well into the ultraviolet region [39, 60-61]. The primary radiation-induced band peaks near 370 nm (3.35 eV), while the others peak near 250 nm (4.95 eV), 296 nm (4.19 eV), and 650 nm (1.91 eV). Attempts to deconvolute the after-irradiation spectrum (trace b) in Figure 18 into a set of Gaussian bands suggest that two overlapping bands with peaks in the 340-400 nm region are needed to replicate the large 370 nm absorption feature. The band in the longer wavelength portion of this 370 nm feature is assigned to the electric-dipole-allowed $4d^{10}5s^1$ to $4d^{10}5p^1$ transition of the Ag^0 center [26]. This $4d^{10}5p^1$ excited state has a delocalized character and is near, or possibly in, the conduction band [62-63]. Thus, stimulation wavelengths within this band easily release trapped electrons from the Ag^0 centers. These released electrons then recombine with trapped holes at Ag^{2+} ions and produce OSL emission. The second band, on the short wavelength side of the 370 nm feature, is possibly due to a charge-transfer process associated with the isolated Ag^{2+} center (i.e., an electron is transferred from a neighboring oxygen ion to the Ag^{2+} ion) [64]. Stimulation light in this second band will create an excited state that can decay in either of two ways. The excited-state complex (consisting of a Ag^{+} ion with an adjacent O^{-} ion) may decay radiatively to restore the initial Ag^{2+} and O^{2-} ions or the hole on the oxygen ion may migrate away from the Ag^{+} ion (i.e., by hoping from oxygen to oxygen). This latter decay mechanism provides an alternative path to generate an OSL signal wherein the holes optically released from the Ag^{2+} ions move to Ag^{0} centers and recombine with the trapped electrons to produce the characteristic 270 nm emission light.

As illustrated in Figure 18, the radiation-induced optical absorption decreases when 400 nm OSL stimulation light (from the Fluorolog-3 spectrometer) is incident at room temperature on the Ag-doped $Li_2B_4O_7$ crystal. Spectra taken after 100 s (trace c), 300 s (trace d), and 700 s (trace e) of 400 nm exposure are shown in Figure 18. All of the absorption features decrease except for the band peaking near 296 nm (4.19 eV). The EPR results described in Section 3.3.3 show that the perturbed Ag^{2+} centers are the only defects not affected by the OSL excitation light. This, in turn, suggests that the perturbed Ag^{2+} centers (via a charge-transfer transition) are responsible for the 296 nm optical absorption band. At the present time, the absorption band peaking near 250 nm (4.95 eV) in Figure 18 is not assigned to a specific defect. The band peaking near 650 nm (1.91

eV) is most likely due to a crystal-field (i.e., *d*-to-*d*) transition of the isolated Ag^{2+} ions [64].

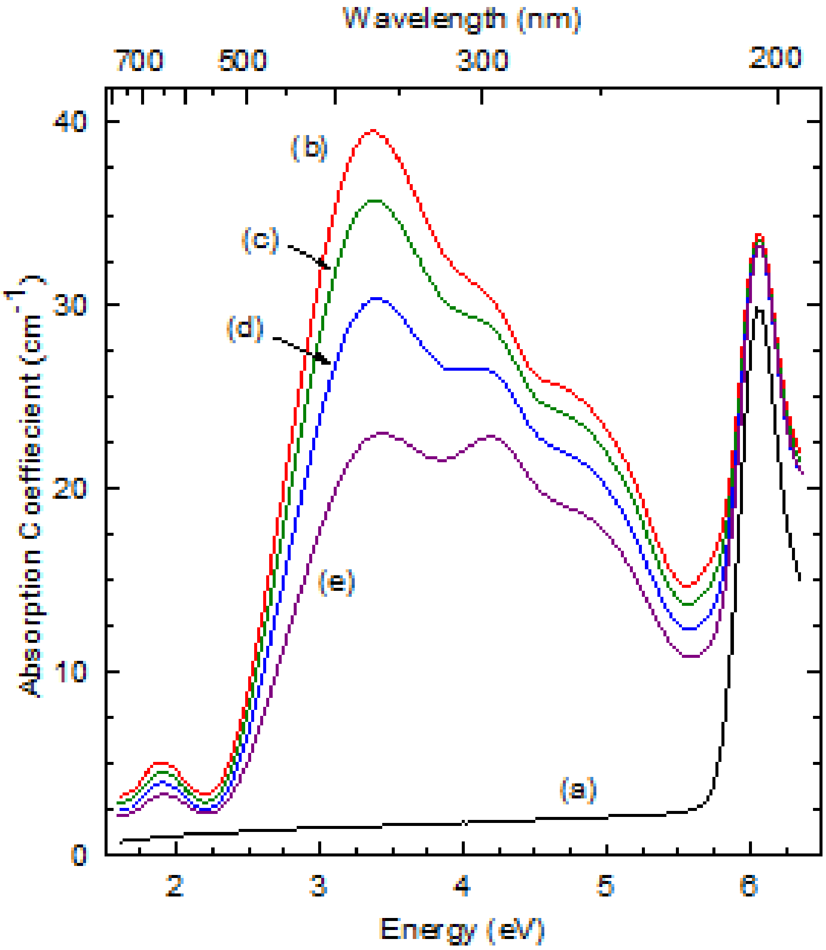

Figure 18. Optical absorption from the Ag-doped $Li_2B_4O_7$ crystal. These spectra were taken at room temperature with unpolarized light propagating along the [001] direction. (a) Before an x-ray irradiation (black curve). (b) After a room-temperature x-ray irradiation (red curve). (c) After exposure to 400 nm light for 100 s (green curve). (d) After exposure to 400 nm light for 300 s (blue curve). (e) After exposure to 400 nm light for 700 s (purple curve).

3.3.3. Correlation of EPR and optical absorption with OSL

The trapped electron and trapped hole centers that participate in the OSL response of the Ag-doped $Li_2B_4O_7$ crystal are determined by monitoring their EPR spectra during an exposure to 400 nm stimulation light. The spectrum in Figure 19(a) was obtained immediately after an irradiation with x rays, while the spectrum in Figure 19(b) was taken after exposing the crystal for 700 s to 400 nm stimulation light from the Fluorolog-3 spectrometer (this is the same stimulation source used to obtain the OSL data in Figs. 3 and 4). Vertical scales are kept the same for Figure 19(a) and Figure 19(b) to allow easy comparison of signal intensities. These two EPR spectra show that the OSL stimulation light does not affect the number of perturbed Ag^{2+} centers, but significantly decreases the concentrations of isolated Ag^{2+} centers and Ag^0 centers. The results in Figure 19 provide evidence that the recombination of electrons and holes occurring during OSL takes place only at isolated Ag^{2+} centers, and not at perturbed Ag^{2+} centers. This difference in behavior for the two trapped-hole centers is expected if the perturbed Ag^{2+} centers are electrically neutral and thus do not attract the optically released electrons at the same rate as the isolated Ag^{2+} centers with their effective positive charge. The perturbed Ag^{2+} center will be electrically neutral if a Li^+ vacancy is adjacent to the Ag^{2+} ion.

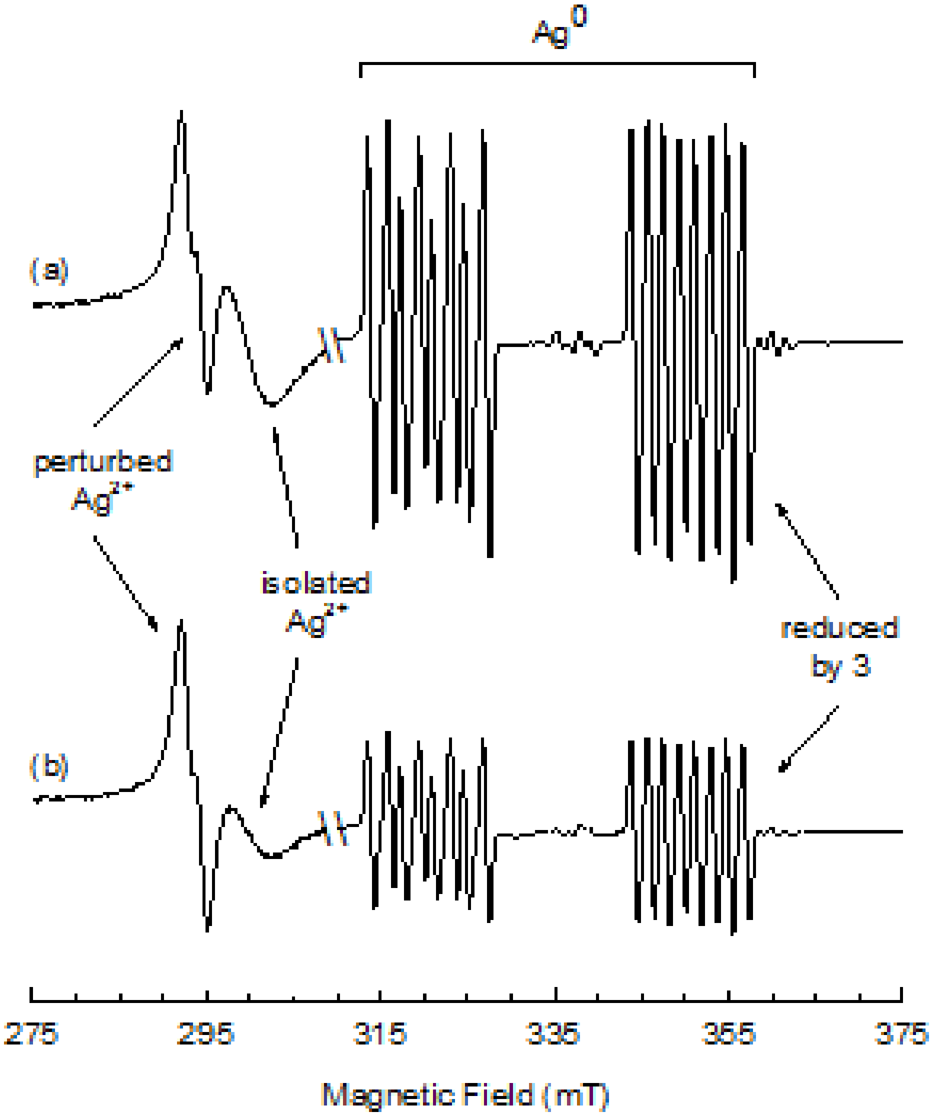

Figure 19. Effect of 400 nm stimulation light on the EPR signals from the isolated Ag^{2+} ions, the perturbed Ag^{2+} centers, and the Ag^0 centers. These spectra were taken at room temperature with the magnetic field along the [001] direction. (a) Spectrum taken after an x-ray irradiation, but before exposure to OSL stimulation light. (b) Spectrum taken after exposure to 400 nm light for 700 s. In both spectra, the intensity of the 16-line Ag^0 center has been reduced by a factor of 3.

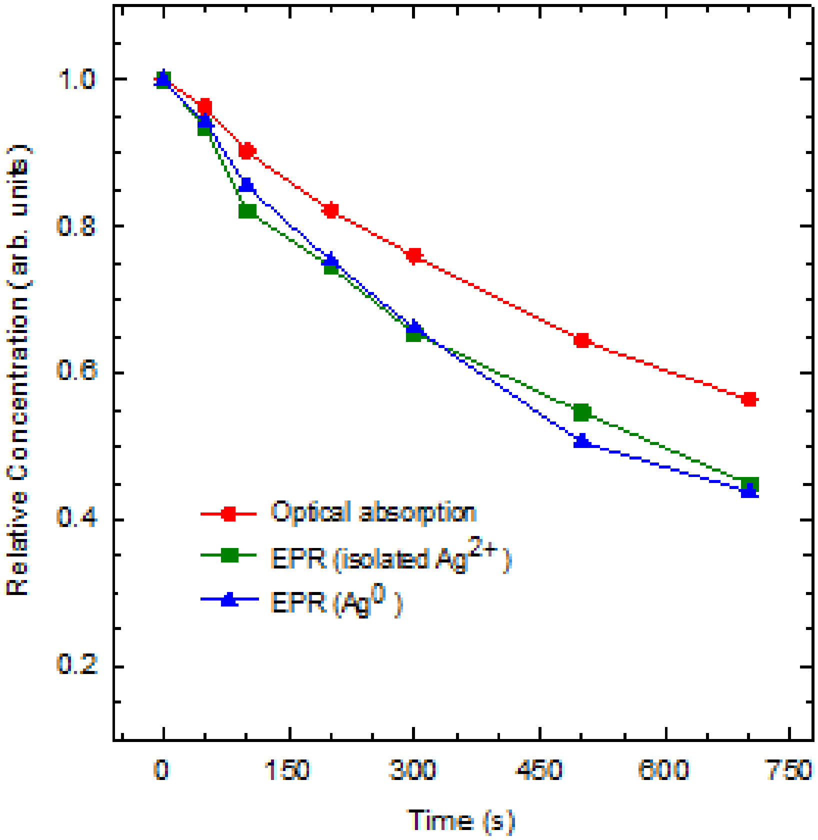

Figure 20. Decrease in the intensities of the 370 nm optical absorption band, the isolated Ag^{2+} center, and the Ag^0 EPR spectrum during exposure at room temperature to 400 nm OSL stimulation light. The crystal was initially irradiated with x rays. The red curve (circles) represents the 370 nm absorption band, the blue curve (triangles) represents the isolated Ag^{2+} EPR signal, and the green curve (squares) represents the Ag^0 EPR signal.

Figure 20 shows in more detail the effects of the OSL stimulation light on the EPR and optical absorption spectra from the participating trapped electron and trapped hole center. Intensities of the Ag^0 EPR spectrum, the isolated Ag^{2+} EPR spectrum, and the 370 nm optical absorption band are plotted as a function of the time the crystal was exposed to 400 nm stimulation light from the Fluorlog-3 spectrometer. The observed reductions in the intensities of the three spectra in Figure 20 (representing the concentrations of active trapped electrons and trapped holes) correlate with the emission of OSL light described in Figure 15. In Figure 20, the curve representing the decay of the 370 nm optical absorption band is slightly above the curves representing the two EPR centers. This suggests that there is an underlying less-intense band contributing to the optical absorption at 370 nm in Fig. 6 that is not affected by the 400 nm stimulation light. The presence of an underlying absorption band is also suggested by the small shift to shorter wavelength of the peak of the 370 nm feature during the decay sequence shown in Figure 18.

3.4. Role of oxygen vacancies in OSL

Oxygen vacancies are present in our Ag-doped $Li_2B_4O_7$ crystal [31]. These vacancies are in the doubly ionized charge state in the as-grown crystal, with no trapped electrons and thus no EPR signal. During an x-ray irradiation at room temperature, a portion of the oxygen vacancies trap an electron and form the EPR-active singly ionized charge state. These paramagnetic oxygen vacancies have a characteristic 4-line EPR spectrum due to the hyperfine interaction with one ^{11}B neighbor, thus making them easy to monitor [31]. After they are formed by the x rays, the singly ionized oxygen-vacancies slowly decay at room temperature over times on the order of 5-10 min, as the trapped electrons are thermally released from the vacancies. This means that the electrons trapped at oxygen vacancies are thermally much less stable than electrons trapped at Ag^0 centers.

The EPR results in Figure 21 verify that oxygen vacancies are present and active in our Ag-doped $Li_2B_4O_7$ crystal. The spectrum in Figure 21(a) was taken several hours after an irradiation with x rays, and is similar to the spectrum in Figure 19(a). Then the crystal was exposed to 405 nm stimulation light from the 65 mW diode laser. After an exposure for 120 s to this laser light, the EPR spectrum in Figure 21(b) was immediately taken. The 405 nm light releases electrons from the Ag^0 centers, thus making the intensity of the Ag^0 EPR spectrum in Figure 21(b) less than its intensity in Figure 21(a). Many of the released electrons recombine with holes at the isolated Ag^{2+} ions and produce an OSL emission. Some of these optically released electrons, however, become trapped temporarily at oxygen vacancies. By acquiring the spectrum in Figure 21(b) within 20 s of turning off the 405 nm stimulation light, the electrons trapped at oxygen vacancies did not have time to thermally decay. In Figure 21(b), the 4-line EPR spectrum from the electrons trapped at the oxygen vacancies overlaps the 16-line spectrum from the Ag^0 centers. A difference spectrum obtained by subtracting the spectrum in Figure 21(a) from the spectrum in Figure 21(b) reveals the underlying EPR spectrum from the oxygen vacancies. Before the subtraction, the intensity of the 16-line Ag^0 spectrum in Figure 21(a) was reduced to be the same as the 16-line spectrum in Figure 21(b). The difference spectrum, shown in Fig. 9(c), represents the singly ionized oxygen vacancies. It is identical to the oxygen-vacancy EPR spectrum previously seen in undoped $Li_2B_4O_7$ crystals that had been x-ray irradiated at 77 K [31].

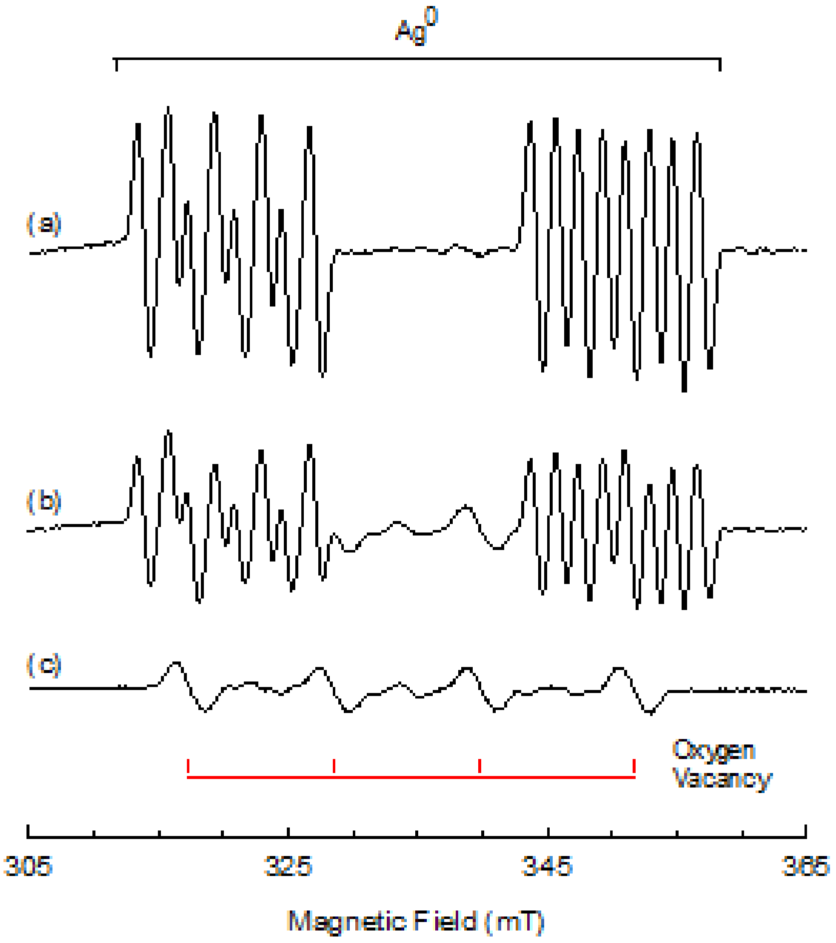

Figure 21. EPR spectra from Ag^0 centers and singly ionized oxygen vacancies in the Ag-doped $Li_2B_4O_7$ crystal. (a) Spectrum taken after an x-ray irradiation at room temperature. (b) The same spectrum taken immediately after exposing the crystal to 405 nm laser light for 120 s. (c) The difference spectrum showing the underlying four-line oxygen vacancy EPR signal. These four lines are due to the hyperfine interaction with one ^{11}B nucleus (see Ref. [31]).

Our results indicate that oxygen vacancies in $Li_2B_4O_7$ serve as a short-lived electron traps at room temperature and reduce the rate at which the optically released electrons recombine with holes at isolated Ag^{2+} ions. Fewer oxygen vacancies will mean larger OSL signals in Ag-doped $Li_2B_4O_7$. Also, by showing that OSL stimulation light forms singly ionized oxygen vacancies, we verify that the optical release of electrons from Ag^0 electron traps is the primary OSL mechanism in Ag-doped $Li_2B_4O_7$.

4. Summary

A large OSL response has been observed from a Ag-doped $Li_2B_4O_7$ crystal. The Ag^+ ions enter the lattice and occupy two distinctly different sites (i.e., they replace Li^+ ions and they also become interstitials). During an irradiation, Ag^+ ions at Li^+ sites trap holes and become isolated Ag^{2+} ions while Ag^+ ions at interstitial sites trap electrons and become Ag^0 atoms. The Ag^0 centers have a broad optical absorption band peaking near 370 nm with a tail extending beyond 500 nm. Stimulation light with wavelengths in this Ag^0 band releases electrons, that then recombine with holes at the isolated Ag^{2+} ions and form Ag^+ ions in a short-lived excited state, i.e., $(Ag^+)^*$ ions. The OSL emitted light with a peak near 270 nm is characteristic of the radiative decay of these $(Ag^+)^*$ ions and is the same as the photoluminescence band observed from an intracenter excitation of Ag^+ ions in $Li_2B_4O_7$. The following summarizes the primary OSL process in Ag-doped $Li_2B_4O_7$ (Ag_i represents Ag at an interstitial position and Ag_{Li} represents Ag at a Li^+ site).

(1) Irradiation step:

$$e^- + Ag_i^+ \longrightarrow Ag_i^0 \qquad \text{(trapped electron)}$$

$$h^+ + Ag_{Li}^+ \longrightarrow Ag_{Li}^{2+} \qquad \text{(trapped hole)}$$

(2) Stimulation step:

$$Ag_i^0 + h\nu \text{ (400 nm photon)} \longrightarrow Ag_i^+ + \text{released } e^-$$

(3) Emission step:

$$\text{released } e^- + Ag_{Li}^{2+} \longrightarrow (Ag_{Li}^{+})^* \longrightarrow Ag_{Li}^{+} + h\nu \text{ (270 nm photon)}$$

In conclusion, our results suggest that Ag-doped $Li_2B_4O_7$ will be a useful OSL material because of a unique combination of defect properties. (1) Doping with Ag produces both electron and hole traps since the Ag^+ ions occupy two distinctly different sites in as-grown material. (2) Electrons trapped as interstitial Ag^0 centers have an intense optical absorption band that allows the OSL stimulation light to easily release electrons. (3) Highly efficient electron-hole recombination occurs at isolated Ag^{2+} trapped-hole centers located at regular Li^+ sites. Future studies are needed to identify the optimum concentrations of interstitial Ag^+ ions (electron traps) and Ag^+ ions at lithium sites (hole traps) that must be present in the pre-irradiated $Li_2B_4O_7$ to make the most sensitive OSL dosimeters. Also, methods must be found to minimize the concentration of oxygen vacancies.

V. Two new silver related electron traps in Ag-doped $Li_2B_4O_7$ crystals

Abstract

Electron paramagnetic resonance (EPR) and thermoluminescence (TL) are used to identify and characterize two new silver related electron traps, $[Ag_i^+ - Ag_{Li}^+]^+$ and $[Ag_i^+ - Li^+]^+$, in Ag-doped lithium tetraborate ($Li_2B_4O_7$) crystals. Additionally, the one known, interstitial silver atom (Ag^0) electron trap is further characterized. In as grown Ag-doped $Li_2B_4O_7$, Ag^+ ions substitute for Li^+ ions, and Ag^+ ions also occupy interstitial sites. Ag^+ ions substituting for Li^+ ions act as hole traps and interstitial Ag^+ ions act as electron traps when the crystal is exposed to ionizing radiation. Interstitial silver ions occur in three distinct environments in the Ag-doped $Li_2B_4O_7$ crystal. Interstitial ions may be in an otherwise unperturbed lattice ($[Ag_i^+ - Li^+]^+$), adjacent to a substitutional silver ion ($[Ag_i^+ - Ag_{Li}^+]^+$), or near a lithium vacancy ($[Ag_i^+ - V_{Li}^-]^0$). When exposed to ionizing x ray radiation at room temperature, the $[Ag_i^+ - Ag_{Li}^+]^+$ and $[Ag_i^+ - V_{Li}^-]^0$ defects trap an electron becoming $[Ag_i^0 - Ag_{Li}^+]^0$ and $[Ag_i^0 - V_{Li}^-]^-$ while the $[Ag_i^+ - Li^+]^+$ traps two electrons becoming $[Ag_i^- - Li^+]^-$. When exposed to ionizing radiation at 77 K, the $[Ag_i^+ - Ag_{Li}^+]^+$ defect traps two electrons becoming $[Ag_i^0 - Ag_{Li}^0]^-$. One electron is released from the $[Ag_i^0 - Ag_{Li}^0]^-$ defect near room temperature, and one electron is released from the $[Ag_i^- - Li^+]^-$ defect near 120 °C. Electrons trapped at the $[Ag_i^0 - Ag_{Li}^+]^0$ and $[Ag_i^0 - Li^+]^0$ defects both have greater thermal stability than an electron trapped at the $[Ag_i^0 - V_{Li}^-]^-$ defect. Both $[Ag_i^+ - Ag_{Li}^+]^+$ and $[Ag_i^+ - Li^+]^+$ defects lead to TL peaks at temperatures greater than 150 °C.

1. Introduction

Single crystal, silver doped lithium tetraborate ($Li_2B_4O_7$:Ag) is a potentially important radiation dosimetry material. The crystal makes a functional dosimeter in both the thermally stimulated luminescence (TL) and the optically stimulated luminescence (OSL) modes [9, 13, 15-16, 18, 29-30]. Furthermore neutron dosimetry may be achieved by enriching the crystal in either ^{6}Li or ^{10}B. In Ag doped $Li_2B_4O_7$, Ag^+ ($4d^{10}$) occupies lithium sites and interstitial sites. Room temperature exposure to ionizing radiation produces electron hole pairs in the crystal lattice. These charge pairs may quickly recombine, or become trapped at defect sites in the crystal. Interstitial silver ions trap an electron becoming Ag^0 silver atoms. These silver trapped electrons are stable up to approximately 150 °C [6, 30]. When thermally released, recombination with holes yields TL light emission. Substitutional silver ions trap a hole becoming Ag^{2+} ($4d^9$). Two different substitutional sites exist. One substitutional silver ion is in an otherwise defect free lattice (Ag_{Li}^{2+}) and the other has a nearby lithium vacancy ($[V_{Li} - Ag_{Li}]$). The role of both species of substitutional silver trapped holes in thermoluminescence has been established [13, 30]. It has also been shown that intrinsic oxygen vacancies and oxygen vacancies perturbed by silver ions serve as a short lived electron trap in Ag doped $Li_2B_4O_7$ [30].

In the present paper, we use electron paramagnetic resonance and thermoluminescence to identify three different interstitial silver electron traps that exist in Ag-doped $Li_2B_4O_7$. Interstitial silver ions may be in an otherwise unperturbed lattice ($[Ag_i^+ - Li^+]^+$), adjacent to a substitutional silver ion ($[Ag_i^+ - Ag_{Li}^+]^+$), or near a lithium vacancy ($[\mathrm{Ag_i}^{+} - \mathrm{V_{Li}}^{-}]^{0}$). Under x-ray irradiation the interstitial Ag^{+} ($4d^{10}$) ion traps an electron and becomes an Ag^{0} ($4d^{10}5s^{1}$) center. In the cases where no lithium vacancy is present, a second electron may be trapped. The maximum reduction in each case is to the 1− charge state, relative to a defect free lattice. In previous work, the $[\mathrm{Ag_i}^{0} - \mathrm{V_{Li}}^{-}]^{-}$ trapped electron has been referenced as the silver atom, Ag^{0}. Lastly, $[\mathrm{Ag_i}^{0} - \mathrm{Li}^{+}]^{0}$ and $[\mathrm{Ag_i}^{0} - \mathrm{Ag_{Li}}^{+}]^{0}$ are shown to have greater thermal stability than electrons trapped at $[\mathrm{Ag_i}^{0} - \mathrm{V_{Li}}^{-}]^{-}$.

Interstitial defects are denoted with a subscript i and substitutional defects are denoted with a subscript Li or subscript O for defects at lithium or oxygen sites, respectively Superscripts are used to denote the charge state of individual ions or defects when the superscript is adjacent to the ion or defect symbol. As an example, $\mathrm{Ag_{Li}}^{+}$, is a 1+ silver ion on a lithium site. If the superscript is adjacent to a pair of defects inside square braces, then the superscript denotes the charge state of the defect pair relative to a defect free lattice. As an example, $[\mathrm{V_{Li}}^{-} - \mathrm{Ag_{Li}}^{+}]^{-}$ is a lithium vacancy 1− adjacent to a substitutional 1+ silver. The defect pair has a 1− charge state relative to a defect free lattice.

2. Experimental

Lithium tetraborate crystals have a tetragonal structure (space group I41cd) with a point group of 4mm. The lattice constants for the crystal, at room temperature, are a=9.475 Å and c=10.283 Å. There are two inequivalent boron sites and four inequivalent oxygen sites. All of the lithium sites are equivalent. There are 104 atoms in the unit cell organized in eight formula units. The formula units transform one to another according to the symmetry of the crystal [32-35]. The basic repeating group, $(B_4O_9)^{6-}$, consists of two boron ions, B2, tetrahedrally coordinated by four oxygens and two boron ions, B1, triangularly coordinated by three oxygens [32]. Each of the oxygen ions is coordinated to two boron ions. Further, the boron-oxygen framework creates channels along the c-axis which are filled by LiO_5 polyhedra, in which, the O3 and O4 oxygen ions are coordinated by two lithium ions, and the O1 and O2 oxygen ions are coordinated by one lithium ion [34]. Figure 22 shows a sparse crystal model of $Li_2B_4O_7$ consisting of two LO_5 polyhedra from two adjacent polyhedra chains, and the common O4 ion linking them. Also shown is the next O4 ion in the minus c direction.

Silver doped crystals were cut from a larger boules. The as grown silver doped crystal had nominal dimensions of $0.83 \times 3 \times 6.5$ mm^3. The [001] direction was normal to the broad faces. The Ag-doped sample was grown by the Czochralski method at the Institute of Physical Optics (L'viv, Ukraine). A congruent melt, exposed to air, was contained in a Pt crucible. The growth axis was [001] and the pulling and rotation velocities did not exceed 0.3 mm/h and 10 revolutions/min, respectively. The concentration of Ag in the Ag-doped sample is estimated, from the starting materials, to be 0.02 at. %.

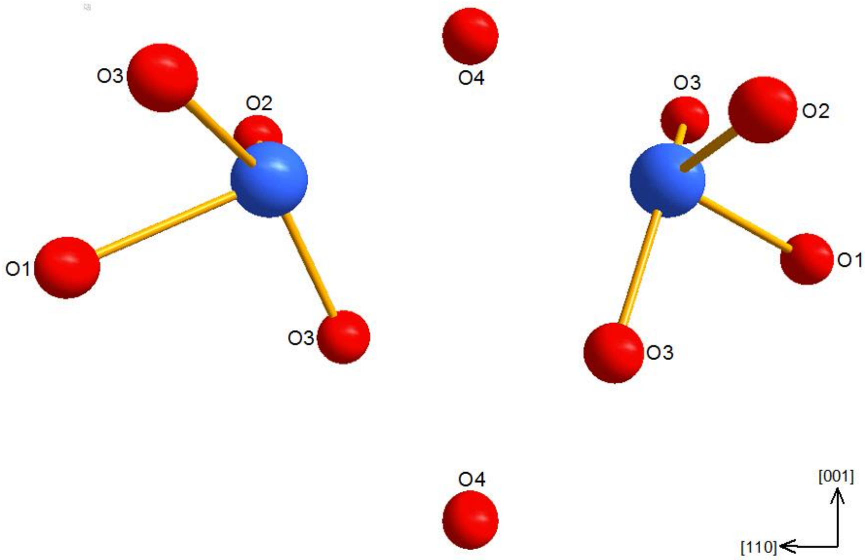

Figure 22. Sparse ball and stick model of $Li_2B_4O_7$. The model contains two LiO_4 polyhedra that share a single O4 ion. The O4 ion at the top of the figure is shared by the two LiO_5 polyhedra. The O4 at the bottom of the figure represents the next lower $(B_4O_9)^{6-}$ group in the crystal. Lithium ions are blue and oxygen ions are red.

EPR data were taken using a Bruker EMX spectrometer operating near 9.4 GHz. An Oxford helium-gas flow system controlled the temperature of the sample and magnetic fields were measured using a Bruker teslameter. A proton NMR gaussmeter was used to obtain static magnetic field values, and a small Cr-doped MgO crystal was used to correct the magnetic field for the difference between the sample position and the position of the gaussmeter. Crystals were irradiated using a Varian OEG-67H x ray tube operating at 60 kV and 30 mA. The duration of each irradiation was three minutes. TL “glow curves” were obtained using an ANDOR Shamrock 193i spectrograph coupled to an iDus 420 CCD camera (the sample was heated at a constant rate with an Instec HCS621G stage).

3. Results

Figure 23 shows a typical room temperature EPR spectrum for Ag-doped $Li_2B_4O_7$ after irradiation with x rays at room temperature. The spectrum was taken with the magnetic field aligned along the [001] direction of the crystal, and the microwave frequency was 9.38 MHz. The upper field portion of the EPR spectrum has been reduced by 3 times for ease of plotting. Clearly visible in Figure 23 are Ag_{Li}^{2+} and $[V_{Li} - Ag_{Li}]^{2+}$ trapped holes as well as $[Ag_i - V_{Li}]^0$ trapped electrons (Ag^0). The trapped-electron spectrum centered at 335.4 mT has 16 lines because of resolved hyperfine interactions with ^{107}Ag and ^{109}Ag nuclei and one additional I = 3/2 nucleus [6].

After irradiation with x rays, the crystal was held at room temperature for at least 10 minutes to allow fading of oxygen vacancy trapped electrons. Furthermore, electrons thermally released from oxygen vacancies may re-trap at other vacant electron traps or recombine with holes stabilized at hole traps thereby increasing the intensity of the corresponding electron and hole spectra. By allowing for complete fading of the oxygen vacancies, re-trapping and recombination events cease thereby allowing EPR spectra intensities to stabilize prior to measurement.

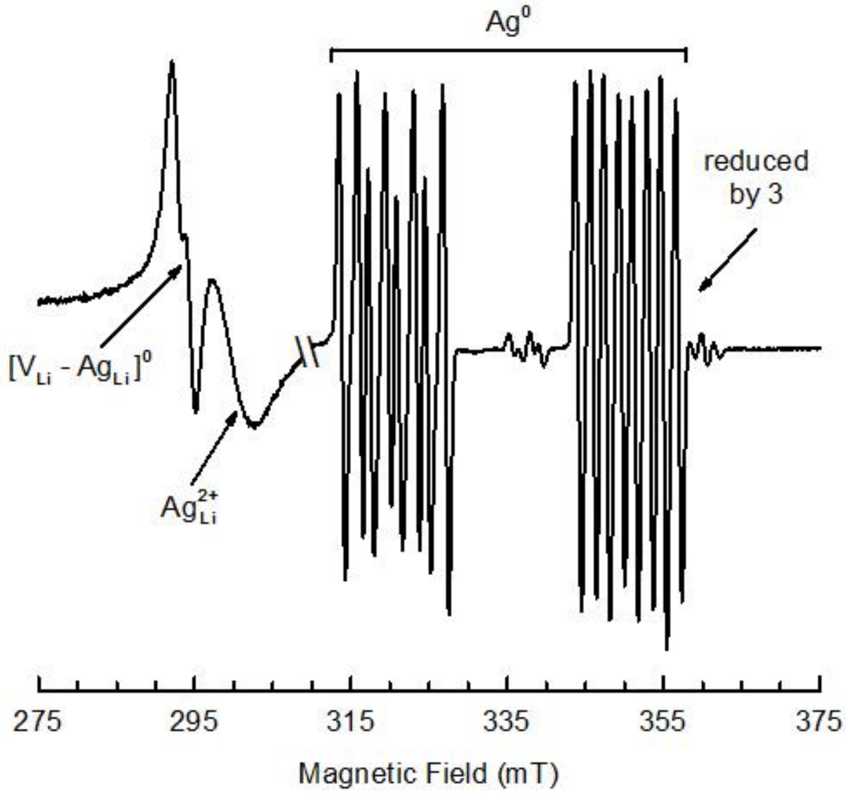

Figure 23. EPR spectra of isolated Ag_{Li}^{2+} ions, perturbed $[V_{Li}^{-} - Ag_{Li}^{2+}]^{2+}$ ions, and Ag^0 centers. These data were taken after the Ag-doped $Li_2B_4O_7$ crystal was irradiated at room temperature with x rays. The magnetic field was along the [001] direction and the microwave frequency was 9.38 GHz. Spectrum taken at room temperature (the intensity of the 16-line Ag^0 center has been reduced by a factor of 3).

3.1 Electron trap: interstitial silver ions adjacent to substitutional silver ions

When the doping level of silver into the $Li_2B_4O_7$ crystal is relatively high, interstitial silver ions may be adjacent to silver ions present on a lithium site. In this case the net effective charge state of the silver-silver defect is 1+ relative to a defect free lattice ($[Ag_i - Ag_{Li}]^+$). When exposed to room temperature ionizing radiation, this silver-silver defect traps an electron becoming $[Ag_i - Ag_{Li}]^0$. Figure 24 (c) shows the EPR spectrum for $[Ag_i - Ag_{Li}]^0$. This spectrum, Figure 24 (c), was obtained by subtracting

Figure 24 (a) from Figure 24 (b). Figure 24 (a) was taken at least 10 minutes after room temperature x ray irradiation of the Ag doped $Li_2B_4O_7$ crystal. The 16-line hyperfine spectrum is due to electrons trapped at interstitial silver atoms perturbed by lithium vacancies. Figure 24 (b) was collected after the crystal was warmed to 93 °C and exposed to room light for 20 hours. At 93 °C, the $[Ag_i - Ag_{Li}]^0$ trapped electron is slightly less likely to be released by room light than the $[Ag_i - V_{Li}]^-$ trapped electron. Therefore, the relative intensity of the $[Ag_i - Ag_{Li}]^0$ trapped electron spectrum increases relative the $[Ag_i - V_{Li}]^-$ trapped electron spectrum. The 16-line hyperfine spectrum in Figure 24 (a) is then reduced to match the intensity of the 16-line hyperfine spectrum in Figure 24 (b). Subtraction then cancels the 16-line $[Ag_i - V_{Li}]^-$ spectrum leaving only the $[Ag_i - Ag_{Li}]^0$ spectrum in Figure 24 (c).

The hyperfine spectrum for the $[Ag_i - Ag_{Li}]^0$ trapped electron is produced by interaction of the trapped electron with two nearly equal silver ions. The spectrum is composed of two triplets, one each at 315 mT and 360 mT, and a four line spectrum near 337 mT. The extreme outer two lines at high and low field are due to interaction with two ^{109}Ag nuclei (red stick diagram). While the next line in at either end (the middle double intensity line in the high and low field triplet) are due to interaction with one ^{107}Ag nucleus and one ^{109}Ag nucleus (black stick diagram). While the blue stick diagram represents the lines due to interaction with two ^{107}Ag nuclei. The inner four lines are due to superposition of two triplet spectra as found in the outer triplets. First order approximations would yield a triplet of twice the intensity of the outer triplets directly midpoint between the outer triplets. Second order effects cause the first order double intensity triplet to separate into four hyperfine lines near the midpoint of the outer two triplets.

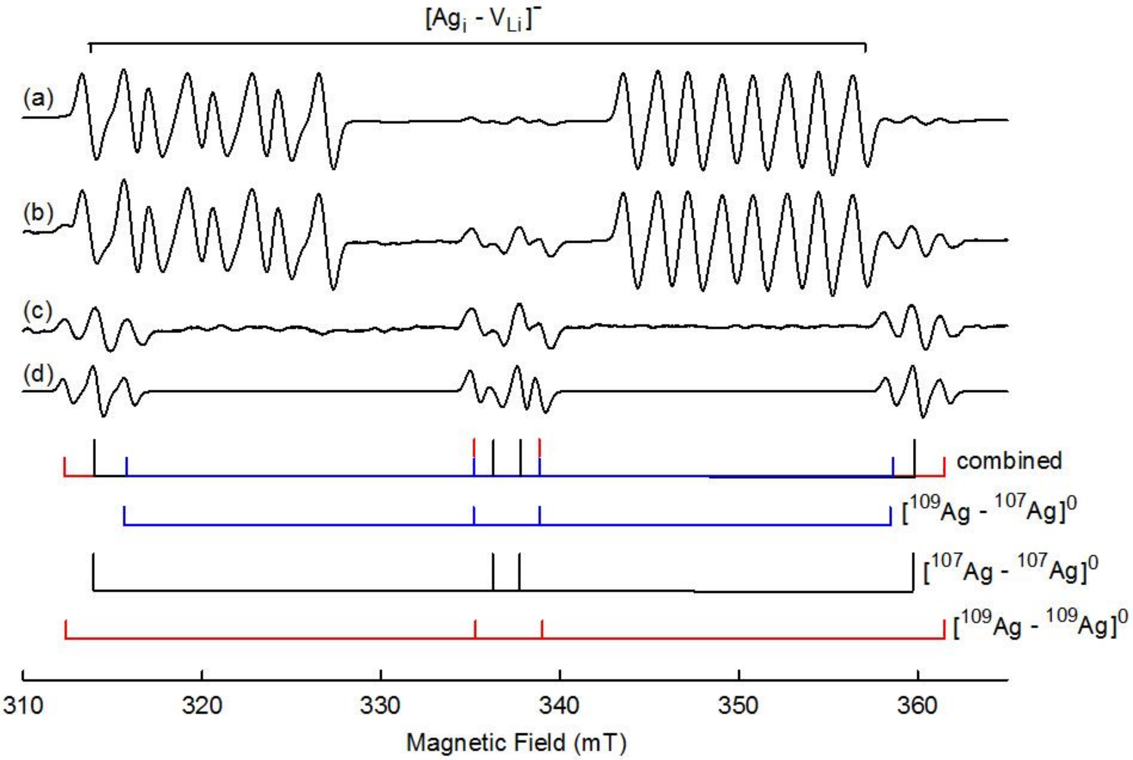

Figure 24. EPR spectrum of $[Ag_i - Ag_{Li}]^0$ in the $Li_2B_4O_7$ crystal. (a) Spectrum taken after an x-ray irradiation at room temperature. (b) The same spectrum taken after 20 hrs at 93 ℃ under room light. (c) The difference spectrum showing the underlying $[Ag_i - Ag_{Li}]^0$ EPR signal. (d) A simulation of the $[Ag_i - Ag_{Li}]^0$ EPR spectrum. The magnetic field was along the [001] direction and the microwave frequency was 9.40 GHz. Spectrum taken at room temperature.

The ratio of the splitting between the outer $[^{107}Ag_i - ^{107}Ag_{Li}]^0$ lines and the splitting between the outer $[^{109}Ag_i - ^{109}Ag_{Li}]^0$ lines is 0.8647, which agrees well with the ratio of the nuclear magnetic moments of ^{107}Ag to ^{109}Ag of 0.8682. This confirms that the hyperfine splitting is due to silver nuclei.

Figure 24 (d) is a simulated $[Ag_i - Ag_{Li}]^0$ produce using the EasySpin computer program. Isotropic hyperfine matrices were used, with values of 18.3 mT for ^{107}Ag

nuclei and 21.1 mT for ^{109}Ag nuclei at one Ag site, and hyperfine values if 18.6 mT for ^{107}Ag nuclei and 21.4 mT for ^{109}Ag nuclei at the other Ag site. The simulation linewidth was set to 0.7 mT. Agreement between the experimental spectrum Figure 24 (c) and the simulation Figure 24 (d) is good. The simulation shows that roughly 49.7 % of the electron spin density is on one Ag ion, while 50.3 % of the spin density is on the other Ag ion. In fact, the four-line hyperfine structure in the center of the $[Ag_i - Ag_{Li}]^0$ EPR spectrum is very sensitive to the amount of spin density on each Ag ion. As little as a half a percent change in spin density from one ion to the other causes poor agreement between the center of the experimental spectrum and the simulated spectrum.

Figure 25 displays a defect model for the $[Ag_i - Ag_{Li}]$ electron trap. The interstitial Ag ion is placed on the line connecting the two nearest O4 ions along the [001] direction in the crystal. The Ag ion is placed slightly closer to the upper O4 ion than the lower O4 ion. The four boron 3+ ions in the $(B_4O_9)^{6-}$ anionic block associated with the lower O4 ion would be between the O4 ion and the Ag ion along the c direction. Whereas the upper O4 would be between the Ag ion and the $(B_4O_9)^{6-}$ anionic group associated with the upper O4 ion. The Ag ion would feel a slightly greater negative charge from the upper O4 ion than the lower O4 ion and mover toward the upper O4 ion accordingly. Although the model shows the interstitial Ag ion along the c axis between the two O4 ions, it is likely that the interstitial Ag ion would be offset from the c axis position. The immediate symmetry of the crystal around the interstitial Ag ion site is not sufficient to suggest this unique position is favored. A slight offset toward the substitutional Ag ion, depicted, would yield the $[Ag_i - Ag_{Li}]$ defect.

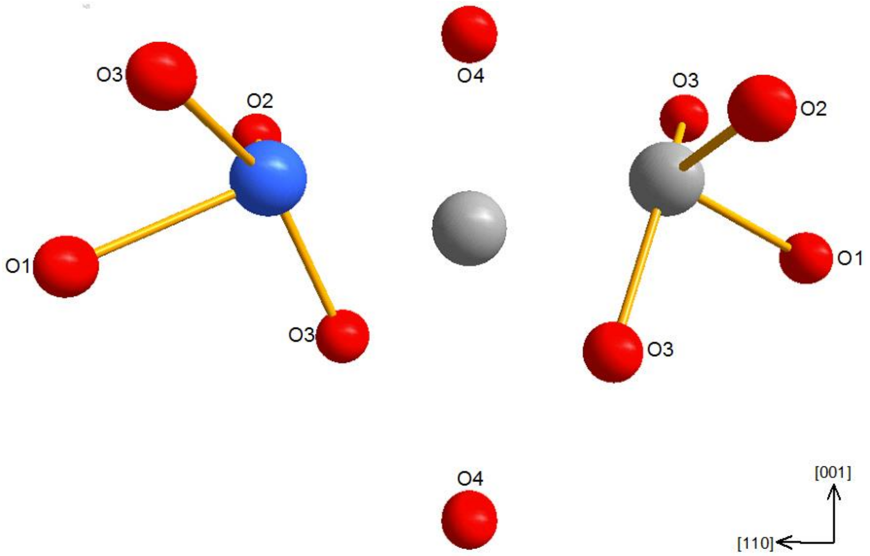

Figure 25. Model of $[Ag_i - Ag_{Li}]$ electron trap. The lithium ion is blue, oxygen ions are red, and the silver ions are gray.

An electron trapped on one of the Ag ions in the $[Ag_i - Ag_{Li}]^0$ defect ($4d^{10}5s^1$) would not display much angular dependence in the g or hyperfine matrices due to the largely s nature of the unpaired electron. Indeed, the g matrix is nearly isotropic for the $[Ag_i - Ag_{Li}]^0$ defect, and the hyperfine matrix shows less than 10 % variation in a [001] to [100] rotation of the applied magnetic field. Furthermore, the measured value of the hyperfine parameter for the ^{109}Ag is 1372 MHz from Figure 24 (c). This is in good agreement with the typical splittings reported for $^{109}Ag^0$ atoms (1300-2100 MHz) [65]. Nearly all the unpaired spin is present on one of the two Ag ions. Compared to Morten and Preston's prediction (1831 MHz for Ag) 75 % of the unpaired spin density resides on the two Ag ions [66-67]. Some additional unpaired spin density may be on oxygen ions surrounding the substitutional Ag ion, but that represents a small portion of the unpaired spin. If the two Ag ions were in the two closest lithium sites in the crystal lattice, each would be coordinated by five oxygen ions, and share coordination with a single O3 ion. In that situation, we would expect that more of the unpaired spin density would fall on coordinating oxygen ions, particularly the shared O3 ion. The fact that nearly all the unpaired spin density resides on of the two Ag ions suggest an interstitial site must be involved.

When Ag-doped $Li_2B_4O_7$ is x ray irradiated at 77 K, the $[Ag_i - Ag_{Li}]^0$ EPR spectrum does not appear in the crystal EPR spectrum. At 77 K the $[Ag_i - Ag_{Li}]^+$ defect traps two electrons forming the $[Ag_i - Ag_{Li}]^-$charge state of the defect. The two trapped electrons pair (S=0), and the defect is not paramagnetic in the 1− charge state. When the crystal is warmed to near 30 °C one of the trapped electrons is thermally released, and the defect takes on the neutral charge state, $[Ag_i - Ag_{Li}]^0$. In the neutral charge state, the second trapped electron is thermally stable to much higher temperatures. Observation of neutron irradiated $Li_2B_4O_7$:Ag suggests that the neutral charge state may be stable to temperatures nearing 230 °C [53].

3.2 Electron trap: interstitial silver ions in an otherwise defect free lattice

While an interstitial Ag^+ ion is a positive defect relative to a defect free lattice and as such requires a compensating negatively charged defect (lithium vacancy), in some instances the compensating lithium vacancy is distant enough that the electron trapped on the interstitial Ag^+ ion appears to be in an otherwise defect free lattice. In this case, the interstitial Ag^+ ion has a net 1+ charge relative to a defect free lattice. This isolated interstitial Ag^+ ion is abbreviated as $[Ag_i - Li]^+$ due to the observed lithium hyperfine contribution to the EPR spectrum when an electron is trapped at the defect.

Figure 26 shows the EPR spectrum for $[Ag_i - Li]^0$. $[Ag_i - Li]^0$ is an electron trapped at a $[Ag_i - Li]^+$ defect. The spectrum was obtained with the magnetic field aligned with the [001] direction of the crystal and a magnetic field of 9.34 MHz. Again the 16-line hyperfine spectrum is due to electrons trapped at interstitial silver atoms perturbed by lithium vacancies. While the four sets of four lines at 305, 310, 360 and 363 mT are due to a $[Ag_i - Li]^0$ trapped electron. The wide, 50-60 mT splitting is due to the Ag hyperfine, while the smaller 2.5 mT splitting is due to Li super-hyperfine. The spectrum was obtained after the $Li_2B_4O_7$:Ag crystal was x ray irradiated at room temperature. Under these conditions, the $[Ag_i - Li]^+$ defect traps two electrons forming a $[Ag_i - Li]^-$ trap with a set of paired electron in the non-paramagnetic S = 0 state. Indeed, after room temperature x ray irradiation, no EPR spectrum is visible for the $[Ag_i - Li]^-$ trapped electrons, see Figure 23. When the crystal is then warmed to near 120 °C, one of the trapped electrons is thermally released, and the remaining $[Ag_i - Li]^0$ trapped electron has the EPR spectrum shown in Figure 26.

To obtain Figure 26 the crystal was bleached with 90 seconds of 442 nm laser light using a He-Cd laser at 150 mW. The $[Ag_i - Ag_{Li}]^0$ and $[Ag_i - V_{Li}]^-$ trapped electrons both have a stronger oscillator strength for 442 nm bleaching than the $[Ag_i - Li]^0$ defect. The 442 nm bleaching nearly eliminates the $[Ag_i - Ag_{Li}]^0$ EPR spectrum which collocates with the 360 and 363 mT portions of the $[Ag_i - Li]^0$ EPR spectrum. Additionally, the $[Ag_i - V_{Li}]^-$ spectrum is reduced in intensity by the 442 nm laser bleaching to about three times the intensity of the $[Ag_i - Li]^0$ EPR spectrum.

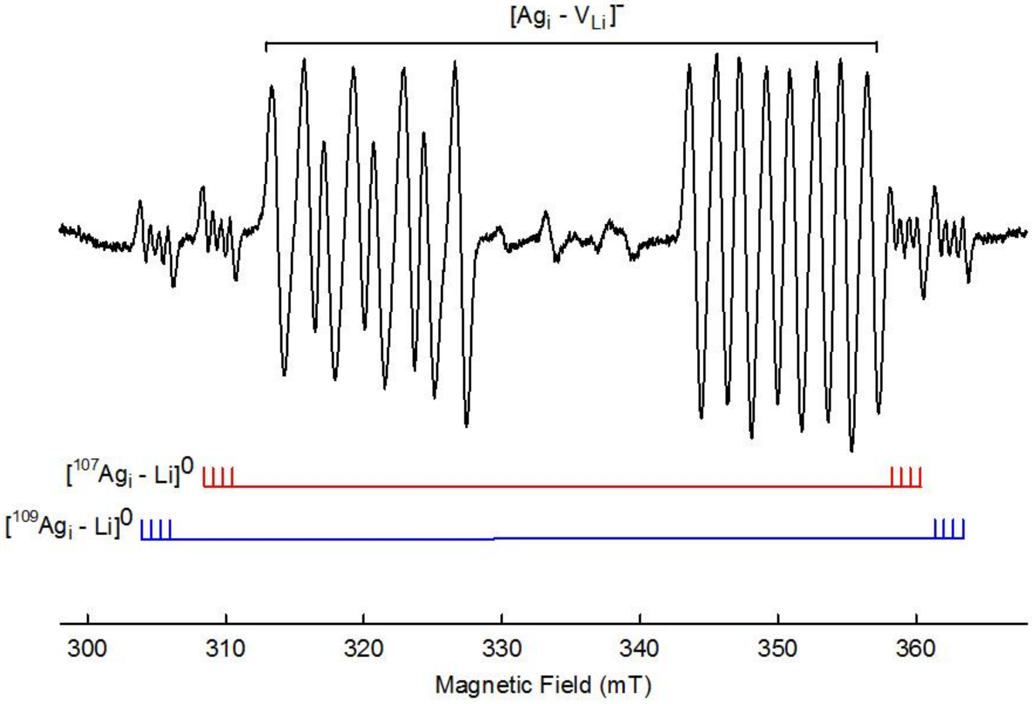

Figure 26. EPR spectrum of $[Ag_i - Li]^0$ in $Li_2B_4O_7$ crystal. The spectrum taken after an x-ray irradiation at room temperature followed by heating the crystal to 120 °C for 2 minutes followed by 90 seconds of 442 nm laser irradiation in the EPR cavity. The magnetic field was along the [001] direction and the microwave frequency was 9.40 GHz. Spectrum taken at room temperature.

The ratio of the splitting between the $[^{107}Ag_i - Li]^0$ spectra and the splitting between the $[^{109}Ag_i - Li]^0$ spectra is 0.8644, which agrees well with the ratio of the nuclear magnetic moments of ^{107}Ag to ^{109}Ag of 0.8682. This confirms that the hyperfine splitting is due to silver nuclei.

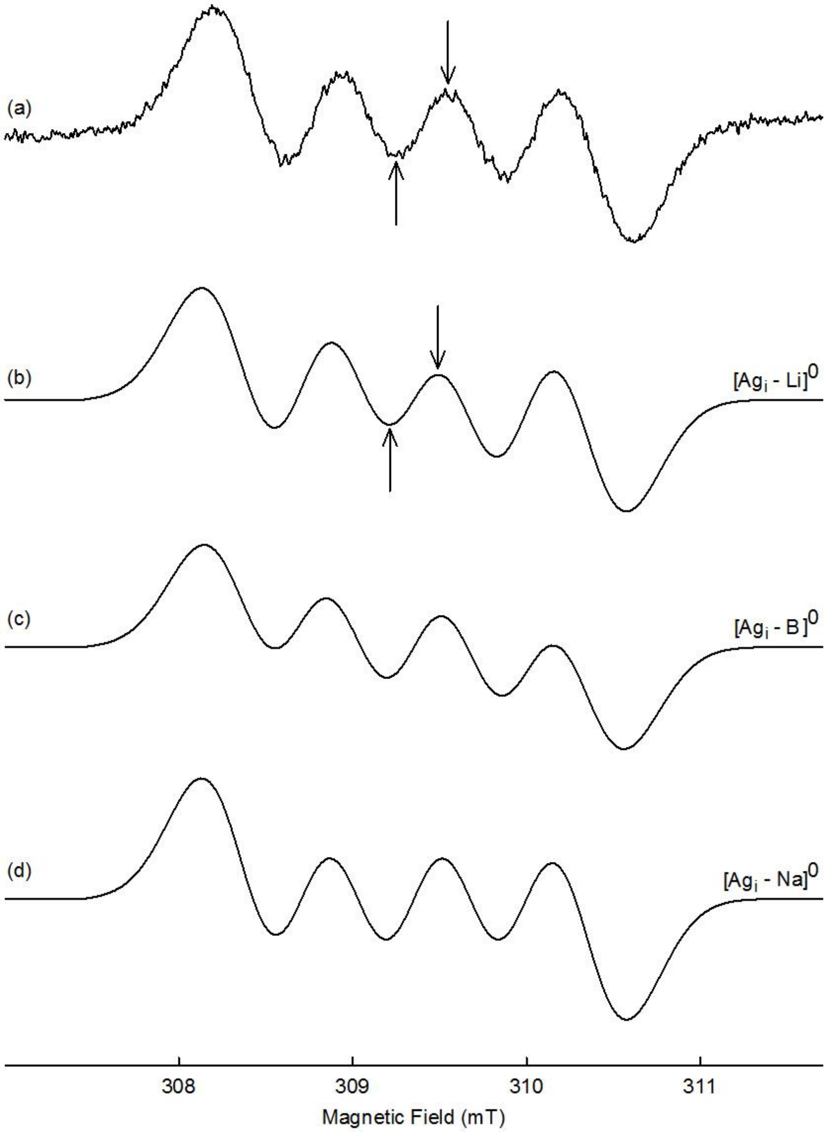

Figure 27. (a) Expanded view of the low field half $[^{107}Ag_i - Li]^0$ electron trap spectrum. The magnetic field was along the [001] direction and the microwave frequency was 9.40 GHz. Spectrum taken at room temperature. (b), (c) and (d) simulations of the low half of $[Ag_i - Li]^0$, $[Ag_i - B]^0$, and $[Ag_i - Na]^0$ electron traps respectively.

Simulations of the $[Ag_i - Li]^0$ ER spectrum resulted in good agreement to the experimentally obtained spectrum. Simulations were produced using the SimFonia computer program from Bruker. Figure 27 shows the results of the simulation. Only the lower half of the $[^{107}Ag - Li]^0$ EPR spectrum is displayed. There are three potential 3/2 spin nuclei in the Ag-doped $Li_2B_4O_7$ crystal. ^{11}B, ^{7}Li and ^{23}Na are all present in the crystal with a nuclear spin of 3/2. The boron and lithium isotopes are a natural part of the $Li_2B_4O_7$ crystal, and sodium is introduced as an impurity during growth through the use of a sodium containing flux. The presence of sodium was also confirmed though neutron activation of other crystals from the same boule. Although all three isotopes have 3/2 spin, they do not produce the same EPR spectra. Na has a 100 % abundant spin 3/2 isotope, Figure 27 (d), which produces a four line hyperfine spectrum in which all four lines are vertically centered on the spectrum baseline. The Na ion EPR spectrum does not have the stair-stepping down with magnetic field strength spectrum shown in the experimental spectrum, Figure 27 (a). Whereas the hyperfine contribution of both of the lesser abundant isotopes, ^{10}B ($I = 3$) and ^{6}Li ($I = 1$), produces the stair stepping down spectrum, Figure 27 (c) and Figure 27 (b), matching the same feature in the experimental spectrum, Figure 27 (a). Careful observation of the relative intensities of the four hyperfine lines shows that only the lithium spectrum, matches these relative intensities. See the arrows in Figure 27 (a) and Figure 27 (b).

Figure 28 displays a defect model for the $[Ag_i - Li]^0$ electron trap. The interstitial Ag ion is placed in the same position as in the $[Ag_i - Ag_{Li}]^0$ electron trap for the same reasons. It is likely that the interstitial Ag ion would be offset from the c axis position toward one of the two nearest Li ions due to the low immediate symmetry of the crystal, thereby yielding the $[Ag_i - Li]^+$ defect.

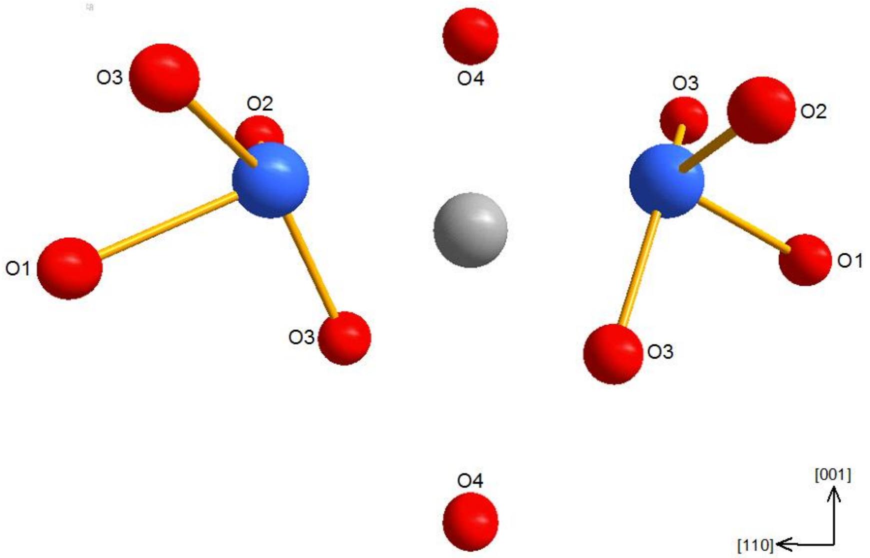

Figure 28. Model of the $[Ag_i - Li]$ electron trap. Lithium ions are blue, oxygen ions are red, and the silver ion is gray.

An electron trapped on the Ag ions in the $[Ag_i - Li]^0$ defect ($4d^{10}5s^1$) would not display much angular dependence in the g or hyperfine matrices due to the largely s nature of the unpaired electron. Indeed, the g matrix is nearly isotropic for the $[Ag_i - Li]^0$ defect, and the hyperfine matrix shows little variation in a [001] to [100] rotation of the applied magnetic field. Furthermore, the measured value of the hyperfine parameter for the ^{109}Ag is 1618 MHz from Figure 26. This is in good agreement with the typical splittings reported for $^{109}Ag^0$ atoms (1300-2100 MHz) [65]. Nearly all the unpaired spin is present on the Ag ion. Compared to Morten and Preston's prediction (1831 MHz for Ag) 88 % of the unpaired spin density resides the Ag ion [66-67]. Some unpaired spin density resides on the Li ion, 10-20 %, and any additional unpaired spin density may be on oxygen ion surrounding the substitutional Ag ion, but that represents a small portion of the unpaired spin. Again, this suggests an interstitial Ag ion must be involved.

The maximum intensity of the $[Ag_i - Li]^0$ trapped electron EPR spectrum occurs after heating to 175 °C. At temperatures above 175 °C, the electron trapped at $[Ag_i - Li]^0$ is thermally released, and the defect resets to the $[Ag_i - Li]^+$ state.

3.3 Electron trap: interstitial silver ions nearby lithium vacancies

In previous work, the 16-line hyperfine spectrum visible near 335 mT in Figure 23 was reported to be an interstitial Ag^+ ion trapping a hole forming an interstitial Ag^0 atom. The Ag^0 atom shared unpaired spin density with a nearby 3/2 nucleus creating the 16-line hyperfine spectrum [6]. EPR spectra of x-ray-irradiated-Ag-doped-^{10}B-enriched $Li_2B_4O_7$ conclusively demonstrates that the 3/2 nucleus contributing to the 16-line hyperfine spectrum of the Ag^0 atom is boron. Furthermore, charge neutrality suggest that the interstitial Ag^+ ion requires a compensating 1− defect in the as grown $Li_2B_4O_7$:Ag crystal. The lithium vacancy is just such a 1− defect, and the resulting defect pair would be neutral relative to the defect free lattice $[Ag_i - V_{Li}]^0$. While charge compensation can be distant from the interstitial Ag^{1+} ion, see Section 3.2, it may also be very near the interstitial Ag^+ ion. If the lithium vacancy is contained in one of the LiO_4 polyhedra directly accessible to the interstitial $Ag1^+$ ion or accessible by lithium ion movement within the polyhedra, it seems likely that lithium ions within the polyhedra would shift as necessary to facilitate the interstitial Ag^+ ion occupying the empty lithium lattice position becoming a substitutional Ag^+ ion. The nearby lithium vacancy must be in a position nearby the interstitial Ag^{1+} yet inaccessible to the interstitial Ag^{1+} ion.

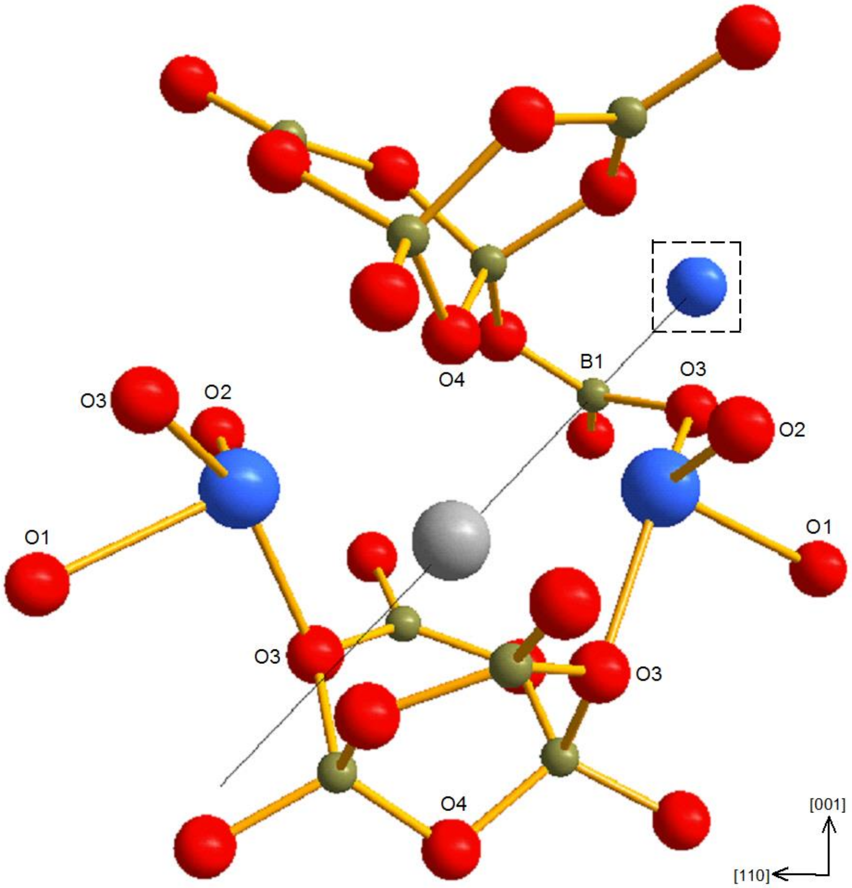

Figure 29. Model of a [Ag_i − V_{Li}]$^-$ electron trap. The lithium vacancy is in the dashed box. Lithium ions are blue, boron ions are green, oxygen ions are red, and the silver ion is gray.

Figure 29 shows a defect model for the [$Ag_i - V_{Li}$]$^-$ electron trap. The model is very similar to the model suggested for the Ag related electron traps outlined in sections 3.1 and 3.2. The lithium vacancy, dashed box, is placed in the lithium site closest to the interstitial Ag that is not within an LO_4 polyhedra accessible to the interstitial Ag^{1+} ion. A straight line connecting the lithium vacancy to the interstitial Ag ion runs directly through a B1 ion. If an interstitial Ag^+ ion moves toward the 1− lithium vacancy, the interstitial moves directly toward the intervening B1 ion. This movement would facilitate partition of the unpaired spin between the interstitial Ag^{1+} ion and the B1 ion after trapping a hole under ionizing radiation. This model for the $[Ag_i - V_{Li}]$ defect and the models for the $[Ag_i - Ag_{Li}]$ and $[Ag_i - Ag_{Li}]$ defects, proposed in section 3.1 and 3.2, are subtle variation of the local environment on the same Ag^{1+} interstitial site.

3.4 Thermoluminescence (TL)

Most recent investigation of thermoluminescence Ag-doped $Li_2B_4O_7$ focus on what is considered the main TL peak near 150 °C [6, 9-10, 13, 15]. Although a few other investigations have identified the existence of TL peaks at temperatures other than 150 °C [51-53], also see Chapter III. Also, Doull notes a slight shift to lower temperature for the main TL peak in Cu and Ag co-doped $Li_2B_4O_7$ [68]. As shown in Figure 30, the Ag-doped $Li_2B_4O_7$ crystal also shows a TL peak at 150 °C. The TL data in Figure 30 were obtained at a heating rate of 1°C/s after x ray irradiation at room temperature. A series of 25 °C heating steps followed by recording the intensity of EPR spectra were performed to identify the role played by the three silver related electron traps in the recombination process. The heating steps were 50, 75, 100, 125, 150, 175, 200 and 225 °C. After initial recording of the EPR spectrum intensities at room temperature before any annealing, the crystal was placed in a preheated (50 °C) single zone furnace for 23 seconds and rapidly cooled back to room temperature. The sample was then transferred to the EPR spectrometer and EPR spectrum intensities were recorded at room temperature. This process was repeated for each temperature step. The effective heating rate of the heating steps was 1.09 °C /s. The relative intensities of the trapped holes in Figure 30 were normalized to the peak intensity of the isolated Ag^{2+} trapped hole. The initial intensity of the $[Ag_{Li} - V_{Li}]^+$ trapped hole was 1/4th of the isolated Ag^{2+} trapped hole. The relative intensities of the trapped electrons in Figure 30 were normalized to the peak intensity of the $[Ag_i - V_{Li}]^-$ trapped electron.

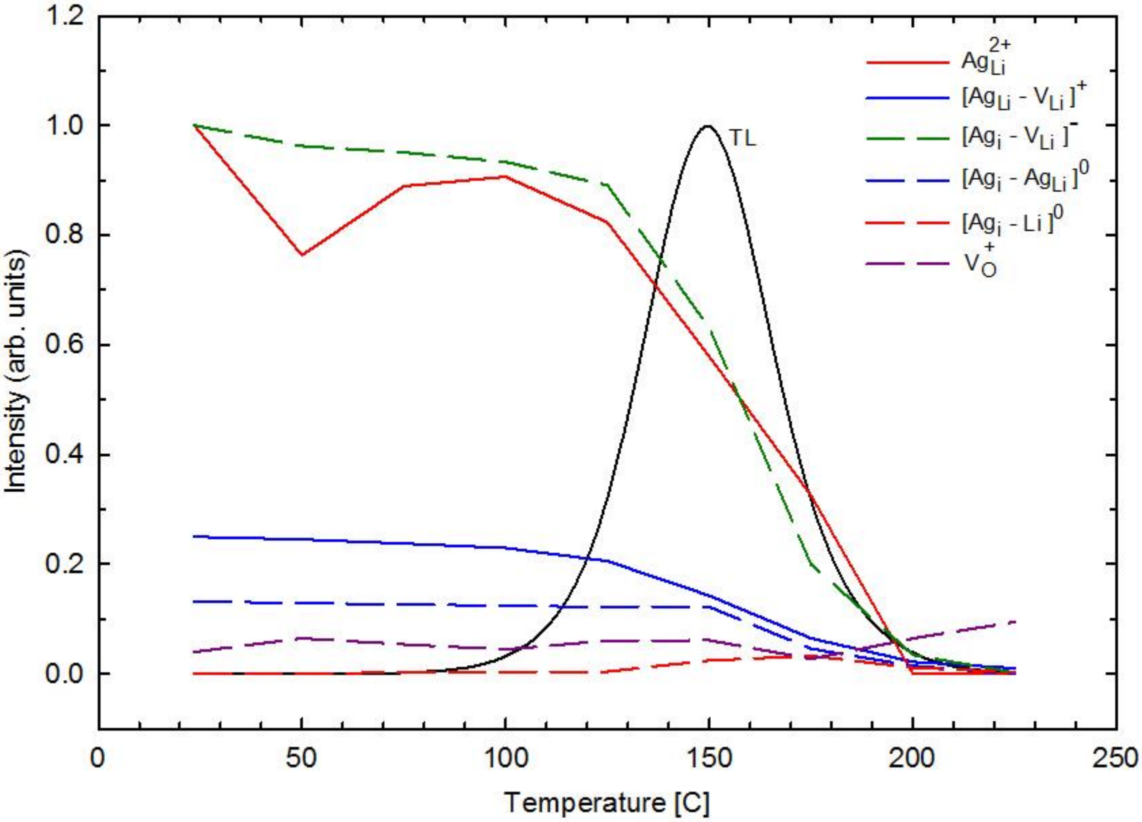

Figure 30. Thermoluminescence from Ag doped $Li_2B_4O_7$ crystal after an irradiation at room temperature with x rays. The TL peak occurs at 150 °C (the heating rate was 1 °C/s). The TL glow curve is black. The intensities of the EPR signals from isolated Ag^{2+} ions (red curve), $[Ag_{Li} - V_{Li}]^0$ defect pairs (blue curve), $[Ag_i - V_{Li}]^-$ electron traps (green dashed curve), $[Ag_i - Ag_{Li}]^0$ electron traps (blue dashed curve), $[Ag_i - Li]^0$ electron traps (red dashed curve), and V_O^+ electron traps (purple dashed line) were monitored in a separate experiment following a similar irradiation at room temperature with x rays.

Initially, the Ag_{Li}^{2+} EPR spectrum decreases from 30-50 °C, and then increases from 50-100 °C, finally from 100-200 °C it decreases continually until completely gone. The $[Ag_{Li} - V_{Li}]^0$ EPR spectrum is unchanged from 30-100 °C, and decreases, albeit at different rates, from 100-200 °C. At 225 °C a small amount of the $[\mathrm{Ag_{Li}} - \mathrm{V_{Li}}]^0$ EPR spectrum is still visible. The $[\mathrm{Ag_i} - \mathrm{V_{Li}}]^-$ EPR spectrum decreases slowly from 30-125 °C, decreases more rapidly from 125-175 °C, and decreases until gone from 175-225 °C. The $[\mathrm{Ag_i} - \mathrm{Ag_{Li}}]^0$ EPR spectrum is unchanged from 30-175 °C, and decreases until gone from 175-225 °C. The $[\mathrm{Ag_i} - \mathrm{Li}]^0$ EPR spectrum is not visible thru 125 °C. From 125-175 °C it increases to its maximum. The spectrum decreases from 175-225 °C, but is not completely gone at 225 °C. Finally, the isolated $\mathrm{V_O}^+$ EPR spectrum increases from 30-50 °C, decreases from 50-100 °C, increases again from 100-150 °C, decreases from 150-175 °C, and finishes by increasing continually from 175-225 °C.

4. Discussion of the TL mechanism

The $[\mathrm{Ag_i} - \mathrm{Ag_{Li}}]^0$ trapped electron, the isolated $\mathrm{V_O}^+$ trapped electron, and the $[\mathrm{Ag_{Li}} - \mathrm{V_{Li}}]^0$ trapped hole are thermally stable to at least 225 °C, see Chapter III and [53]. Any decrease in intensity of the EPR spectrum of these three trapped charges must correspond to net recombination at the site of the thermally stable trap. The simplest charge trap to monitor in order to understand the net flow of trapped charge in the x ray irradiated crystal is the isolated $\mathrm{V_O}^+$ electron trap. From 30-50 °C additional electrons are trapped at the isolated oxygen vacancies. Another electron trap must be thermally releasing electrons. In this temperature range perturbed oxygen vacancy trapped electron are thermally released, see Chapter III. The thermally released electrons re-trap at isolated oxygen vacancies, but also recombine with trapped holes yielding the $\mathrm{Ag_{Li}}^{2+}$ EPR spectrum decrease over the same temperature.

While the isolated oxygen vacancy EPR spectrum decreases from 50-100 °C, holes are being thermally released in the crystal from isolated lithium vacancies over this temperature range, see Chapter III. These thermally released holes recombine with electrons trapped at isolated oxygen vacancies and $[\mathrm{Ag_i} - \mathrm{V_{Li}}]^-$ yielding a decreased EPR spectra for both defects. The thermally released holes are also re-trapped at the $\mathrm{Ag_{Li}}^+$ defect site yielding an increase in $\mathrm{Ag_{Li}}^{2+}$ EPR spectrum from 50-100 °C.

From 100-150 °C, the EPR spectrum for isolated oxygen vacancies increases. Over this temperature range electrons are being thermally released in the crystal and re-trapping at isolated oxygen vacancy defects ($\mathrm{V_O}^{2+}$) yielding an increase in the $\mathrm{V_O}^+$ EPR spectrum. Over this temperature range trapped electrons are being thermally released from $[\mathrm{Ag_i} - \mathrm{V_{Li}}]^-$ defects. The decrease in the $[\mathrm{Ag_i} - \mathrm{V_{Li}}]^-$ EPR spectrum follows. The thermally released electrons re-trap at isolated oxygen vacancies, but also recombine at trapped hole sites. The EPR spectra for holes trapped at both $\mathrm{Ag_{Li}}^{2+}$ and $[\mathrm{Ag_{Li}} - \mathrm{V_{Li}}]^0$ both decrease over this temperature range due to electron hole recombination at the hole trapping defects.

From 125-175 °C, the $[\mathrm{Ag_i} - \mathrm{Li}]^0$ EPR spectrum increases from zero to its maximum value. One of the two electrons trapped at the $[\mathrm{Ag_i} - \mathrm{Li}]^-$ defect is thermally released yielding the paramagnetic $[\mathrm{Ag_i} - \mathrm{Li}]^0$ trapped electron.

From 150-175 °C the isolated oxygen vacancy EPR spectrum decreases. Again holes are being thermally released in the crystal over this temperature range. The decrease in the $[\mathrm{Ag_i} - \mathrm{Ag_{Li}}]^0$ defect intensity confirms holes are being thermally released. However, the decrease of the EPR spectrum for $[\mathrm{Ag_{Li}} - \mathrm{V_{Li}}]^0$ indicates the thermal release of electron over the same temperature range. Both electron and holes are being thermally released over the range of 150-175 °C. More holes than electron are being released thus the net decrease in the number of electron trapped at isolated oxygen vacancies. Ag_{Li}^{2+} defects are thermally releasing holes, and are completely annealed by 200 °C. $[Ag_i - V_{Li}]^-$ defects continue to thermally release electrons until completely annealed by 225 °C. The long temperature range of electron release for $[Ag_i - V_{Li}]^-$ defects, 100-225 °C, suggest the presence of two slightly different $[Ag_i - V_{Li}]^-$ defects. The decrease in the rate of thermal release of electrons trapped at $[Ag_i - V_{Li}]^-$ defects at 175 °C, indicated by the reduced downward slope of the decrease in EPR intensity, also suggest the presence of two very similar defects. In fact, in Cu-doped $Li_2B_4O_7$ two very similar interstitial Cu electron traps have been identified [11].

Finally, from 175-225 °C the EPR spectrum for isolated oxygen vacancy trapped electrons increases. Over this temperature range more electrons are thermally released than holes. The complete annealing of Ag_{Li}^{2+} trapped holes and continued decrease of the $[Ag_i - Ag_{Li}]^0$ trapped electron EPR spectrum confirms the thermal release of some holes. It is not clear if the decrease in the $[Ag_i - Li]^0$ EPR spectrum indicates recombination of holes with electrons trapped at this site. It is however likely given the $[Ag_i - Li]^0$ EPR spectrum is still visible after heating to 225 °C. The complete annealing of the $[Ag_i - V_{Li}]^-$ trapped electrons and decrease in $[Ag_{Li} - V_{Li}]^0$ EPR spectrum, demonstrates that electrons are being thermally released from the $[Ag_i - V_{Li}]^-$ defect and some of those electrons are recombining with trapped holes at the $[Ag_{Li} - V_{Li}]^0$ defect. At 225 °C three EPR spectra are still visible: the isolated oxygen vacancy (V_O^+) trapped electron, the $[\mathrm{Ag_{Li}} - \mathrm{V_{Li}}]^0$ trapped hole, and the $[\mathrm{Ag_i} - \mathrm{Li}]^0$ trapped electron. It is apparent that trapped electrons that are neutral or positive relative to the defect free lattice ($[\mathrm{Ag_i} - \mathrm{Ag_{Li}}]^0$, $[\mathrm{Ag_i} - \mathrm{Li}]^0$ and $\mathrm{V_O}^+$) are more thermally stable than trapped electrons that are negatively charged relative the defect free lattice ($[\mathrm{Ag_i} - \mathrm{V_{Li}}]^-$, $[\mathrm{Ag_i} - \mathrm{Ag_{Li}}]^-$, and $[\mathrm{Ag_i} - \mathrm{Li}]^-$). The trapped hole that is neutral relative to the defect free lattice ($[\mathrm{Ag_{Li}} - \mathrm{V_{Li}}]^0$) is also more stable than the trapped holes that are positively charged relative to the defect free lattice ($[\mathrm{Ag_{Li}}^{2+}]^+$).

5. Summary

Two new electron traps involving interstitial Ag^{1+} ions are identified by EPR spectroscopy. These two defects, $[\mathrm{Ag_i} - \mathrm{Ag_{Li}}]^+$, $[\mathrm{Ag_i} - \mathrm{Li}]^+$ can trap one or two electrons yielding the neutral and 1− states of each defect respectively. EPR hyperfine spectra of each of these 1− charge state defects and the previously known $[\mathrm{Ag_i} - \mathrm{V_{Li}}]^-$ trapped electron conclusively show the majority of the trapped electron unpaired spin resides on the interstitial silver atom. In fact, the more unpaired spin that resides on the interstitial silver atom, the greater the thermal stability of the trapped electron. Defect models are proposed for each of the three interstitial silver defects which are subtle variations on the same interstitial position. Furthermore, thermoluminescence and EPR are used to show the role of all known electron and hole traps in the main dosimetry peak of $\mathrm{Li_2B_4O_7}$:Ag. These results suggest that the by adjusting the Ag-doping level, the relative intensity of high and low temperature TL peaks may be controlled yielding less fading and a more useful dosimetry material.

VI. Copper-doped lithium triborate (LiB_3O_5) crystals: a photoluminescence, thermoluminescence, and electron paramagnetic resonance study

Abstract

When doped with copper ions, lithium borate materials are candidates for use in radiation dosimeters. Copper-doped lithium tetraborate ($Li_2B_4O_7$) crystals have been widely studied, but little is known thus far about copper ions in lithium triborate (LiB_3O_5) crystals. In the present investigation, Cu^+ ions ($3d^{10}$) were diffused into an undoped LiB_3O_5 crystal at high temperature (these ions occupy both Li^+ and interstitial positions in the crystal). A photoluminescence (PL) band peaking near 387 nm and a photoluminescence excitation (PLE) band peaking near 273 nm verify that a portion of these Cu^+ ions are located at regular Li^+ sites. After an irradiation at room temperature with x rays, electron paramagnetic resonance (EPR) spectra show that Cu^+ ions at Li^+ sites have trapped a hole and converted to Cu^{2+} ions ($3d^9$) while Cu^+ ions at interstitial sites have trapped an electron and converted to Cu^0 atoms ($3d^{10}4s^1$). Two distinct Cu^{2+} trapped-hole spectra are formed by the x rays (one due to isolated Cu^{2+} ions with no nearby defects and the other due to perturbed Cu^{2+} ions). A thermoluminescence (TL) peak appears at 120 °C with a maximum in the emitted light near 630 nm when the irradiated crystal is heated above room temperature. EPR shows that the TL peak occurs when trapped electrons are thermally released from interstitial Cu^0 atoms. Thermal quenching above room temperature prevents the electron-hole recombination at Cu^{2+} ions from contributing to the TL emission.

1. Introduction

Lithium triborate (LiB_3O_5) is a well-established nonlinear optical material widely used in frequency conversion applications ranging from the mid-infrared to the deep ultraviolet [69-71]. In recent years, this material has also been proposed as a possible candidate for radiation dosimeters [72-78]. Further investigation, however, is needed to determine if LiB_3O_5 can serve as a practical thermoluminescence (TL) dosimeter. A related borate compound, lithium tetraborate ($Li_2B_4O_7$), is known to be an excellent TL dosimeter material when doped with copper [5, 10, 16-17, 79-80]. Because of the similarities of the two materials (LiB_3O_5 and $Li_2B_4O_7$), we have initiated a comprehensive study of copper in LiB_3O_5, with the goal of establishing whether or not copper ions behave the same in the two materials. Interest in both materials also arises because the ^{6}Li and ^{10}B nuclei have large cross-sections for thermal neutron absorption (enrichment with either or both isotopes may allow these materials to be used as neutron detectors).

Our focus on copper is a result of the unique role played by Cu^+ ions in the TL response of doped $Li_2B_4O_7$. These monovalent ions serve as both hole traps and electron traps during an exposure to ionizing radiation [11]. The diametrically opposite behaviors occur because Cu^+ ions are located at two different sites in the $Li_2B_4O_7$ crystals. When substituting for Li^+ ions, the Cu^+ ions trap holes and become Cu^{2+} ions. The Cu^+ ions also occupy interstitial sites where they trap electrons and become Cu^0 atoms. During a subsequent heating after an irradiation, electrons are thermally released from Cu^0 centers and recombine with holes at the Cu^{2+} ions. This produces an intense TL signal in

$Li_2B_4O_7$ because electron-hole recombination at the Cu^{2+} sites is primarily radiative. Similar behavior has been reported for Ag^+ ions in $Li_2B_4O_7$ crystals [6, 30].

In the present paper, we identify the Cu-related electron and hole trapping sites in LiB_3O_5 that are active during an exposure to ionizing radiation, and we also explore the recombination process when charge is thermally released by heating above room temperature. Diffusion at 650 °C is used to introduce Cu^+ ($3d^{10}$) ions into a previously grown undoped crystal. The Cu^+ ions occupy both substitutional Li^+ sites and interstitial sites in the LiB_3O_5 crystal. Complementary optical and magnetic resonance characterization techniques are then applied. These are optical absorption, photoluminescence (PL), photoluminescence excitation (PLE), thermoluminescence (TL), and electron paramagnetic resonance (EPR). The PL and PLE results verify that Cu^+ ions are present at Li^+ sites in the diffused crystal. After irradiating at room temperature with x rays, EPR spectra show that Cu^+ ions at Li^+ sites have trapped a hole (Cu^{2+} ions are formed) and Cu^+ ions at interstitial sites have trapped an electron (Cu^0 atoms are formed). A TL peak near 120 °C corresponds to the release of electrons from the Cu^0 traps. Surprisingly, the spectral dependence of the TL signal peaks near 630 nm, thus showing that this TL-related radiative recombination is not occurring at the Cu^{2+} ions.

2. Experimental

Lithium triborate (LiB_3O_5) crystals have an orthorhombic structure (space group Pna21) for all temperatures below their 834 °C melting point. At room temperature, lattice constants are a = 8.447 Å, b = 7.3789 Å, and c = 5.1408 Å [81-83]. There are three inequivalent boron sites and five inequivalent oxygen sites in LiB_3O_5 (all the lithium sites are equivalent). The 36 atoms in a unit cell separate into four sets of nine atoms that transform into each other according to the symmetry elements of the crystal [37]. More generally, the LiB_3O_5 crystals are best described as helices of fully connected $(B_3O_7)^{5-}$ groups separated by Li^+ cations [71]. Each $(B_3O_7)^{5-}$ anionic group has two boron ions that are part of BO_3 units and one boron ion that is part of a BO_4 unit. A “ball-and-stick” representation of this basic building block is shown in Figure 31.

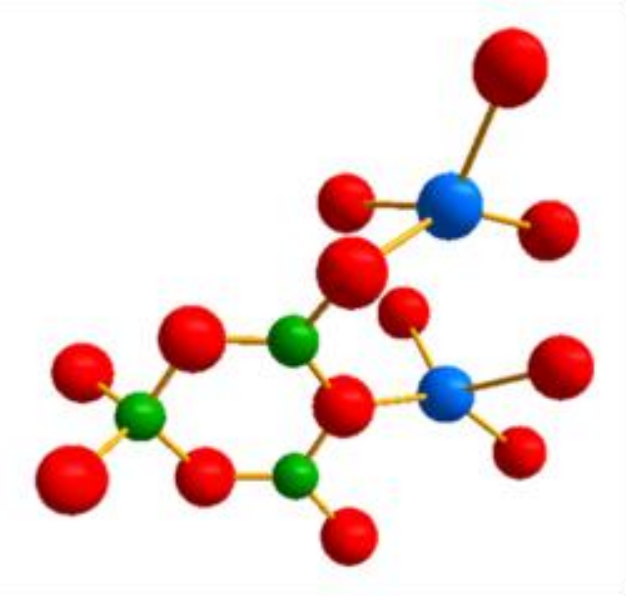

Figure 31. Schematic representation of the basic $(B_3O_7)^{5-}$ anionic group in the LiB_3O_5. This view is along an arbitrary direction in the crystal. Two of the equivalent lithium sites are also shown. Boron ions are green, oxygen ions are red, and the lithium ions are blue.

The sample used in our optical and EPR experiments was rectangular in shape and had nominal dimensions of 2.5 x 3 x 3.5 mm^3 along the a, b, and c axes, respectively. The following process was used to diffuse copper into an undoped LiB_3O_5 crystal. After wrapping a single layer of copper foil (0.0125 mm thick) around a sample, it was placed in a one-zone tube furnace and heated to 650 °C in a static air atmosphere. The sample, surrounded by copper, was held at this temperature for 11 h, and then was quickly cooled to room temperature. At the high temperature, copper enters the crystal as close-shelled Cu^+ ions and occupies Li^+ sites and interstitial spaces. A mismatch in both size and charge prevents Cu^+ ions from occupying B^{3+} sites. It is not known if the copper was uniformly distributed within our diffused crystal.

A Horiba Fluorolog-3 spectrometer was used to collect the PL and PLE spectra (slits for the excitation and emission monochromators were set at 10 nm resolution). PL spectra were not corrected for system response. A Bruker EMX spectrometer operating near 9.40 GHz was used to collect the EPR spectra. An Oxford helium-gas flow system controlled the temperature of the sample and magnetic fields were measured using a Bruker teslameter. Optical absorption spectra were obtained using a Cary 5000 spectrophotometer. A Harshaw TLD-3500 reader provided the TL "glow" curve (the heating rate was 1 °C/s). The spectral dependence of the TL emission was obtained using an ANDOR Shamrock 193i spectrograph coupled to an iDus 420 CCD camera (the sample was heated at a constant rate with an Instec HCS621G stage). An OEG-76H x-ray tube from Varian (operating at 60 kV and 30 mA) was used to convert the Cu^+ ions to Cu^{2+} ions and Cu^0 atoms. The duration of each irradiation was three minutes.

3. Optical and magnetic resonance results

3.1. Photoluminescence (PL and PLE)

After diffusing Cu^+ ions into the LiB_3O_5 crystal, an intense PL emission band is observed at room temperature. This PL band peaks near 387 nm (3.20 eV) when the excitation light is 275 nm. Its full width at half maximum (FWHM) is 0.40 eV. The corresponding room-temperature PLE band, obtained by monitoring the emission at 385 nm, has a peak at 273 nm (4.54 eV) and a FWHM of approximately 0.43 eV. These PL and PLE bands are shown in Figure 32. Their Stokes shift is approximately 1.34 eV. The bands in Figure 32 were not present before the LiB_3O_5 crystal was diffused with copper. We assign the PLE band to the $3d^{10}$ to $3d^94s^1$ intracenter transition of Cu^+ ions substituting for Li^+ ions and the PL band to the Stokes-shifted $3d^94s^1$ to $3d^{10}$ emission (a two-level configurational coordinate diagram describes this localized excitation and emission). PL and PLE bands similar to those shown in Figure 32 have been previously attributed to Cu^+ ions substituting for Li^+ ions in $Li_2B_4O_7$ and $LiAlO_2$ crystals [5, 7, 10, 16, 58].

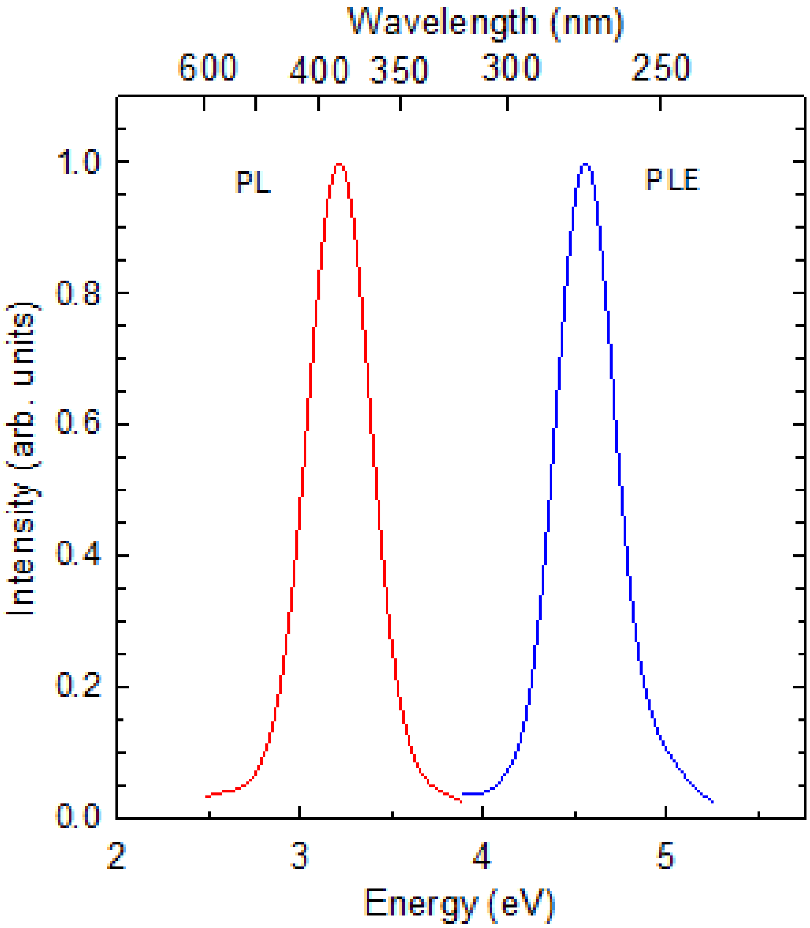

Figure 32. Photoluminescence (PL) and photoluminescence excitation (PLE) spectra from the Cu$^+$ ions in a copper-diffused LiB_3O_5 crystal. The PL (red curve) was taken with 275 nm excitation and the PLE (blue curve) was obtained by monitoring the emission at 385 nm.

The intensity of the PL emission band at 387 nm in the copper-diffused LiB_3O_5 crystal was monitored as the temperature was raised above room temperature. These results are shown in Figure 33. The data suggest that the PL signal from the Cu$^+$ ions is thermally quenched even at 75 °C (the intensity of this PL emission is expected to be much larger for temperatures below room temperature). The Cu$^+$ emission in LiB_3O_5 is nearly 100% quenched at 100 °C. For comparison, data taken under identical conditions from a Cu-doped $Li_2B_4O_7$ crystal are also shown in Figure 33. For this latter crystal, the intensity of the emission at 370 nm from Cu^+ ions [7] was recorded as the temperature was steadily increased. As seen in Figure 33, the Cu^+ emission in $Li_2B_4O_7$ does not begin to significantly quench until the temperature is above 200 °C.

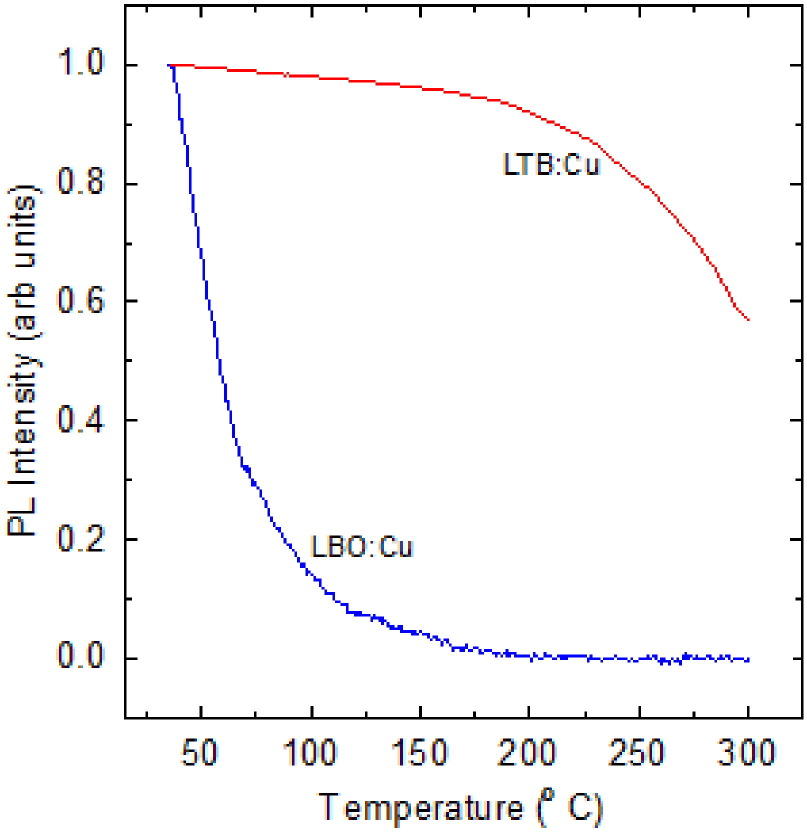

Figure 33. Thermal quenching of the PL emission from Cu^+ ions. A comparison of the copper-diffused LiB_3O_5 crystal (blue curve) and the copper-doped $Li_2B_4O_7$ crystal (red curve). The two curves are normalized at 35 °C.

3.2. Electron paramagnetic resonance (EPR)

Irradiating the copper-diffused LiB_3O_5 crystal at room temperature with x rays produces EPR signals from Cu^{2+} ($3d^9$) ions and Cu^0 ($3d^{10}4s^1$) atoms. Although the majority of the “free” electrons and holes created by the x rays quickly recombine in otherwise perfect regions of the crystal, a small portion become trapped at existing defects and create the EPR signals. The Cu^{2+} ions are at Li^+ sites in the crystal and are formed when a radiation-induced hole is trapped at a Cu^+ ion [84]. At the same time, the Cu^0 atoms are formed when a radiation-induced electron is trapped at an interstitial Cu^+ ion [11].

The EPR spectra of two distinct x-ray-induced Cu^{2+} ions are shown in Figure 34. These data were obtained at 25 K with the magnetic field along the *b* axis. Stick diagrams above and below the spectrum identify the lines belonging to separate Cu^{2+} centers. The red stick diagrams above the spectrum identify the lines from isolated Cu^{2+} ions (specifically, Cu^{2+} ions on Li^+ sites with no nearby perturbing point defects), whereas the blue stick diagrams below the spectrum identify lines from perturbed Cu^{2+} ions (those Cu^{2+} ions with a Li^+ vacancy at a nearest-neighbor Li site). Hyperfine interactions with the two stable isotopes of copper allow these spectra in Figure 34 to be unambiguously assigned to Cu^{2+} ions. The ^{63}Cu nuclei are 69.2% abundant with I = 3/2 and the ^{65}Cu nuclei are 30.8% abundant with I = 3/2. Two sets of hyperfine lines, with four lines in each set, are observed for each Cu^{2+} spectrum as a result of these I = 3/2 nuclear spins (the number of EPR lines in a set is given by 2I + 1). For a specific spectrum, the separations between the four ^{65}Cu lines are greater (by a small amount) than the separations between the four ^{63}Cu lines. This is a result of the magnetic moment of the ^{65}Cu nucleus being slightly larger than the moment of the ^{63}Cu nucleus. The different natural abundances of the two copper isotopes explain why ^{63}Cu lines are more intense than ^{65}Cu lines in Figure 34.

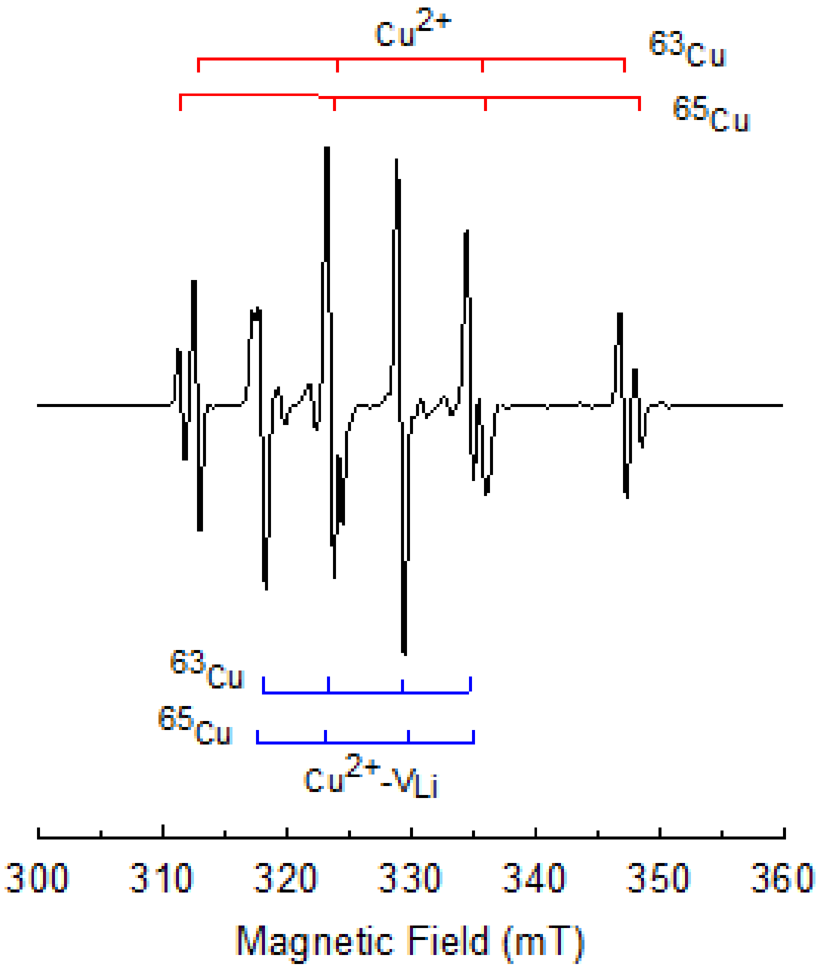

Figure 34. EPR spectra from Cu^{2+} ions in the copper-diffused LiB_3O_5 crystal. Data were taken at 25 K after irradiating the crystal at room temperature with x rays. The magnetic field is along the *b* axis and the microwave frequency is 9.398 GHz. Upper (red) stick diagrams are lines from the isolated Cu^{2+} ions and lower (blue) stick diagrams are lines from the perturbed Cu^{2+} ions.

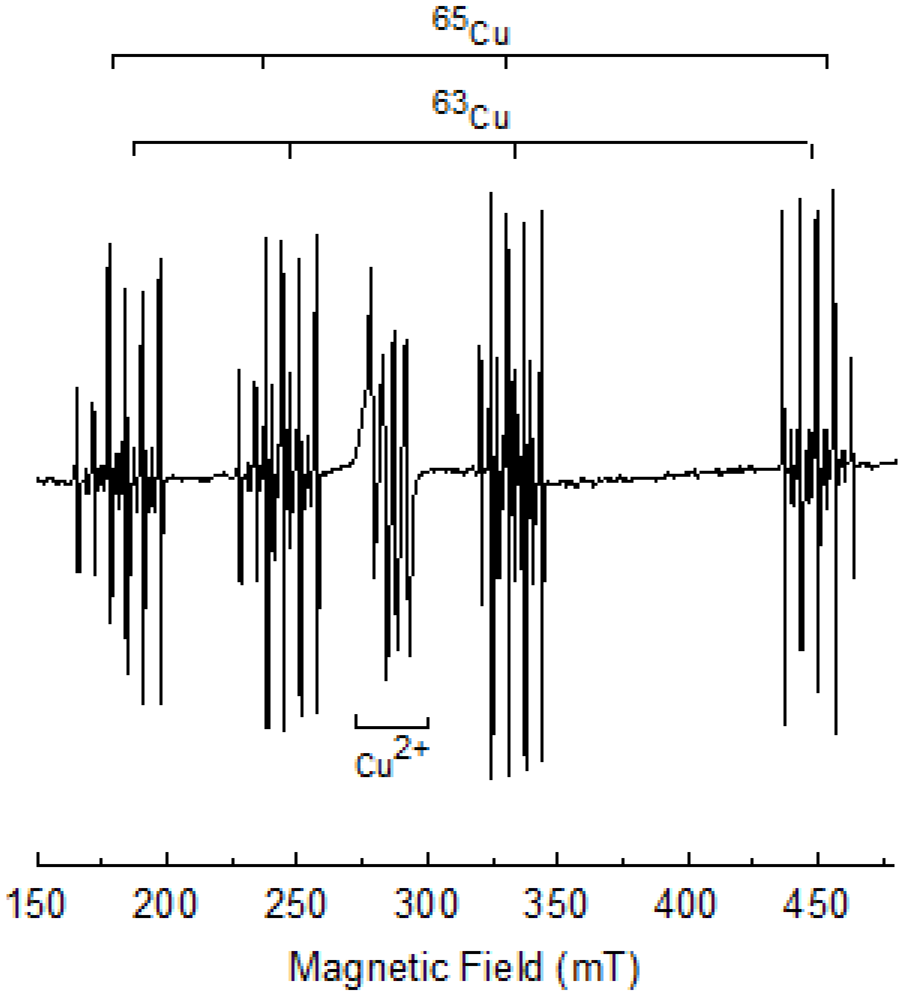

Figure 35. EPR spectrum from Cu^0 atoms in the copper-diffused LiB_3O_5 crystal. Data were taken at room temperature after irradiating the crystal at room temperature with x rays. The magnetic field is along the *c* axis and the microwave frequency is 9.397 GHz. Lines from both ^{63}Cu and ^{65}Cu nuclei are present in each of the four primary groups.

The EPR spectrum from the x-ray-induced Cu^0 atoms is shown in Figure 35. This spectrum was taken at room temperature with the magnetic field along the crystal's *c* axis. There are four widely separated groups of EPR lines in Figure 35, centered at approximately 185, 240, 335, and 450 mT. As indicated by the red and blue stick diagrams above the spectrum, these four groups are due to hyperfine interactions with

^{63}Cu and ^{65}Cu nuclei. The large Cu hyperfine parameters and their isotropic nature establish that the responsible defect is, to first order, a copper atom. Also present in Fig. 5 are a set of Cu^{2+} lines near 285 mT. A comparison of the Cu^{0} and Cu^{2+} spectra shows that the magnitude of the hyperfine interaction, as expected, is much larger for a Cu^{0} atom. This is because the unpaired spin is in a 4*s* orbital for the Cu^{0} atom and is in a 3*d* orbital for the Cu^{2+} ion. The larger interaction for the Cu^{0} atoms causes the separation between adjacent sets of lines to increase from low to high field in Figure 35.

Figure 36 is an expanded view of the lowest-field set of Cu^{0} EPR lines in Figure 35. Each Cu hyperfine line is split into additional superhyperfine lines by an interaction with a boron neighbor (lines from both ^{10}B and ^{11}B are resolved). The other sets of primary ^{63,65}Cu lines at higher fields in Figure 35 also have similar patterns due to the interactions with ^{10,11}B nuclei. As shown by stick diagrams above the spectrum in Figure 36, the ^{63}Cu line and the ^{65}Cu lines are separately split into a set of four lines due to an interaction with a ^{11}B nucleus (80.2% abundant, I = 3/2) at one nearby boron site and a set of seven lines due to the interaction with a ^{10}B nuclei (19.8% abundant, I = 3) at the same nearby boron site. This pattern of seven lines of smaller intensity and four lines of larger intensity is consistent with a boron interaction. The nuclear magnetic moment of ^{10}B is nearly three times smaller than the nuclear magnetic moment of ^{11}B, thus explaining why the^{10}B lines appear between the ^{11}B lines. A detailed analysis of the EPR spectra from these Cu^{2+} and Cu^{0} centers in LiB_3O_5, including the determination of their spin-Hamiltonian parameters, will be reported in a later publication.

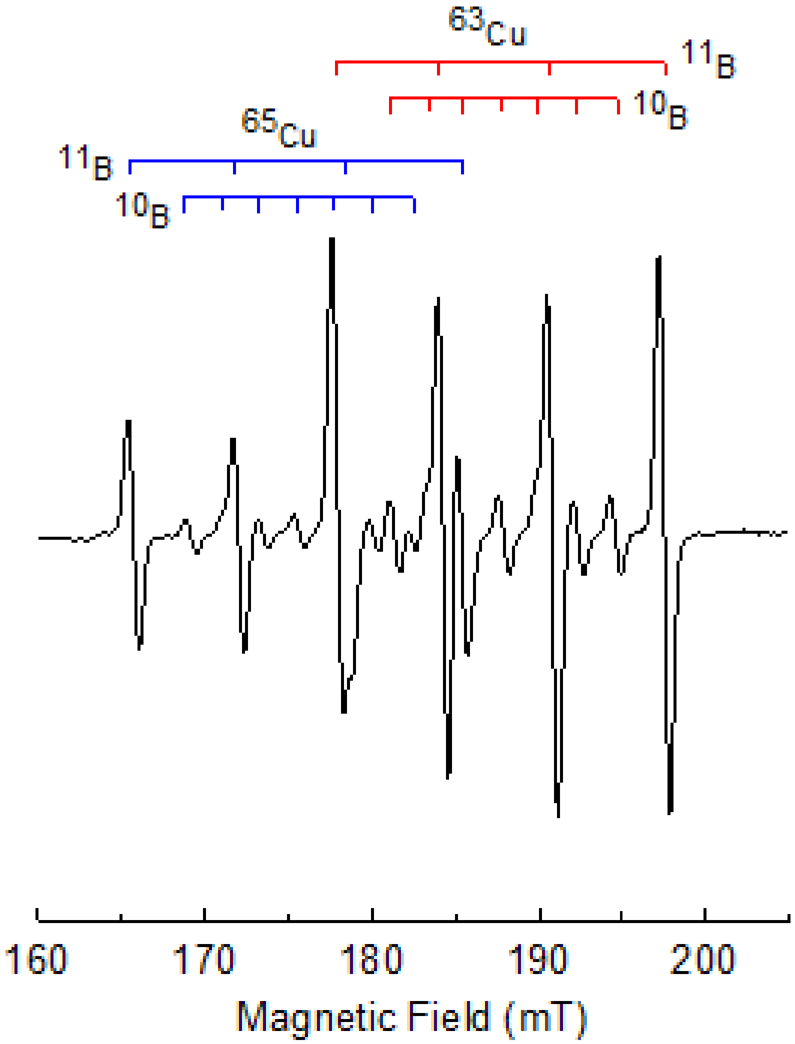

Figure 36. Expanded view of the lowest-field group of EPR lines in the Cu^0 spectrum from the copper-diffused LiB$_3$O$_5$ crystal (taken from Fig. 5). In addition to the ^{63}Cu (red) and ^{65}Cu (blue) hyperfine interactions, stick diagrams identify resolved hyperfine lines from ^{10}B and ^{11}B nuclei at one neighboring boron site.

3.3. Optical absorption

Optical absorption spectra from the LiB$_3$O$_5$ crystal diffused with copper are shown in Figure 37. These spectra were taken at room temperature using unpolarized light propagating along the *c* direction. The lower (blue) spectrum was taken from the as-diffused crystal and the upper (red) spectrum was taken after an irradiation at room temperature with x rays. Before the irradiation, the crystal had broad absorption bands peaking near 292 nm (4.25 eV), 254 nm (4.88 eV), and 226 nm (5.49 eV), with the 292 nm band being weakest and the 226 nm band being most intense. The defects responsible for these absorption bands are not unambiguously identified in our study (the bands are tentatively assigned to transitions from the ground state to different excited states of the Cu^+ ions). After the x-ray irradiation (red curve), additional absorption bands are present near 355 nm (3.49 eV) and 312 nm (3.97 eV). These latter two bands are most likely associated with the radiation-induced Cu^{2+} and Cu^0 defects seen with EPR (see Section 3.2). Singly ionized oxygen vacancies (V_O^+) have an optical absorption band near 300 nm (4.13 eV) in LiB_3O_5 [41], and they may also be contributing to the after-irradiation absorption spectrum (red curve) in Figure 37. Additional in-depth studies will help determine final assignments for these optical absorption bands appearing in the copper-diffused LiB_3O_5 crystal.

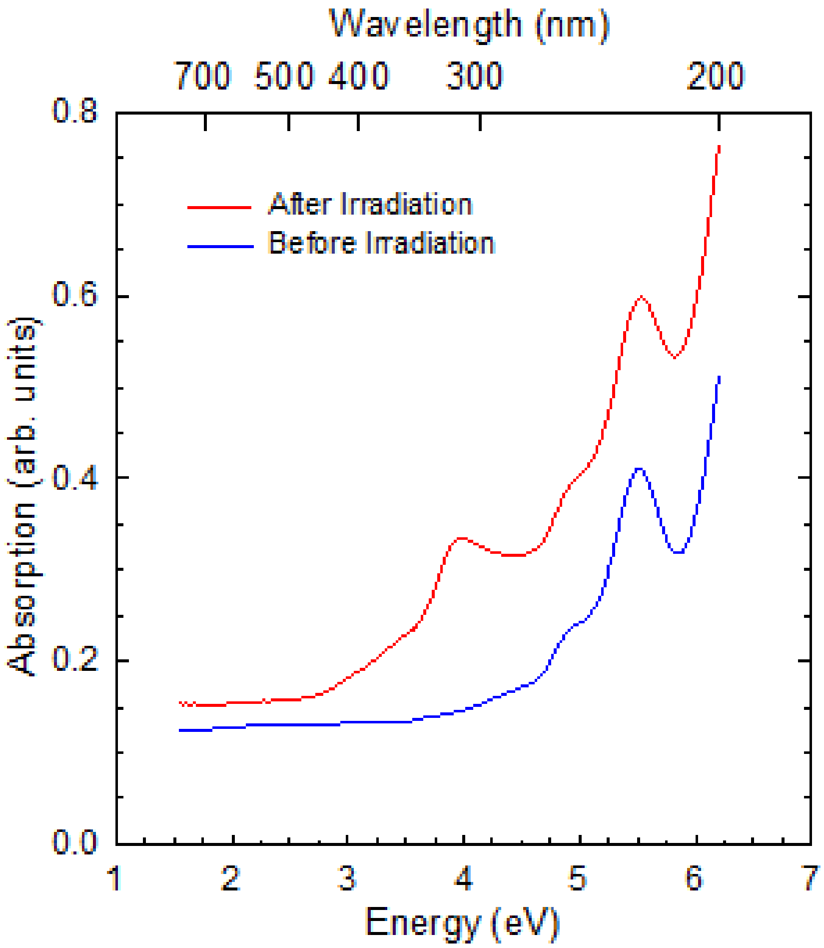

Figure 37. Optical absorption spectra from the copper-diffused LiB_3O_5 crystal. These data were taken at room temperature with unpolarized light propagating along the *c* direction. The lower (blue) curve was taken before an x-ray irradiation at room temperature. The upper (red) curve was taken after the irradiation with x rays.

3.4. Thermoluminescence (TL)

Recently, investigators [72, 75] reported that a thermoluminescence (TL) glow curve occurs near 120 °C when a LiB_3O_5 crystal containing copper is exposed at room temperature to ionizing radiation. As seen in Figure 38, our copper-diffused LiB_3O_5 crystal also shows this 120 °C TL peak (green curve). The TL data in Figure 38 were obtained with a heating rate of 1 °C/s after an irradiation at room temperature with x rays. To help identify the defects participating in this TL glow curve, a series of EPR measurements that reproduced the TL heating rate were made on the same copper-diffused LiB_3O_5 crystal.

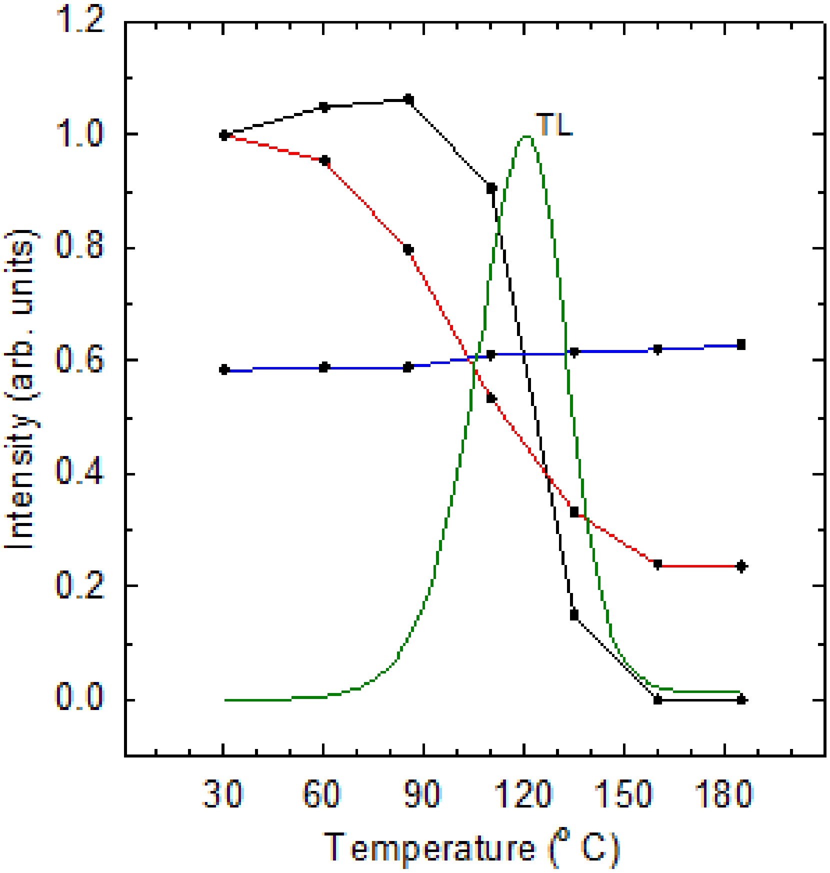

Figure 38. Thermoluminescence (green curve) from the copper-diffused LiB_3O_5 crystal after an irradiation at room temperature with x rays. The TL peak occurs at 120 °C (the heating rate was 1 °C/s). Intensities of the EPR signals from isolated Cu^{2+} ions (red curve), perturbed Cu^{2+} ions (blue curve), and Cu^0 atoms (black curve) were monitored in a separate experiment following a similar irradiation at room temperature with x rays.

After an irradiation at room temperature with x rays, the EPR spectra of the isolated and perturbed Cu^{2+} trapped-hole centers and the Cu^0 trapped-electron centers were monitored during an isochronal thermal anneal. The irradiated copper-diffused LiB_3O_5 crystal was placed in the microwave cavity and the three EPR spectra were taken at 25 K. Next, the sample was moved to a small furnace (preheated to 60 °C) and held at this temperature for 23 s before being returned to the microwave cavity where the EPR spectra were again recorded at 25 K. This incremental process was repeated at 85 °C and again in 25 °C steps above 85 °C with 23 s holding times at each of the elevated temperatures (the equivalent constant heating rate was approximately 1.09 °C/s). Following each heating step, the three EPR spectra were recorded at the 25 K monitoring temperature. Results from these thermal anneals are included in Figure 38. The TL peak intensity and the initial intensities of the isolated Cu^{2+} and the Cu^0 spectra are normalized. The intensity of the perturbed Cu^{2+} spectrum is not normalized; instead, its initial value is set to approximately 60% of the initial intensity of the isolated Cu^{2+} spectrum, thus indicating that the x-ray irradiation initially created more isolated Cu^{2+} ions than perturbed Cu^{2+} ions.

In Figure 38, the intensity of the Cu^0 trapped-electron spectrum increases slightly in the 30-85 °C region and then decreases rapidly in the 85-160 °C region and is completely gone at 160 °C. At 120 °C, the intensity of the Cu^0 EPR spectrum has decreased by half. This thermal decay of the Cu^0 centers correlates very well with the width and peak position of the TL glow curve. In contrast, the intensity of the isolated Cu^{2+} trapped-hole spectrum decreases gradually over the 30-160 °C region. Approximately 23% of these trapped-hole centers remain after the 160 °C anneal step and there is no further decay when the anneal temperature reaches 185 °C. The intensity of the perturbed Cu^{2+} EPR spectrum does not decrease over the 60-185 °C region in Figure 38.

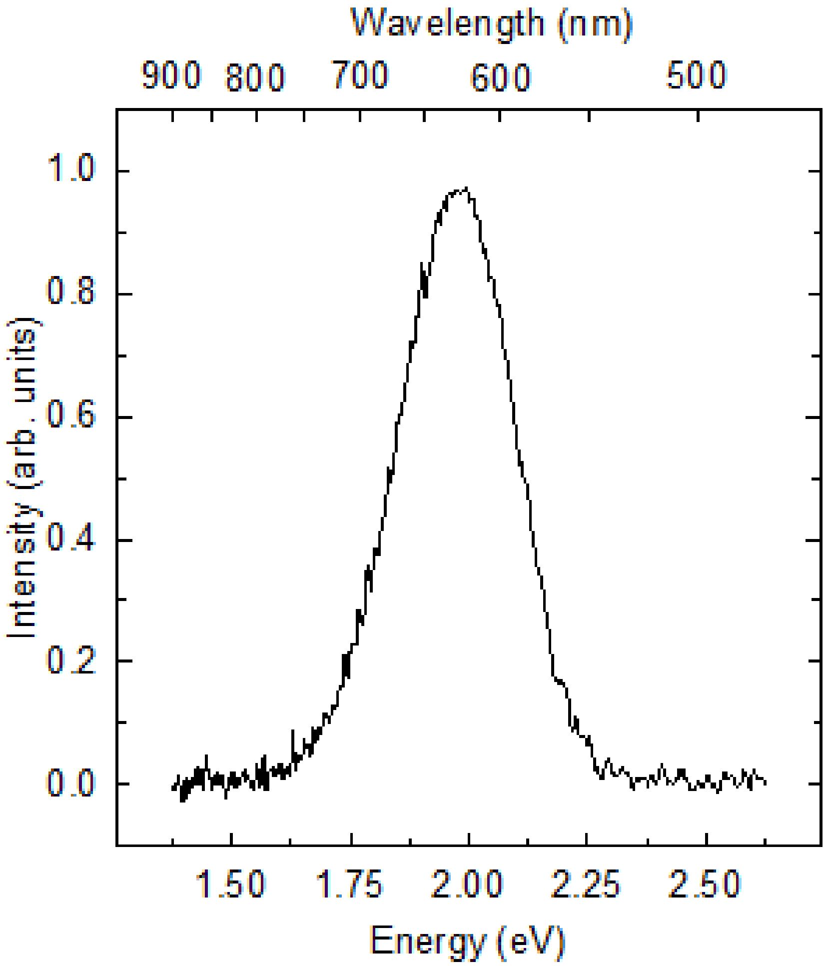

Figure 39. Spectral dependence of the primary emission associated with the 120 °C TL peak from the copper-diffused LiB_3O_5 crystal. This peak in the wavelength dependence occurs at 630 nm.

Figure 39 shows the wavelength dependence of the emitted light associated with the 120 °C TL peak. These data were obtained using a spectrograph and a CCD camera as the sample was heated in a TL experiment. The spectral curve in Figure 39 was collected during a 1.1 s interval of time while the temperature of the sample was near 120

°C (i.e., corresponding to the peak of the TL glow curve). The maximum in this emission spectrum occurs at 630 nm (1.97 eV) and the FWHM of the band is 0.31 eV. Light near 380 nm was not detected when the crystal was at 120 °C.

4. Discussion of the TL mechanism

The early studies [72, 75] of the TL response of copper-doped LiB_3O_5 did not identify the participating electron and hole traps and did not specify a recombination site. Now, however, by combining the results from our EPR, thermal quenching, and spectral-dependence experiments, we have sufficient information to establish the primary physical mechanisms responsible for the TL glow curve peaking at 120 °C in a copper-diffused LiB_3O_5 crystal.

The EPR results in Figure 34, Figure 35, and Figure 38 show that isolated Cu^{2+} ions at Li^+ sites are the active hole traps and that Cu^0 atoms at interstitial sites are the active electron traps. In Figure 38, a portion of the isolated Cu^{2+} ions and all of the perturbed Cu^{2+} ions survive after the temperature reaches 185 °C, whereas all of the Cu^0 atoms disappear by 160 °C. These annealing results, with their 100% change in the Cu^0 spectrum, demonstrate conclusively that the 120 °C TL peak is caused by the thermal release of electrons from Cu^0 centers. If the TL peak were caused by holes being thermally released from isolated Cu^{2+} ions, then the intensity of their EPR signal would be 100% gone after the anneal step at 160 °C. There is a second, and smaller effect, also present in Figure 38. Increases in the intensity of the Cu^0 trapped-electron spectrum and decreases in the intensity of the isolated Cu^{2+} trapped-hole spectrum appear at 60 and 85 °C. We attribute these changes in the Cu^0 and Cu^{2+} spectra in the 60-85 °C range to the thermal release of electrons from singly ionized oxygen vacancies (the released electrons are trapped at interstitial Cu^+ ions to form additional Cu^0 atoms and they recombine with holes at isolated Cu^{2+} ions to restore Cu^+ ions at Li^+ sites).

Thermal quenching results in Figure 33 strongly suggest that the electron-hole recombination site in the TL process is not the isolated Cu^{2+} ions. The $3d^94s^1$ to $3d^{10}$ emission of a Cu^{2+} ion in LiB_3O_5 is completely quenched (i.e., is non-radiative) at 120 °C, and thus they do not contribute to the TL emission. Additional evidence that the electron-hole recombination responsible for the observed emission does not occur at Cu^{2+} ions comes from the 630 nm maximum in the spectral dependence of the TL emitted light (see Figure 39). Annalakshmi et al. [78] recently studied the TL properties of Mn-doped LiB_3O_5 and reported an emission peak near 600 nm. They suggest that Mn^{2+} ions trap holes and convert to Mn^{3+} during an irradiation. Trapped electrons are released during heating and recombine radiatively with the holes at the Mn^{3+} ions (this forms Mn^{2+} ions in an excited state, which then relax to the ground state while emitting 600 nm photons). Similarly, TL investigations of Mn-doped $Li_2B_4O_7$ [8, 85-88] have reported light emission near 580-615 nm. Thus, for our present study, we conclude that the most likely radiative recombination site in the copper-diffused LiB_3O_5 crystal are Mn^{2+} ions at Li^+ sites. In support of this assignment, our EPR spectra show that trace amounts of Mn^{2+} are present in the copper-diffused crystal.

5. Summary

The present investigation describes the behavior of copper ions in LiB_3O_5 crystals. An immediate goal was to establish the basic properties of copper ions in this host lattice, and thus determine the feasibility of using Cu-doped LiB_3O_5 crystals as thermoluminescence-based radiation dosimeters. As part of the study, comparisons were made with Cu-doped $Li_2B_4O_7$ crystals, a known functional radiation-dosimeter material. Except for one important difference, copper ions have similar behaviors in the LiB_3O_5 and $Li_2B_4O_7$ crystals. An irradiation at room temperature with x rays produces Cu^{2+} trapped-hole centers and interstitial Cu^0 trapped-electron centers in both materials. Then, when heated above room temperature, the Cu^0 centers releases the trapped electron and electron-hole recombination takes place at the isolated Cu^{2+} centers. As the electron returns to the Cu^{2+} ion, the excited state $(Cu^+)^*$ is formed which then decays to the Cu^+ ground state. This recombination at the Cu^{2+} ions in $Li_2B_4O_7$ is radiative whereas the recombination at the Cu^{2+} ions in LiB_3O_5 is thermally quenched, and thus nonradioactive. Instead of the expected spectral peak near 380 nm, we observe a peak near 630 nm in LiB_3O_5 for light emitted near the maximum of its 120 °C TL glow curve. This suggests that trace amounts of Mn^{3+} ions, produced by the x rays, serve as the radiative recombination site in the copper-diffused LiB_3O_5 crystal.

The observed strong thermal quenching of Cu-related emission above room temperature suggest that Cu-doped LiB_3O_5 may not be well suited for use as a practical thermoluminescence-based radiation dosimeter. For these devices to be useful, radiative recombination at Cu^{2+} ions is needed to produce an intense TL peak above room temperature.

VII. Silver-doped lithium triborate (LiB3O5) crystals: a photoluminescence, thermoluminescence, and electron paramagnetic resonance study

Abstract

Silver-doped lithium triborate (LiB_3O_5) is a promising candidate material for radiation dosimetry. A similar material, silver-doped lithium tetraborate ($Li_2B_4O_7$) crystals have been shown to have excellent TL and OSL dosimeter properties. Silver-doped lithium triborate crystals, however, have not been studied for dosimetry. In the present investigation, Ag^+ ions ($3d^{10}$) were diffused into an undoped LiB_3O_5 crystal at high temperature (these ions occupy both Li^+ and interstitial positions in the crystal). A photoluminescence (PL) band peaking near 270 nm and a photoluminescence excitation (PLE) band peaking near 225 nm verify that a portion of these Ag^+ ions are located at regular Li^+ sites. After an irradiation at room temperature with x rays, electron paramagnetic resonance (EPR) spectra show that Ag^+ ions at Li^+ sites trap a hole and convert to Ag^{2+} ions ($3d^9$) while Ag^+ ions at interstitial sites trap an electron and converted to Ag^0 atoms ($3d^{10}4s^1$). Two distinct Ag^{2+} trapped-holes are formed after x rays irradiation (one due to isolated Ag^{2+} ions with no nearby defects and the other due to perturbed Ag^{2+} ions). Three Ag^0 trapped-electron EPR spectra are evident after x ray at room temperature. Two slightly different Ag^0 atoms both with hyperfine interactions due to a nearby $I = 3/2$ nucleus, and an additional one Ag^0 atom that shares a trapped-electron with an adjacent Ag^+ ion on a Li^+ site are observed. A rich multi-peak thermoluminescence (TL) glow curve with maxima at 60, 100, 140, 250 and 305 °C

where measured. TL emitted light is composed principally of two emissions, one near 270 nm and another near 630 nm.

1. Introduction

Lithium triborate (LiB_3O_5) is a well-established nonlinear optical material widely used in frequency conversion applications ranging from the mid-infrared to the deep ultraviolet [69-71]. In recent years, this material has also been proposed as a possible candidate for radiation dosimeters [72-78]. While Ag-doped lithium tetraborate ($Li_2B_4O_7$), a similar material, has been shown to be an efficient and sensitive radiation dosimetry material in both TL and OSL modes [6, 9-10, 16, 29], Ag-doped LiB_3O_5 has not been investigated for dosimetry applications. This investigation was undertaken to determine if Ag-doped LiB_3O_5 may be used as an efficient and neutron sensitive dosimetry material in the same manner as Ag-doped $Li_2B_4O_7$.

For dosimetry purposes, a material should have an effective atomic number (z value) as close to tissue equivalence (7.42) as possible [89]. LiB_3O_5 has an effective z value near tissue equivalent at 7.3 [74], while $Li_2B_4O_7$ has an effective z value of 7.23 [89]. Furthermore, unlike most dosimetry materials, LiB_3O_5 and $Li_2B_4O_7$ are intrinsically sensitive to neutrons due to the presence of ^{6}Li and ^{10}B both of which have relatively large thermal neutron absorption cross sections. In fact lithium and boron combine to comprise 44 % and 46 % of the nuclei in LiB_3O_5 and $Li_2B_4O_7$ respectively, and boron comprises 33 % of LiB_3O_5 and 31 % of $Li_2B_4O_7$. The larger number density of boron in LiB_3O_5 makes it potentially more sensitive to neutrons than $Li_2B_4O_7$. In effort to make a neutron sensitive yet gamma blind radiation detector, LiB_3O_5 could be made slightly thinner than $Li_2B_4O_7$ and thus less sensitive to gamma radiation.

Our focus on silver is a result of the unique role played by Ag^+ ions in the TL response of doped $Li_2B_4O_7$. These monovalent ions serve as both hole traps and electron traps during an exposure to ionizing radiation [6]. This diametrically opposite behavior occurs because Ag^+ ions are located at two different sites in the $Li_2B_4O_7$ crystals. When substituting for Li^+ ions, the Ag^+ ions trap holes and become Ag^{2+} ions. The Ag^+ ions also occupy interstitial sites where they trap electrons and become Ag^0 atoms. During subsequent heating after irradiation, electrons are thermally released from Ag^0 centers and recombine with holes at the Ag^{2+} ions. This produces an intense TL signal in $Li_2B_4O_7$ because electron-hole recombination at the Ag^{2+} sites is primarily radiative. Optically stimulated luminescence has also been reported in Ag-doped $Li_2B_4O_7$ [29-30].

In the present paper, we identify the Ag-related electron and hole trapping sites in LiB_3O_5 that are active after exposure to ionizing radiation. Diffusion at 750 °C is used to introduce Ag^+ ($4d^{10}$) ions into a previously grown undoped crystal. The Ag^+ ions occupy both substitutional Li^+ sites and interstitial sites in the LiB_3O_5 crystal. Complementary optical and magnetic resonance characterization techniques are then applied. These are optical absorption, photoluminescence (PL), photoluminescence excitation (PLE), thermoluminescence (TL), and electron paramagnetic resonance (EPR). The PL and PLE results verify that Ag^+ ions are present at Li^+ sites in the diffused crystal. After irradiating at room temperature with x rays, EPR spectra show that Ag^+ ions at Li^+ sites have trapped a hole (Ag^{2+} ions are formed) and Ag^+ ions at interstitial sites have trapped an electron (Ag^0 atoms are formed). Two slightly different silver atom (Ag^0) electron traps are present after x ray irradiation. Pairs of silver ions adjacent to each other, one in an interstitial site and one at a Li site, also trap an electron after x ray irradiation. TL peaks near 100, 250 and 300 °C correspond to electron and hole recombination at silver sites. The TL signal peaks near 275 nm and 630 nm indicating that the recombination sites also include Mn impurities.

2. Experimental

Single crystal lithium triborate (LiB_3O_5) has orthorhombic structure with a space group of Pna21. The lattice constants are a = 8.447 Å, b = 7.3789 Å, and c = 5.1408 Å at room temperature [81-83]. All boron and oxygen sites in LiB_3O_5 are unequal, but all the lithium sites are equivalent. The unit cell consists of 36 atoms which can be divided into four sets of nine atoms that are equivalent after application of crystal symmetry [37]. Helices of $(B_3O_7)^{5-}$ groups are separated by Li^+ cations in the LiB_3O_5 crystal [71]. Each $(B_3O_7)^{5-}$ anionic group has two boron ions that are part of BO_3 units and one boron ion that is part of a BO_4 unit. Figure 40 depicts the basic $(B_3O_7)^{5-}$ anionic unit.

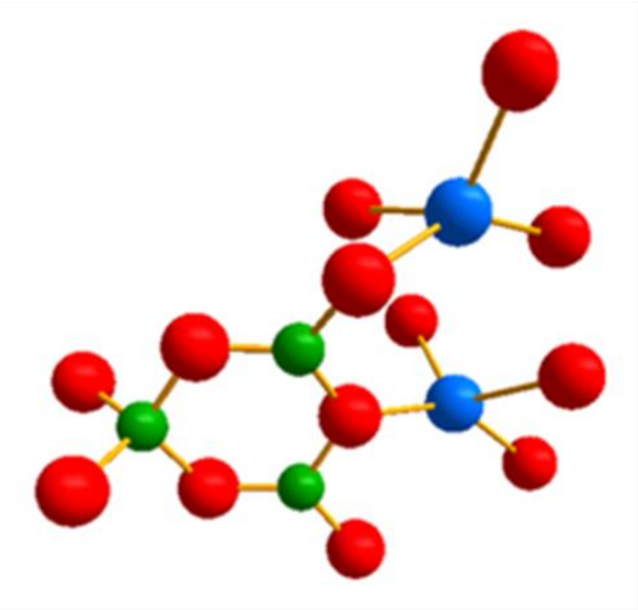

Figure 40. Schematic representation of the basic $(B_3O_7)^{5-}$ anionic group in the LiB_3O_5. This view is along an arbitrary direction in the crystal. Two of the equivalent lithium sites are also shown. Boron ions are green, oxygen ions are red, and the lithium ions are blue.

The sample used in our experiments was rectangular in shape and had nominal dimensions of 2 x 3 x 3 mm^3 along the a, b, and c axes, respectively. Silver was diffused into an undoped LiB_3O_5 crystal by wrapping a single layer of silver foil (0.25 mm thick) around a sample, placing the sample in a one-zone tube furnace and heating to 750 °C in a static air atmosphere. The sample was held at this temperature for 27 h, and then was quickly cooled to room temperature. At temperatures over 700 °C, silver enters the crystal as close-shelled Ag^+ ions and occupies Li^+ sites and interstitial spaces. Size and charge mismatch prevents Ag^+ ions from occupying B^{3+} sites. It is unlikely the silver was uniformly distributed within our diffused crystal. The presence of adjacent interstitial and substitutional Ag ions suggests regions of relatively high Ag concentration most likely near the surface of the crystal, but the intensity of Ag related PL emission suggests light Ag doping overall. Hence, the total doping level remains relatively low while concentration near the surface yields more complex defects than simple isolated silver ions.

A Horiba Fluorolog-3 spectrometer was used to collect the PL and PLE spectra (slits for the excitation and emission monochromators were set at 10 nm resolution). PL spectra were not corrected for system response. A Bruker EMX spectrometer operating near 9.40 GHz was used to collect the EPR spectra. An Oxford helium-gas flow system controlled the temperature of the sample and magnetic fields were measured using a Bruker teslameter. Optical absorption spectra were obtained using a Cary 5000 spectrophotometer. TL "glow curve" and spectral dependence of the TL emission where obtained using an ANDOR Shamrock 193i spectrograph coupled to an iDus 420 CCD camera (the sample was heated at a constant rate of 1 °C/s with an Instec HCS621G stage). An OEG-76H x-ray tube from Varian (operating at 60 kV and 30 mA) was used to convert the Ag^+ ions to Ag^{2+} ions and Ag^0 atoms via x ray irradiation that lasted five minutes.

3. Results

3.1 Photoluminescence (PL and PLE)

A PL emission band peaking near 270 nm (4.59 eV) is observed in Ag^+ diffused LiB_3O_5 when exposed to excitation light of 215 nm. The full width half max of the 270 nm emission is 0.7 eV. The room temperature PLE band is found by monitoring emission at 285 nm. Monitoring the higher emission wavelength provided greater separation from the PL peak, thereby facilitating better resolution of the PLE peak. The

PLE band peaked at 225 nm (5.51 eV) with a full width half max of 0.7 eV. The PL and PLE bands are shown in Figure 41. The Stokes shift is 0.92 eV. The PL and PLE bands at 270 nm and 225 nm were not present prior to diffusion doping of Ag ions into the crystal. We assign the PLE band to the $4d^{10}$ to $4d^{9}5s^{1}$ intracenter transition of Ag^+ ions substituting for Li^+ ions and the PL band to the Stokes-shifted $4d^{9}5s^{1}$ to $4d^{10}$ emission (a two-level configurational coordinate diagram describes this localized excitation and emission). Similar PL and PLE bands have been reported for Ag^+ ions substituting for Li^+ ions in $Li_2B_4O_7$ crystals [7, 10, 16].

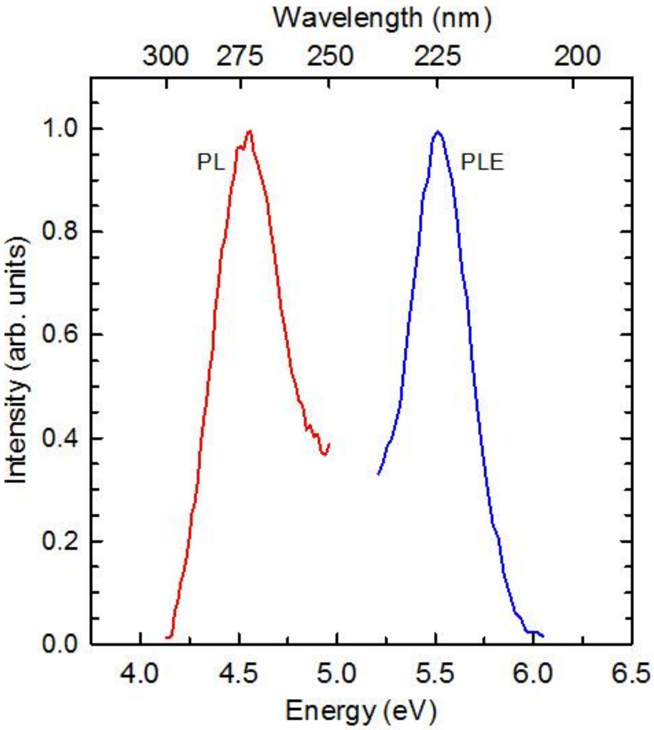

Figure 41. Photoluminescence (PL) and photoluminescence excitation (PLE) spectra from the Ag^+ ions in a silver-diffused LiB_3O_5 crystal. The PL (red curve) was taken with 215 nm excitation and the PLE (blue curve) was obtained by monitoring the emission at 285 nm.

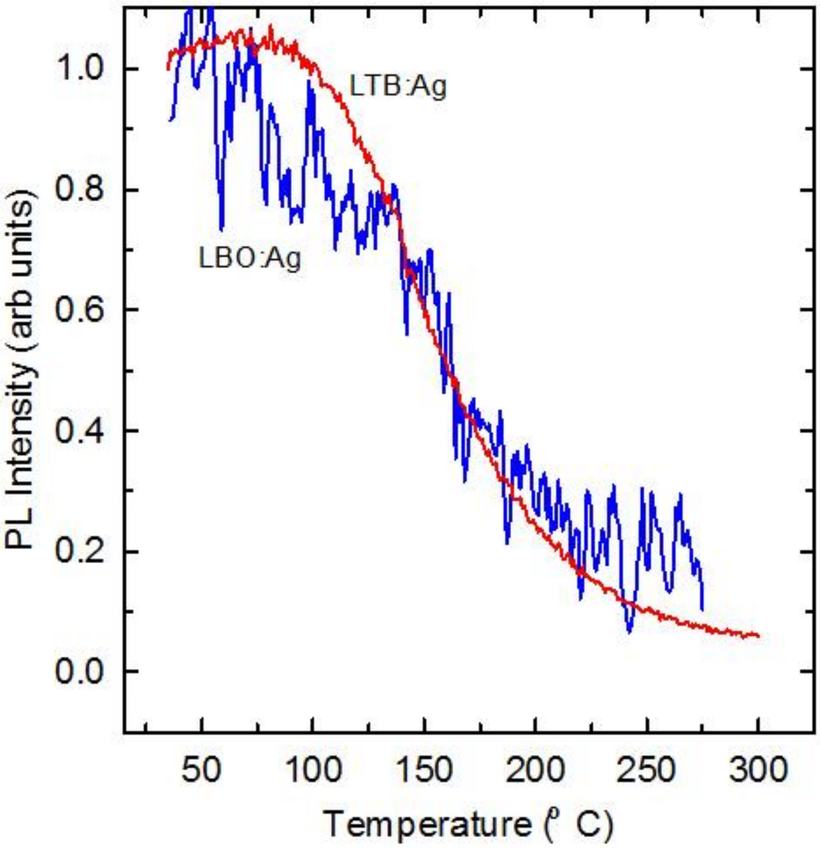

Figure 42. Thermal quenching of the PL emission from Ag^+ ions. A comparison of the silver-diffused LiB_3O_5 crystal (blue curve) and the silver-doped $Li_2B_4O_7$ crystal (red curve). The two curves are normalized at 35 °C.

The intensity of the PL emission band at 270 nm in the silver-diffused LiB_3O_5 crystal was monitored as function of increasing temperature from room temperature up to 275 °C. Figure 42 shows that the 270 nm PL emission in LiB_3O_5 begins quenching near 75 °C, and is about 80% quenched by 175 °C. Data taken under identical conditions from a Ag-doped $Li_2B_4O_7$ crystal are also shown in Figure 42. For this latter crystal, the intensity of the emission at 270 nm from Ag^+ ions [7] was recorded as the temperature was steadily increased. Quenching of the 270 nm emission is identical in the two crystals to within the experimental error.

3.2 Electron Paramagnetic Resonance (EPR)

Room temperature x ray irradiation of silver-doped LiB_3O_5 produces six distinct EPR signals: Ag^{2+} ($4d^9$) ions (two species); Ag^0 ($3d^{10}4s^1$) atoms (three species); and O^- ($1p^9$) ions (lithium vacancies). The x ray irradiation produces "free" electrons and holes which may be trapped at crystal defects creating EPR signals, or recombine in defect free crystal regions. Ag^+ ions substituting for Li^+ ions trap x-ray-liberated-holes forming Ag^{2+} ions in the same manner as in $Li_2B_4O_7$ [6, 13]. Interstitial Ag^+ ions trap electrons after x ray irradiation forming two species of Ag^0 atoms and a single species if Ag^0 atoms adjacent to a substitutional Ag^+ ion. The silver-silver trapped electron and one species of Ag^0 atom is similar to defects in $Li_2B_4O_7$ (see reference [6] and chapter V), while the second Ag^0 atom is similar to the same phenomenon in copper-doped $Li_2B_4O_7$ [11].

Figure 43 shows the EPR spectrum of Ag-doped LiB_3O_5 after irradiation with ionizing radiation at room temperature. The spectrum was taken at 30 K with the magnetic field aligned parallel to the [001] crystal direction. The 25 lines indicated by Ag^0 result from both interstitial Ag^0 species. The 11 lines indicated by $[Ag_i - Ag_{Li}]^0$ are the silver-silver electron trap. These represent 11 of 16 total lines in the EPR spectrum. The two lines near 295 mT are the two species of Ag^{2+}, and the spectrum centered at 335 mT is the isolated-lithium vacancy. The lithium vacancy spectrum is composed of a set of seven hyperfine lines with intensity ration of 1:2:3:4:3:2:1 due a hole trapped at an oxygen ion adjacent to the lithium vacancy equally interacting with two nearby boron nuclei ($I=3/2$). Similar EPR spectra have been observed for lithium vacancy species and self-trapped holes in both LiB_3O_5 and $Li_2B_4O_7$ (see chapter I and references [6, 31, 37, 41].

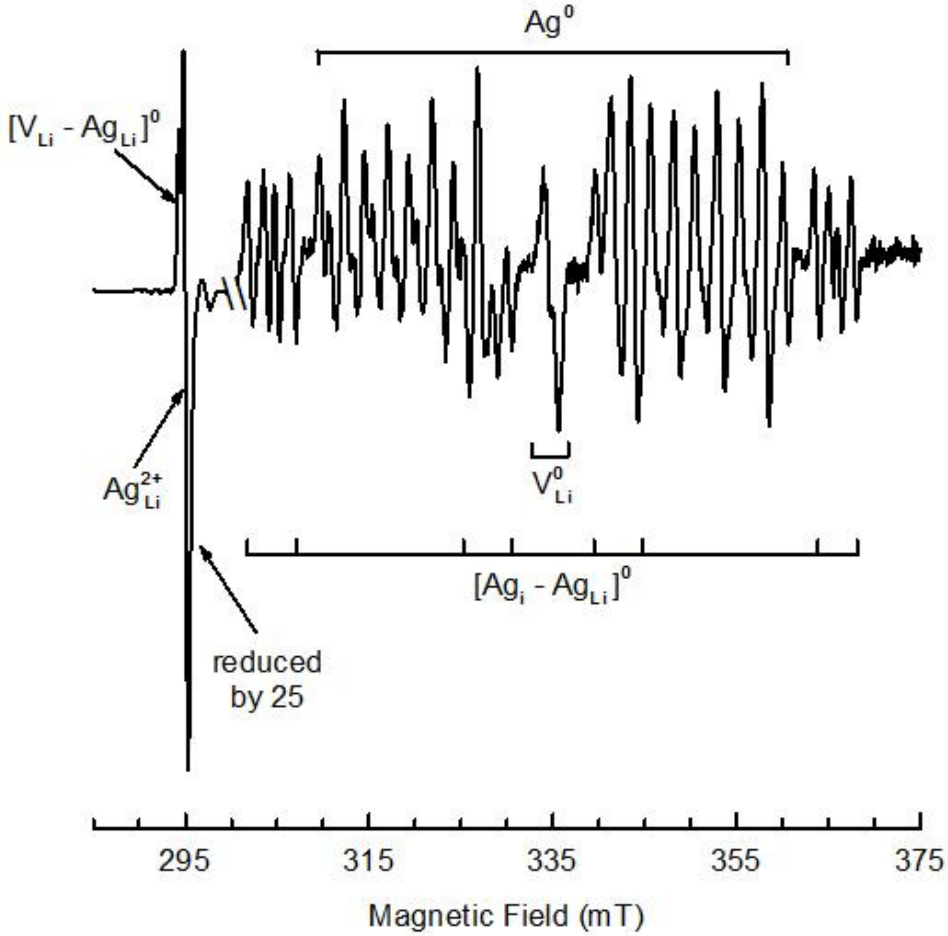

Figure 43. EPR spectrum of silver-doped LiB_3O_5. The EPR spectrum is taken after room temperature x ray irradiation with the magnetic field aligned along the [001] direction. Sample temperature during acquisition was 30 K, and microwave energy was 9.400087 GHz. The left side of the spectrum was reduced 25 times for ease of plotting

3.2.1 Trapped Hole Centers (Ag^{2+} ions)

X ray irradiation at room temperature produces two hole-like centers in Ag-doped LiB_3O_5. Figure 44 shows the EPR spectrum of the two hole-like centers collected at 30

K. The magnetic field was aligned along the [001] direction. Neither center is visible in the EPR spectrum prior to diffusion doping with silver. Both centers are S=1/2, and are a pair of equal intensity lines. In the higher field center, located at 333 mT (g = 2.0164 (±0.0001)), the pair of lines are separated by 1.39 mT, and in the lower field center, located at 330 mT (g = 2.0307 (±0.0001)), the lines are separated by 0.74 mT. The lower field spectrum is approximately one fourth as large as the higher field doublet. Hyperfine interaction with Ag nuclei are responsible for these doublets. Hyperfine spectra for the two silver isotopes, ^{107}Ag and ^{109}Ag, are not resolved due to the relatively small difference in isotopic magnetic moments. ENDOR spectra of the two centers would positively identify silver as the responsible I=1/2 nucleus causing the doublet hyperfine in each center. The unresolved hyperfine for the two S=1/2 centers along with the large positive g shifts lead to the assignment of the centers to two similar Ag^{2+} ions substituting for Li^+ ions in the crystal lattice.

Ag-doped $Li_2B_4O_7$ also contains two hole-like Ag^{2+} centers [6]. In Ag-doped $Li_2B_4O_7$, the two centers are a Ag^{2+} ion on a Li^+ site in an otherwise unperturbed lattice, and a Ag^{2+} ion on a Li^+ site adjacent to a lithium-vacancy ($[V_{Li} - Ag_{Li}{}^{2+}]^0$), see chapter III. In Figure 44, the higher field doublet is labeled $Ag_{Li}{}^{2+}$ while the lower field doublet is labeled $[V_{Li} - Ag_{Li}{}^{2+}]^0$. The lithium vacancy perturbed Ag^{2+} doublet in the $Li_2B_4O_7$ EPR spectrum has smaller intensity like the lower field doublet in Figure 44. Also as in $Li_2B_4O_7$, when x ray irradiated at 77 K, the $[V_{Li} - Ag_{Li}{}^{2+}]^0$ center is not visible in the EPR spectrum for LiB_3O_5. Furthermore, when warmed to room temperature, the $[V_{Li} - Ag_{Li}{}^{2+}]^0$ doublet reappears in the EPR spectrum of both $Li_2B_4O_7$ and LiB_3O_5. For these reasons the lower field doublet is assigned to the $[V_{Li} - Ag_{Li}{}^{2+}]^0$ and the higher field doublet is assigned to isolated $Ag_{Li}{}^{2+}$.

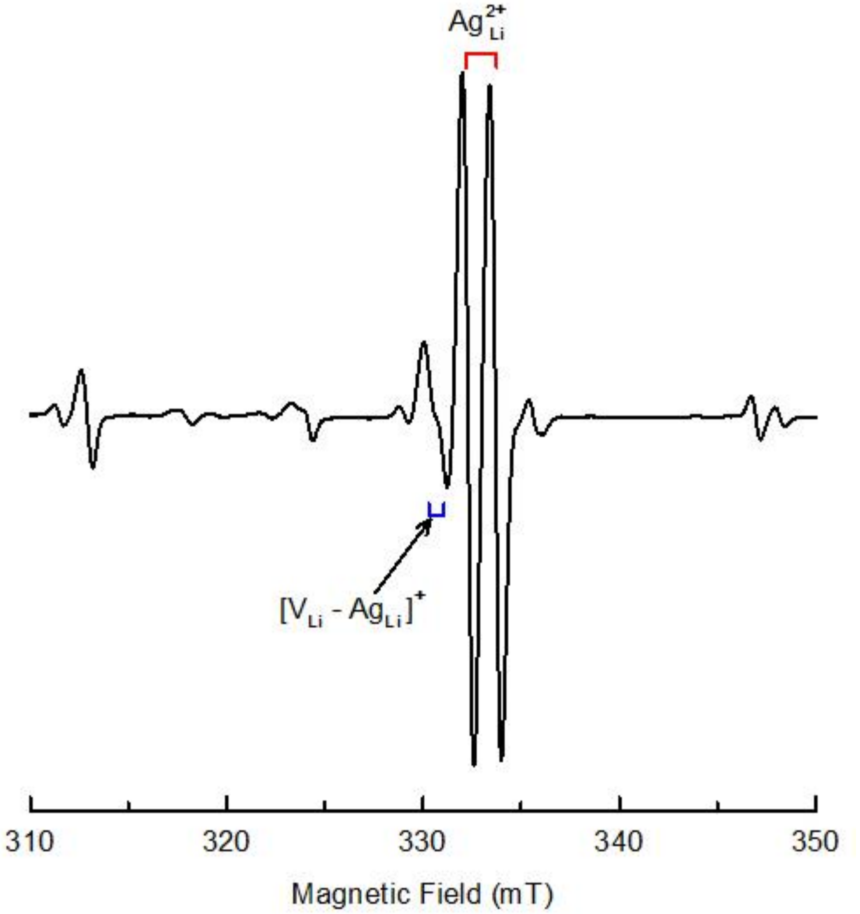

Figure 44. EPR spectra from Ag^{2+} ions in the silver-diffused LiB_3O_5 crystal. Data were taken at 30 K after irradiating the crystal at room temperature with x rays. The magnetic field is along the *b* axis and the microwave frequency is 9.398 GHz. Upper (red) stick diagrams are lines from the isolated Ag^{2+} ions and lower (blue) stick diagrams are lines from Ag^{2+} ions perturbed by a nearby lithium vacancy.

3.2.2 Trapped electron centers

Figure 45 shows the EPR spectra for three separate trapped electron-like S=1/2 centers in Ag-doped LiB_3O_5 after room temperature x ray irradiation. The spectrum was taken with the magnetic field aligned along the [001] direction at 30 K. Spectrum (a) is the experimental spectrum, and spectrum (b) is a simulated spectrum of a $[Ag_i - Ag_{Li}]^0$ trapped electron produced using the EasySpin computer program. Bracketing the top and bottom of spectrum (a) are two sets of stick diagrams. The upper red set of stick diagrams total 16 hyperfine lines representing a set of 8 hyperfine lines for each of the two silver isotopes ^{107}Ag and ^{109}Ag. The two silver isotopes are in nearly 50% abundance (^{107}Ag is 51.83% abundant and ^{109}Ag is 48.17% abundant) resulting in nearly equal intensity spectra for each of the two isotopes. Each of the two silver isotope, I=1/2 diagrams has additional super-hyperfine provided by an I=3/2 nuclei resulting in four lines in the low field and four lines in the high field for both isotopes totaling 16 lines. The I=3/2 isotope could be either ^{11}B or ^{7}Li, both present in the crystal, but the most likely candidate is ^{11}B given similar electron traps in Cu-doped LiB_3O_5, Cu-doped $Li_2B_4O_7$, and Ag-doped $Li_2B_4O_7$ see Chapters III and V and [11]. This ratio of the hyperfine splitting of the ^{107}Ag to ^{109}Ag spectra is 0.8607 which compares favorably to known ratio of the nuclear magnetic moments of the two isotopes of 0.8682. The g_c for the ^{107}Ag isotopes spectrum and the g_c value for the ^{109}Ag isotope spectrum are shifted by 0.16 mT. The difference in the two g_c values is a result of second order effect and the difference in the A_c values for the two isotopes, A_c = 311 mT for the ^{107}Ag isotope, and A_c = 361 mT for the ^{109}Ag isotope. Each of these attributes of this electron-like center is similar to the $[Ag_i - V_{Li}]^-$ trapped electron in Ag-doped $Li_2B_4O_7$, as described in [6] and Chapter V. By analogy, the most likely defect model for this electron like, S=1/2 spectrum is an electron trapped at an interstitial Ag^+ ion yielding an interstitial Ag^0 atom

[6]. It is unknown if the analogy can be extended to the $[Ag_i - V_{Li}]^-$ defect model suggested in Chapter V.

The second set of two stick diagram sets (blue) below spectrum (a) is a second, slightly different version of the same defect represented by the upper red stick diagrams. The g_c for the ^{107}Ag isotopes spectrum and the g_c value for the ^{109}Ag isotope spectrum are shifted by 0.42 mT. Again, the difference in g_c values for the two isotopes is due to second order effect given the relatively large A_c values of 285 mT for the ^{107}Ag spectrum and 328 mT for the ^{109}Ag spectrum. The ratio of the hyperfine splitting of the ^{107}Ag to ^{109}Ag spectra is 0.8674, in good agreement with the known ratio of the two isotopes' nuclear magnetic moments of 0.8682. These two silver interstitial electron trap species are similar to the two species of interstitial copper electron traps in Cu-doped $Li_2B_4O_7$ [11], while Cu-doped LiB_3O_5 displays only one type of interstitial copper electron trap, see chapter VI. It has not been shown that there are two species of interstitial silver electron traps in Ag-doped $Li_2B_4O_7$, but the change in slope in the decay of $[Ag_i - V_{Li}]^-$ trapped electrons at 175 °C in Figure 30 (Chapter V) suggests a second slightly different $[Ag_i - V_{Li}]^-$ may occur in $Li_2B_4O_7$ as well.

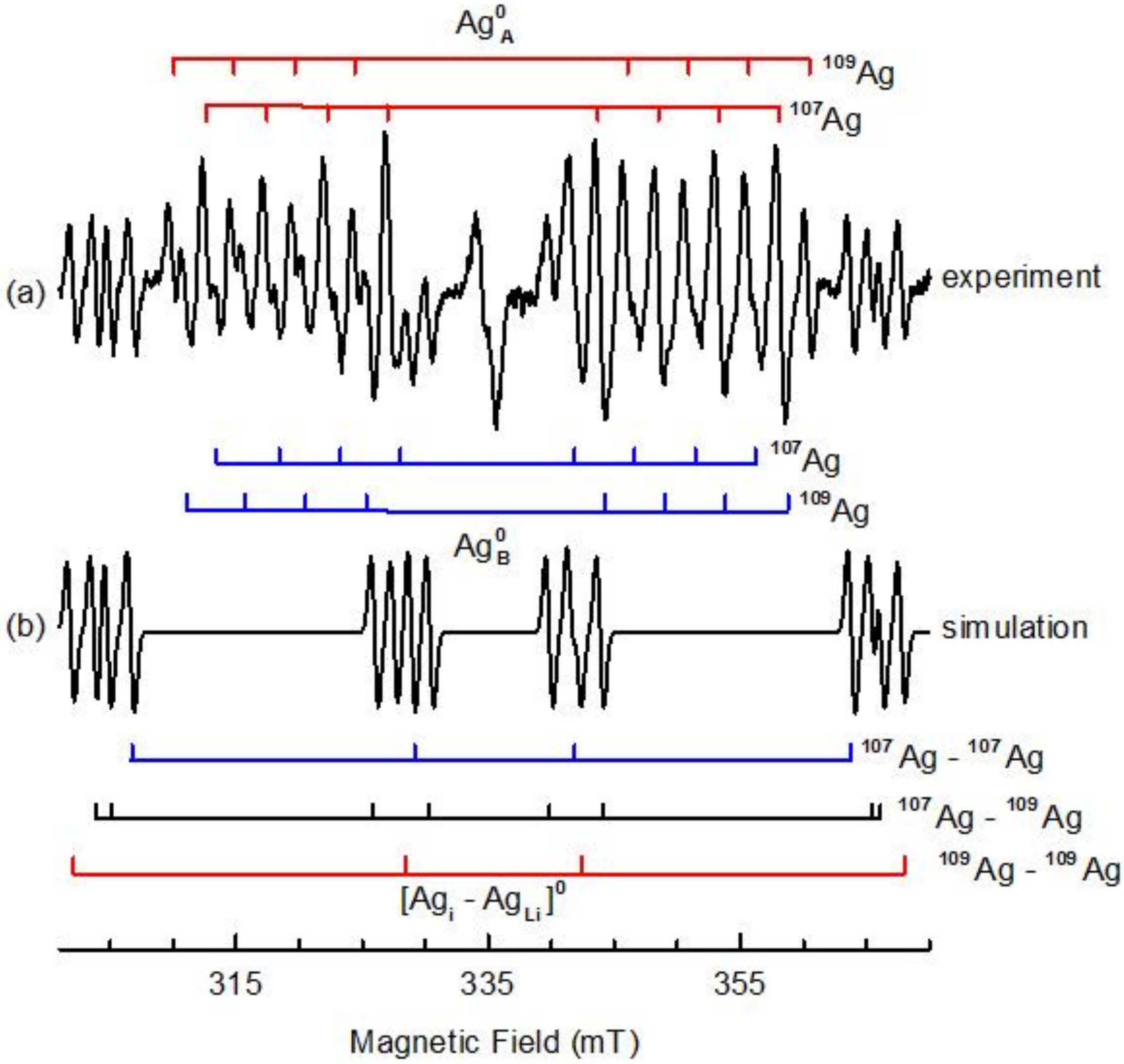

Figure 45. EPR spectrum of trapped electrons in Ag-doped LiB_3O_5. Spectrum (a) taken after room temperature x ray irradiation. Upper (red) stick diagrams are for Ag_A^0 center and lower (blue) stick diagrams are for Ag_B^0 center. Spectrum (b) is a simulation of the $[Ag_i - Ag_{Li}^{2+}]^0$ defect. The top (blue) stick diagram is for the $^{107}Ag - ^{107}Ag$ defect, the middle (black) stick diagram is for the $^{107}Ag - ^{109}Ag$ defect, and the bottom (red) stick diagram is for the $^{109}Ag - ^{109}Ag$ defect. Magnetic field along [001] direction. EPR spectrum taken at 30K with a microwave energy of 9.400087 GHz.

The measured value of the hyperfine parameter for the ^{109}Ag isotope is 1008 MHz for Ag_A^0 and 924 MHz for Ag_B^0 from Figure 45 for the interstitial silver atoms. This is in good agreement with the typical splittings reported for $^{109}Ag^0$ atoms (1300-2100 MHz)

[65]. Most of the unpaired spin is present on the Ag ions. Compared to Morten and Preston's prediction (1831 MHz for Ag) 55 % of the unpaired spin density resides on the Ag ion for Ag_A^0 and 50 % for Ag_B^0 [66-67]. Some of the remaining unpaired spin density resides on the B ion <50 %. The similar defect in Ag-doped $Li_2B_4O_7$ has approximately 50 % of the electron spin density on the Ag ion [6].

Spectrum (b) in Figure 45 is a simulation of an EPR spectrum produced using the EasySpin computer program. The hyperfine spectrum was created by simulating interaction with two unequal silver nuclei. 60.8% of the electron spin density resided on one silver nuclei, and 39.2% of the spin density resides on the other silver nuclei. Natural abundance of each silver isotope is used in the simulation. The A_c value for the silver nuclei with greater spin density is 972.2643 MHz, and the spin density for the silver nuclei with less spin density is 627.182 MHz (A_c values are for the ^{107}Ag isotope). Note that in the high field near 365 mT, and in the low field near 305 mT the simulation is in good agreement with the experimental spectrum including the subtleties of the overlap of individual hyperfine lines. The agreement between simulation and experiment is very sensitive to the relative magnitudes of the two A_c values. A change of a couple tenths of one percent in the relative size of the two hyperfine values results in poor agreement between the simulation and experiment. Near 330 mT and 340 mT, the agreement is not as obvious due to the overlap with the spectra for the interstitial silver atoms. The likely point defect acting as the electron trap is an interstitial silver ion adjacent to a silver ion substituting for a lithium ion, $[Ag_i - Ag_{Li}]^0$.

The extreme outer two lines at high and low field and two lines in the inner sets are due to interaction with two ^{109}Ag nuclei (red stick diagram). While the next two lines at either end (the middle lines in the high and low field sets) and outer two lines in the inner sets are due to interaction with one ^{107}Ag nucleus and one ^{109}Ag nucleus (black stick diagram). Finally, the blue stick diagram represents the lines due to interaction with two ^{107}Ag nuclei.

The ratio of the splitting between the outer $[^{107}Ag_i - {}^{107}Ag_{Li}]^0$ lines and the splitting between the outer $[^{109}Ag_i - {}^{109}Ag_{Li}]^0$ lines is 0.8676, which agrees well with the ratio of the nuclear magnetic moments of ^{107}Ag to ^{109}Ag of 0.8682. This confirms that the hyperfine splitting is due to silver nuclei. In addition, an electron trapped on the Ag ions in the $[Ag_i - Li]^0$ defect ($4d^{10}5s^1$) would not display much angular dependence in the g or hyperfine matrices due to the largely s-orbital nature of the unpaired electron. Indeed, the g matrix is nearly isotropic for the $[^{109}Ag_i - {}^{109}Ag_{Li}]^0$, and the hyperfine matrix shows little variation in a [001] to [100] rotation of the applied magnetic field.

The measured value of the hyperfine parameter for the ^{109}Ag is 1840 MHz from Figure 45. This is in good agreement with the typical splittings reported for $^{109}Ag^0$ atoms (1300-2100 MHz) [65]. Nearly all the unpaired spin is present on the Ag ions. Compared to Morten and Preston's prediction (1831 MHz for Ag) 99 % of the unpaired spin density resides the Ag ion [66-67]. Any additional unpaired spin density may be on oxygen ion surrounding the substitutional Ag ion, but that represents a small portion of the unpaired spin. This suggests an interstitial Ag ion must be involved. The same defect in Ag-doped $Li_2B_4O_7$ has a total spin density of 75 % that resides on the two silver ions, see chapter V.

3.3 Thermoluminescence (TL)

Ag-doped LiB_3O_5 displays a strong thermoluminescence between 30 and 350 °C, see Figure 46, after exposure to ionizing radiation at room temperature. Prior to obtaining the TL data in Figure 46, the sample was x-ray irradiated at room temperature for five minutes. After x-ray irradiation, the sample was immersed in liquid nitrogen until mounted on the Instec stage held at 10 °C. This was done to prevent the fading of emissions below 100 °C prior to obtaining the TL data. The red curve is a 630 nm emission, and the purple curve is a 275 nm emission. These two emissions wavelengths are the only two emission bands in the spectrum of the bulk TL. The combined TL "bulk" glow curve is nearly a sum of the 630 nm and 275 nm emissions. The 630 nm emission may be an emission from electron and hole recombination occurring at Mn impurities in the sample, see chapter VII. The 275 nm emission is likely electron and hole recombination at silver sites in the sample. The TL emission and the Ag-related PL emission, Figure 41, both peak at 275 nm.

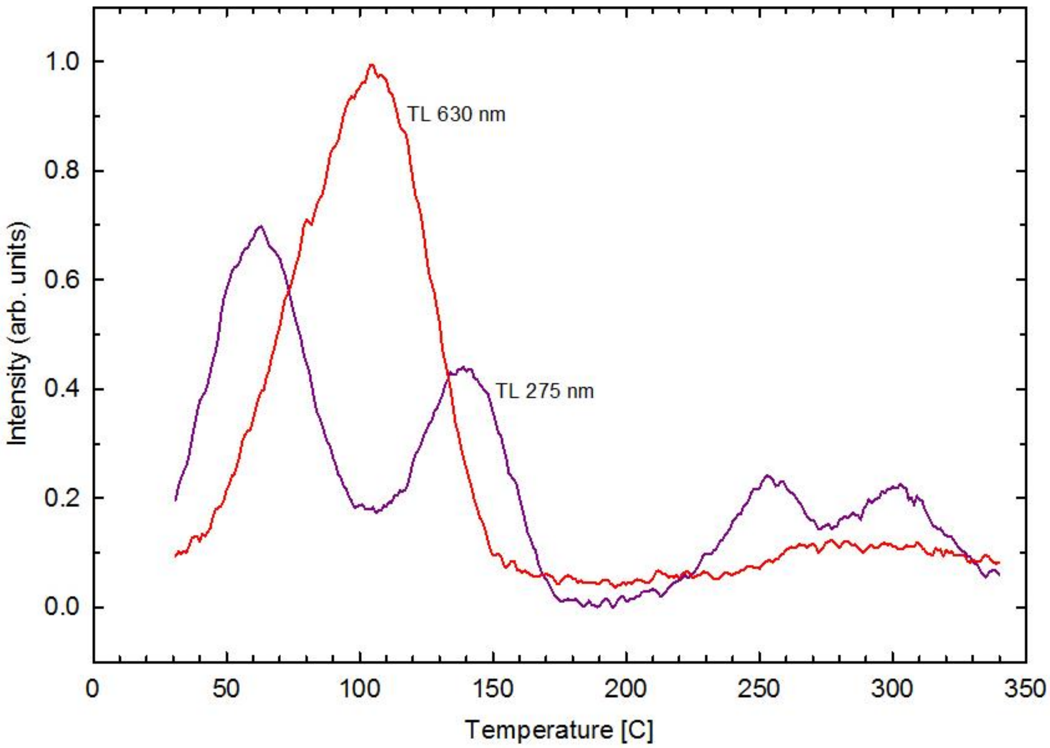

Figure 46. Thermoluminescence from the silver-diffused LiB_3O_5 crystal after an irradiation at room temperature with x rays. The heating rate was 1 °C/s.

In the bulk TL glow curve, the emissions from 30 thru 175 °C combine to form one broad emission. The higher temperature emissions are generally more resolved as separate peaks. The recombination mechanisms for each peak is not yet known, but an isochronal anneal study relating the intensity of EPR spectra, and annealing temperature, as discussed in earlier chapters, should identify the recombination sites active in each TL glow peak.

5. Summary

The present investigation describes the behavior of silver ions in LiB_3O_5 crystals. An immediate goal was to establish the basic properties of silver ions in this host lattice, and thus determine the feasibility of using Ag-doped LiB_3O_5 crystals as thermoluminescence-based radiation dosimeters. As part of the study, comparisons were made with Ag-doped $Li_2B_4O_7$ crystals, a known functional radiation-dosimeter material. Silver ions have similar behaviors in the LiB_3O_5 and $Li_2B_4O_7$ crystals. An irradiation at room temperature with x rays produces Ag^{2+} trapped-hole centers, interstitial Ag^0 trapped-electron centers, and $[Ag_i - Ag_{Li}]^0$ trapped electron centers in both materials. In LiB_3O_5 the room temperature irradiation also produced a second interstitial Ag^0 trapped-electron center not observed in Ag-doped $Li_2B_4O_7$. TL peaks near 100 ℃, 250 ℃ and 300 ℃ with emission peaks at 275 nm and 630 nm are evident. This suggests that the electron hole recombination sites are Ag ions and Mn impurities in silver-diffused LiB_3O_5 crystal. We also observe OSL emission from the Ag-doped LiB_3O_5 crystal when stimulated with light near 400 nm. The results of this study indicate that Ag-doped LiB_3O_5 is a strong candidate to be an efficient and sensitive radiation dosimetry material.

IX. Conclusion

Previously unidentified point defects in Ag-doped $Li_2B_4O_7$ have been investigated. These newly identified defects include lithium vacancy substitutional-silver-ion defect-pairs (hole trap); isolated lithium vacancies (hole trap); isolated oxygen vacancies (electron trap); interstitial-silver-ion substitutional-silver-ion defect pairs (electron trap); isolated interstitial silver ions (electron trap); and interstitial-silver-ion lithium-vacancy defect pairs (electron trap). EPR spectra for each new defect have been identified, and the role of each defect in thermoluminescence and optically stimulated luminescence has been reported. In each case, where available data permitted, defect models have been developed for new and previously reported defects. The combined results of this and previous work suggests that Ag-doped $Li_2B_4O_7$ is a promising candidate material for TL and OSL based radiation dosimetry. Additional work focused on optimizing the combinations of defect types for TL and OSL dosimetry during crystal growth may provide an even more sensitive and efficient dosimetry material with intrinsic neutron sensitivity.

Copper diffused LiB_3O_5 was evaluated for its potential as a radiation dosimetry material based on the similarity with Cu-doped $Li_2B_4O_7$. Copper diffused into the crystal occupied both lithium sites and interstitial sites. The Cu ions on lithium sites trap holes after irradiation with x rays at room temperature, and the Cu ions at interstitial sites trap electrons after irradiation with x rays at room temperature. This dual role for copper is analogous to the same dopant in $Li_2B_4O_7$ an efficient TL dosimetry material. However, in LiB_3O_5, thermal quenching of the Cu^+ PL emission prevents use of the copper doped

LiB_3O_5 as a TL material. The Cu^+ PL emission is thermally quenched prior to the release of electrons from interstitial copper atoms. Any future evaluation of Cu-doped LiB_3O_5 must be based on luminescence mechanisms accessible at temperatures near room temperature (OSL or multiple dopants) to avoid quenching of the Cu^+ emission.

Silver diffused LiB_3O_5 was also evaluated for its potential as a radiation dosimetry material. In this case, the analogy is to Ag-doped $Li_2B_4O_7$. Silver diffused into the crystal occupied both lithium sites and interstitial sites. The Ag ions on lithium sites trap holes after irradiation with x rays at room temperature, and the Ag ions at interstitial sites trap electrons after irradiation with x rays at room temperature. Silver ions also occupy adjacent lithium and interstitial sites which trap electrons after irradiation with x rays at room temperature. In Ag-doped LiB_3O_5, thermal quenching of the Ag^+ PL emission is not the issue it is in Cu-doped LiB_3O_5. Ag-doped LiB_3O_5, therefore, makes a good candidate material for TL based radiation dosimetry. Furthermore, the presence of the OSL mode emission also indicates that OSL based dosimetry is also possible. Further study of Ag-doped LiB_3O_5 should be undertaken to determine the recombination mechanisms for both TL and OSL processes. Additionally, studies should be undertaken to determine the maximum sensitivity of Ag-doped LiB_3O_5 for radiation detection, and optimization of defect types through growth to enhance sensitivity.

Lithium borates doped with silver and/or copper represent promising materials for radiation dosimetry in both TL and OSL modes. The presence of ^6Li and ^{10}B make all lithium borates intrinsically neutron sensitive, and the near tissue equivalent effective atomic number of lithium borates represents an improvement in dosimetry character over presently available OSL materials. The relatively large percent of lithium and boron in lithium borates means that this class of materials will retain neutron sensitivity in relatively thin samples leading to detectors blind to gamma radiation yet still sensitive to neutron radiation. In fact, LiB_3O_5 has a slight advantage over $Li_2B_4O_7$ in this regard. Further study of lithium borates as radiation detecting and dosimetry materials is warranted. In fact, the low mobility of electrons and holes in lithium borates, a product of the large band gaps of these oxide crystals, indicates that the materials may also be useful as imaging materials in radiography, and uniquely in neutron based radiography. This area of research has not yet been undertaken and represents an important area in which lithium borates may be more suited than presently available materials.

Bibliography

[1] M. Takenaga, O. Yamamoto and T. Yamashita, "Preparation of Characteristics of Li2B4O7:Cu Phosphor," *Nuclear Instrumentation and Methods,* vol. 175, pp. 77-78, 1980.

[2] M. Martini, F. Meinardi, L. Kovacs and K. Polgar, "Spectrally Resolved Thermoluminescence of $Li_2B_4O_7$:Cu Single Crystals," *Radiation Protection Dosimetry,* vol. 65, pp. 343-346, 1966.

[3] M. Prokic, "Lithium Borate Solid TL Detectors," *Radiation Measurements,* vol. 33, pp. 393-396, 2001.

[4] N. Can, T. Karali, P. Townsend and F. Yildiz, "TL and EPR Studies of Cu, Ag and P Doped Li2B4O7 Phosphor," *Journals of Physics D: Applied Physics,* vol. 39, no. 10, pp. 2038-2043, 2006.

[5] B. Tiwiri, N. S. Rawat, D. G. Desai, S. G. Singh, M. Tyagi, P. Ratna, S. C. Gadkari and M. S. Kulkarni, "Thermoluminescence Studies on Cu-Doped Li2B4O7 Single Crystals," *Journal of Luminescence,* vol. 130, pp. 2076-2083, 2010.

[6] A. T. Brant, B. E. Kananen, M. K. Murari, J. W. McClory, J. C. Petrosky, V. T. Adamiv, Y. V. Burak, P. A. Dowben and L. E. Halliburton, "Electron and Hole Traps in Ag-Doped Lithium Tetraborate (Li2B4O7) Crystals," *Journal of Applied Physics,* vol. 110, pp. 093719 1-7, 2011.

[7] G. D. Patra, M. Tyagi, D. G. Desai, B. Tiwari, S. Sen and S. C. Gadkari, "Photoluminescence Properties of Cu and Ag Doped Li2B4O7 Single Crystals at Low Temperatures," *Journal of Luminescence,* vol. 132, no. 5, pp. 1101-1105, 2012.

[8] M. Ignatovych, M. Fasoli and A. Kelemen, "Thermoluminescence Study of Cu, Ag and Mn Doped Lithium Tetraborate Single Crystals and Glasses," *Radiation Physics and Chemistry,* vol. 81, no. 9, pp. 1528-1532, 2012.

[9] G. D. Patra, S. G. Singh, A. K. Singh, D. G. Desai, B. Tiwari, S. Sen and S. C. Gadkari, "Growth of Silver Doped $Li_2B_4O_7$ Single Crystals for Dosimetric Application," in *AIP Conf. Proc*, 2013.

[10] G. D. Patra, S. G. Singh, B. Tiwari, S. Sen, D. G. Desai and S. C. Gadkari, "Thermally Stimulated Luminescence Process in Copper and Silver Co-Doped Lithium Tetraborate Single Crystals and Its Implication to Dosimetry," *Journal of Luminescence,* vol. 137, pp. 28-31, 2013.

[11] A. T. Brant, D. A. Buchanan, J. W. McClory, P. A. Dowben, V. T. Adamiv, Y. V. Burak and L. E. Halliburton, "EPR Identification of Defects Responsible for Thermoluminescence in Cu-doped Lithium Tetraborate ($Li_2B_4O_7$) Crystals," *Journal of Luminescence,* vol. 139, pp. 125-131, 2013.

[12] O. Annalakshmi, M. T. Jose, U. Madhusoodanan, B. Venkatraman and G. Amarendra, "Kinetic Parameters of Lihtium Tetraborate Materials," *Journal of Luminescence,* vol. 141, pp. 60-66, 2013.

[13] D. A. Buchanan, M. S. Holston, A. T. Brant, J. W. McClory, V. T. Adamiv, Y. V. Burak and L. E. Halliburton, "Electron Paramagnetic Resonance and Thermoluminescence Study of Ag2+ Ions in $Li_2B_4O_7$ Crystals," *Journal of Physics and Chemistry of Solids,* vol. 75, pp. 1347-1353, 2014.

[14] S. Kar, C. Debnath, S. Verma, V. P. Dhamgaye, G. S. Lodha and K. S. Bartwal, "Themoluminescence Studies on Single Crystal, Polycrustalline and Glass Lithium Tetraborate Samples Irradiated by X-rays from Indus-2," *Physica B: Condensed Matter,* vol. 456, pp. 1-4, 2015.

[15] G. D. Patra, S. G. Singh, A. K. Singh, M. Tyagi, D. G. Desai, B. Tiwari, S. Sen and S. C. Gadkari, "Silver Doped Lithium Tetraborate ($Li_2B_4O_7$) Single Crystals as Efficient Dosimeter Material with Sub-Micro-Gy Sensitivity," *Journal of Luminescence,* vol. 157, pp. 333-337, 2015.

[16] N. S. Rawat, M. S. Kulkarni, M. Tyagi, P. Ratna, D. R. Mishra, S. G. Singh, B. Tiwari, A. Soni, S. C. Gadkari and S. K. Gupta, "TL and OSL Studies on Lithium Borate Single Crystals Doped with Cu and Ag," *Journal of Luminescence,* vol. 132, pp. 1969-1975, 2012.

[17] T. Aydin, H. Demirtas and S. Aydın, "TL/OSL Studies of $Li_2B_4O_7$:Cu Dosimetric Phosphors," *Radiation Meaurements,* vol. 58, pp. 24-32, 2013.

[18] M. S. Kulkarni, M. Luskzik-Bhadra, K. P. Muthe, R. Behrens, N. S. Rawat, A. Soni, D. R. Mishra, S. C. Gadkari, S. K. Gupta and D. N. Sharma, "New OSL Detector Combination for Albedo Neutron Dosimetry," *Radiation Measurements,* vol. 71, pp. 505-508, 2014.

[19] Brookhaven National Laboratory, "Evaluated Nuclear Data File," 15 December 2006. [Online]. Available: http://www.nndc.bnl.gov/exfor/endf00.jsp. [Accessed 18 January 2011].

[20] S. W. McKeever, Thermoluminescence in solids, Cambridge: Cambridge University Press, 1985.

[21] C. C. Klick and J. H. Schulman, "Luminescence in Solids," *Solid State Physics,* vol. 5, pp. 97-172, 1957.

[22] S. G. Gorbics, A. E. Nash and F. H. Attix, "Thermal Quenching of Six Thermoluminescence Dosimetry Phosphors - I," *International Journal of Applied Radiation Isotopes,* vol. 20, pp. 829-841, 1969.

[23] F. Rappaport and J. Lavergne, "Thermoluminescence: Theory," *Jounral of Photosynthesis Research,* vol. 101, pp. 205-216, 2009.

[24] A. J. Bos, "Theory of Thermoluminescence," *Radiation Measurements,* vol. 41, pp. S54-S56, 2007.

[25] F. E. Williams and H. Eyring, "The Mechanism of The Luminescence of Solids," *The Journal of Chemical Physics,* vol. 15, pp. 289-304, 1947.

[26] D. L. Dexter, C. C. Klick and G. A. Russell, "Criterion for Occurence of Luminescence," *Physical Review,* vol. 100, no. 2, pp. 603-605, 1955.

[27] G. B. Beard, W. H. Kelly and M. L. Mallory, "Temperature Dependent Luminescence of CaWO4 and CdWO4," *Journal of Applied Physics,* vol. 33, pp. 144-147, 1962.

[28] S. W. McKeever, "Optically Stimulated Luminescence Dosimetry," *Nuclear Instruments and Methods in Physics REsearch B,* vol. 184, pp. 29-54, 2001.

[29] G. D. Patra, S. G. Singh, B. Tiwari, A. K. Singh, D. G. Desai, M. Tyagi, S. Sen and S. C. Gadkari, "Optically Stimulated Luminescence in Ag Doped $Li_2B_4O_7$ Single Crystal and Its Sensitivity to Neutron Detection and Dosimetry in OSL Mode," *Radiation Measurements,* vol. 88, pp. 14-19, 2016.

[30] B. E. Kananen, E. S. Maniego, E. M. Golden, N. C. Giles, J. W. McClory, V. T. Adamiv, Y. V. Burak and L. E. Halliburton, "Optically Stimulated Luminescence (OSL) from Ag-Doped $Li_2B_4O_7$ Crystals," *Journal of Luminescence,* vol. 177, pp. 190-196, 2016.

[31] M. W. Swinney, J. W. McClory, J. C. Petrosky, S. Yang, A. T. Brant, V. T. Adamiv, Y. V. Burak, P. A. Dowben and L. E. Halliburton, "Identification of Electron and Hole Traps in Lithium Tetraborate ($Li_2B_4O_7$) Crystals: Oxygen Vacancies and Lithium Vacancies," *Journal of Applied Physics,* vol. 107, pp. 113715-1-9, 2010.

[32] J. Krogh-Moe, "The Crystal Structure of Lithium Diborate, $Li_2O.2B_2O_3$," *Acta Crystallographica,* vol. 15, pp. 190-193, 1961.

[33] J. Krogh-Moe, "Refinement of the Crystal Structure of Lithium Diborate, $Li_2O.2B_2O_3$," *Acta Crystallographica,* vol. 24, pp. 179-181, 1968.

[34] N. Sennova, R. S. Bubnova, G. Cordier, B. Albert, S. K. Filatov and L. Isaenko, "Temperature-dependent Changes of the Crystal Structure of $Li_2B_4O_7$," *Z. anorg. allg. Chem,* vol. 634, p. 2601–2607, 2008.

[35] V. T. Adamiv, Y. V. Burak and I. M. Teslyuk, "The Crystal Structure of $Li_2B_4O_7$ Compound in the Temperature Range 10–290K," *Journal of Alloys and Compounds,* vol. 475, no. 1-2, pp. 869-873, 2009.

[36] Y. Ansai, K. Terashima and S. Kimura, "Physical Properties of Molten Lithium Tetraborate," *Journal of Crystal Growth,* vol. 134, pp. 235-239, 1993.

[37] W. Hong, M. M. Chirila, L. E. Halliburton, D. Lupinski, P. Villeval and L. E. Halliburton, "Electron Paramagnetic Resonance and Electron-Nuclear Double

Resonance Study of Trapped-Hole Centers in LiB_3O_5 Crystals," *Physical Review B,* vol. 68, pp. 09411-1-9, 2003.

[38] B. E. Kananen, J. W. McClory, J. C. Petrosky and A. T. Brant, "Characterization of Neutron Induced Defects in Lithium Tetraborate Using Electron Paramagnetic Resonance and Thermoluminescence," *Journal of Radiation Effects, Research and Engineering,* vol. 30, no. 1, pp. 173-177, 2012.

[39] A. T. Brant, D. A. Buchanan, J. W. McClory, V. T. Adamiv, Y. V. Burak, L. E. Halliburton and N. C. Giles, "Photoluminescence from Ag^{2+} Ions in Lithium Tratraborate ($Li_2B_4O_7$) Crystals," *Journal of Luminescence,* vol. 153, pp. 79-84, 2014.

[40] J. A. Huheey, E. A. Keiter and R. L. Keiter, Inorganic Chemistry: Priciples of Stucture and Reactivity, 4th ed., New York: Harper Collins, 1993.

[41] M. P. Scripsick, X. H. Fang, G. J. Edwards, J. K. Tyminski and L. E. Halliburton, "Point Defects in Lithium Triborate (LiB_3O_5) Crystals," *Journal of Applied Physics,* vol. 73, no. 3, pp. 1114-1118, 1993.

[42] K. S. Park, J. K. Ahn, D. H. Kim, H. K. Kim, Y. H. Hwang, D. S. Kim, M. H. Park, Y. Park, J. J. Yoon and J. Y. Leem, "Growth and Properties of $Li_2B_4O_7$ Single Crystals Doped with Cu, Mn and Mg," *Journal of Crystal Growth,* vol. 249, no. 3-4, pp. 483-486, 2003.

[43] D. I. Shahare, B. T. Deshmukh, S. V. Moharil, S. M. Dhopte, P. L. Muthal and V. K. Kondawar, "Synthesis of $Li_2B_4O_7$: Cu Phosphor," *Physica Status Solidi (a),* vol. 141.2, pp. 329-334, 1994.

[44] O. T. Antonyak, V. T. Adamiv, Y. V. Burak and I. M. Teslyuk, "Thermoluminescence of Doped $Li_2B_4O_7$ Single Crystals," *Functional Materials,* vol. 9, pp. 452-455, 2002.

[45] Z. Xiong, Q. Tang and C. Zhang, "Investigation of Thermoluminescence in $Li_2B_4O_7$ Phosphors Doped with Cu, Ag and Mg," *Science in China Series G: Physics Mechanics and Astronomy,* vol. 50, no. 3, pp. 311-320, 2007.

[46] V. M. Holovey, V. I. Sidey, V. I. Lyamayev and P. P. Puga, "Influence of Reducing Annealing on the Luminescent Properties of $Li_2B_4O_7$:Cu Single Crystals," *Journal of Luminescence,* vol. 126, pp. 408-412, 2007.

[47] A. S. Prahdan, R. C. Bhatt and K. G. Vohra, "Some Preparation Parameters of $Li_2B_4O_7$: Cu TLD Phosphor," *Radiochemical and Radioanalytical Letters,* vol. 53, no. 2, pp. 103-110, 1982.

[48] J. K. Srivastava and S. J. Supe, "The Thermoluminescence Characterisation of $Li_2B_4O_7$ Doped with Cu," *Journal of Physics D: Applied Physics,* vol. 22, no. 10, p. 1537, 1989.

[49] B. M. Hunda, T. V. Hunda, P. P. Puga, A. M. Solomon, V. M. Holovey and G. D. Puga, "Concentration and Temperature Dependence for the Copper-doped Lithium Tetraborate Single Crystal," *Journal of Optoelectronics and Advanced Materials,* vol. 1, no. 4, pp. 49-56, 1999.

[50] Y. V. Burak, B. V. Padlyak and V. M. Shevel, "Neutron-Induced Defects in the Lithium Tetraborate Single Crystals," *Radaition Effects and Defects in Solids,* vol. 157, pp. 1101-1109, 2002.

[51] D. Kurali, E. E. Karali, A. Kelemen, V. Holovey, N. Can and T. Karali, "Thermoluminescence Characterization of Ag-doped $Li_2B_4O_7$ Single Crystal Materials," *Luminescence,* 2016.

[52] A. Kelemen, V. Holovey and M. Ignatovych, "Relative Yields of Radioluminescence and Thermoluminescence in Manganese- and Silver-doped Lithium Tetraborate Phosphors," *Radiation Measurements,* vol. 43, pp. 375-378, 2008.

[53] B. E. Kananen, A. T. Brant, D. A. Buchannon, M. K. Murari and J. W. McClory, "Analysis of Neutron Induced Defects in Silver Doped Lithium Tetraborate," in *IEEE Nuclear Science Symposium Conference Record*, Valencia, 2011.

[54] M. Ignatovych, M. Fasoli and A. Kelemen, "Thermoluminescence Study of Cu, Ag and Mn Doped Lithium Tetraborate Single Crystals and Glasses," *Radiation Physics and Chemistry,* vol. 81, no. 9, pp. 1528-1532, 2012.

[55] K. J. Kearfott, W. G. West and M. Rafique, "The Optically Stimulated Luminescnece (OSL) Properties of LiF:Mg,Ti, $Li_2B_4O_7$:Cu, $CaSO_4$:Tm, and CaF_2:Mn Thermoluminescent (TL) Materials," *Applied Radiation and Isoptopes,* vol. 99, pp. 155-161, 2015.

[56] J. Krogh-Moe, "Crystal Structure of Lithium Diborate, $Li_2O.B_2O_3$," *Acta Crystallographica,* vol. 15, pp. 190-193, 1961.

[57] M. M. Islam, V. V. Maslyuk, T. Bredlow and C. Minot, "Structural and Electronic Properties of $Li_2B_4O_7$," *Journal of Physical Chemistry B,* vol. 109, pp. 13597-13604, 2005.

[58] M. S. Holston, I. P. Ferguson, N. C. Giles, J. W. McClory and L. E. Halliburton, "Identification of Defects Responsible for Optically Stimulated Luminescence (OSL) from Copper-diffused $LiAlO_2$ Crystals," *Journal of Luminescence,* vol. 164, pp. 105-111, 2015.

[59] T. Sugawara, R. Komatsu and U. Satoshi, "Linear and NonLinear Optical Properties of Lithium Tetraborate," *Solid State Communications,* vol. 107, no. 5, pp. 233-237, 1998.

[60] A. Kelemen, M. Ignatovych, V. Holovey, T. Vidoczy and P. Baranyai, "Effect of Irradiation on Photoluminescence and Optical Absorption of Spectra of $Li_2B_4O_7$:Mn and $Li_2B_4O_7$:Ag Single Crystals," *Radiation Physics and Chemistry,* vol. 76, no. 8-9, pp. 1531-1534, 2007.

[61] V. T. Adamiv, O. T. Antonyak, Y. V. Burak, M. S. Pudzyrailo and I. M. Teslyuk, "Model od TSL-Centers in $Li_2B_4O_7$:A (A = Cu,Ag) Single Crystals," *Advanced Functional Materials,* vol. 12, pp. 278-280, 2005.

[62] V. S. Osminin, "Photoionization of Silver (0) Centers in Silver-Activated Potassium Chloride," *Soviet Physics Solid State,* p. 1588 [Fiz. Tverd. Tela (Leningrad) 15 (1973) 2386], 1974.

[63] C. Sousa, C. de Graff, F. Illas, M. T. Barriuso, J. A. Aramburu and M. Moreno, "Neutral Atoms in Ionic Lattices: Excited States of KCl:Ag)," *Physical Review B,* vol. 62, pp. 13366-13375, 2000.

[64] R. Valiente, J. A. Aramburu, M. T. Barriuso and M. Moreno, "Electronic Structure of Ag^{2+} Impurities in Halide Lattices," *Journal of Physics: Condensed Matter,* vol. 6, no. 24, p. 4515, 1994.

[65] S. V. Nistor, D. Schoemaker and I. Ursu, "Spectroscopy of ns1-centers in Ionic Crystals," *Physica Status Solidi B,* vol. 185, pp. 9-76, 1994.

[66] J. R. Morton and K. F. Preston, "Atomic Parameters for Paramagnetic Resonance Data," *Journal of Magnetic Resonance,* vol. 30, pp. 577-582, 1978.

[67] J. A. Fitzpatrick, F. R. Manby and C. M. Western, "The Interpretation of Molecular Magnetic Hyperfine Interactions," *Journal of Chemical Physics,* vol. 122, pp. 084312-1-12, 2005.

[68] B. A. Doull, L. C. Oliveira, D. Y. Wang, E. D. Milliken and E. G. Yukihara, "Thermoluminescent Properties of Lithium Borate, Magnesium Borate and Calcium Sulfate Developed for Temperature Sensing," *Journal of Luminescence,* vol. 146, pp. 408-417, 2014.

[69] C. T. Chen, Y. C. Wu, A. D. Jiang, G. M. You, R. K. Li and S. J. Lin, "New Nonlinear-Optical Crystal: LiB_3O_5," *Journal of the Optical Society of America B,* vol. 6, no. 4, pp. 616-621, 1989.

[70] D. N. Nikogosyan, "Lithium Triborate (LBO)," *Applied Physics A,* vol. 58, no. 3, pp. 181-190, 1994.

[71] T. T. Tran, H. Yu, J. M. Rondinelli, K. R. Poeppelmeier and P. S. Halasyamani, "Deep Ultraviolet Nonlinear Optical Materials," *Chemistry of Materials,* vol. 28, no. 15, pp. 5238-5258, 2016.

[72] Z. Ozdemir, G. Ozbayoglu and A. Yilmaz, "Investigation of Thermoluminescence Properties of Metal Oxide Doped Lithium Triborate," *Journal of Materials Science,* vol. 42, pp. 8501-8508, 2007.

[73] T. Depci, G. Ozbayoglu, A. ilmaz and A. N. Yazici, "The Thermoluminescent Properties of Lithium Triborate (LiB_3O_5) Activated by Aluminum," *Nuclear Instruments and Methods in Physics Research B,* vol. 266, pp. 755-762, 2008.

[74] V. E. Kafadar, A. N. Yazici and R. G. Yildirim, "Determination of Trapping Parameters of Dosimetric Thermoluminescent Glow Peak of Lithium Triborate (LiB_3O_5) Activated by Aluminum," *Journal of Luminescence,* vol. 129, pp. 710-714, 2009.

[75] T. Depci, G. Ozbayoglu and A. Yilmaz, "Comparison of Different Synthesis Methods to Produce Lithium Triborate and Their Effects on Its Thermoluminescent Property," *Metallurgical and Materials Transactions A,* vol. 41, no. 10, pp. 2584-2594, 2010.

[76] T. Depci, G. Ozbayoglu and A. Yilmaz, "Synthesis and Thermoluminescence Properties of Rare Earth Oxides (Y, Ce-Lu) Doped Lithium Triborate," *Journal of Rare Earths*, vol. 29, no. 6, pp. 618-622, 2011.

[77] Y. M. Alajerami, S. Hashim, S. K. Ghoshal, D. A. Bradley, M. Mhareb and M. A. Saleh, "Copper Doped Borate Dosimeters Revisited," *Journal of Luminescence,* vol. 155, pp. 141-148, 2014.

[78] O. Annalakshmi, M. T. Jose and B. Venkatraman, "Dosimetric Characteristics of Manganese Doped Lithium Triborate Thermoluminescent Material," *journal of Luminescence,* vol. 179, pp. 241-247, 2016.

[79] A. Kelemen, D. Mesterhazy, M. Ignatovych and V. Holovey, "Thermoluminescence Characterization of Newly Developed Cu-Doped Lithium Tetraborate Materials," *Radiation Physics and Chemistry,* vol. 81, no. 9, pp. 1533-1535, 2012.

[80] E. Cruz-Zaragoza, C. Furetta, J. Maracazzo, M. Santiago, C. Guarneros, M. Pacio and R. Palomino, "Beta Radiation Induced Luminescence of Polycrystalline Cu-Doped Li2B4O7," *Journal of Luminescence,* vol. 179, pp. 260-264, 2016.

[81] Y. F. Shepelev, R. S. Bubnova, S. K. Filatov, N. A. Sennova and N. A. Pilneva, "LiB_3O_5 Crystal Structure at 20, 227 and 377 °C," *Journal of Solid State Chemistry,* vol. 178, no. 10, pp. 2987-2997, 2005.

[82] C. Le Henaff, N. K. Hansen, J. Protas and G. Marnier, "Electron Density Distribution in LiB_3O_5 at 293 K," *Acta Crystallographica Section B,* vol. 53, pp. 870-879, 1997.

[83] S. F. Radaev, B. A. Maximov, V. I. Simonov, B. V. Andreew and V. A. Dyakov, "Deformation Density in Lithium Triborate, LiB_3O_5," *Acta Crystallographica Section B,* vol. 48, pp. 154-160, 1992.

[84] W. Hong, N. Y. Garces, M. M. Chirila and L. E. Halliburton, "Identification of Point Defects Responsible for Laser-Induced Ultraviolet Absorption in LiB_3O_5 (LBO) Crystals," in *SPIE Proccedings 4932*, 2003.

[85] A. Ozdemir, Z. Yegingil, N. Nur, K. Kurt, T. Tuken, T. Depci, G. Tansug, V. Altunal, V. Guckan, G. Sigircik, Y. Yu, M. Karatasli and Y. Dolek, "Thermoluminescence Study of Mn Doped Lithium Tetraborate Powder and Pellet Samples Synthesized by Solution Combustion Synthesis," *Journal of Luminescence,* vol. 173, pp. 149-158, 2016.

[86] O. Annalakshmi, M. T. Jose, U. Madhusoodanan, J. Sridevi, B. Venkatraman, G. Amarendra and A. B. Mandal, "Radiation-Induced Defects in Manganese-Doped Lithium Tetraborate Phosphor," *Radiation Protectin Dosimetry,* vol. 163, no. 1, pp. 14-21, 2015.

[87] V. Nagirnyi, E. Aleksanyan, G. Corradi, M. Danilkin, E. Feldbach, M. Kerikmae, A. Kotlov, A. Lust, K. Polgar, A. Ratas, I. Romet and V. Seeman, "Recombination Luminescence in $Li_2B_4O_7$ Doped with Manganese and Copper," *Radiation Measurements,* vol. 56, pp. 192-195, 2013.

[88] V. M. Holovey, K. P. Popovich, D. B. Goyer, V. M. Krasylynets and A. V. Gromonnai, "Spectral Dependences of Thermally Stimulated Luminescence and X-ray Luminescence of Single-Crystalline and Glassy $Li_2B_4O_7$:Mn," *Radiation Effects and Defects in Solids,* vol. 166, no. 7, pp. 522-528, 2011.

[89] C. A. Jayachandran, "Calculated Effective Atomic Number and Kerma Values for Tissue-Equivalent and Dosimetry Materials," *Physics in medicine and biology,* vol. 16, no. 4, pp. 617-623, 1971.

REPORT DOCUMENTATION PAGE	*Form Approved* *OMB No. 074-0188*

1. REPORT DATE *(DD-MM-YYYY)* 14-09-2017	**2. REPORT TYPE** Ph.D. Dissertation	**3. DATES COVERED** *(From – To)* Oct 2014 – Sep 2017

4. TITLE AND SUBTITLE Luminescence in Lithium Borates	**5a. CONTRACT NUMBER** **5b. GRANT NUMBER** **5c. PROGRAM ELEMENT NUMBER**
6. AUTHOR(S) Kananen, Brant E., Lieutenant Colonel, USA	**5d. PROJECT NUMBER** **5e. TASK NUMBER** **5f. WORK UNIT NUMBER**
7. PERFORMING ORGANIZATION NAMES(S) AND ADDRESS(S) Air Force Institute of Technology Graduate School of Engineering and Management (AFIT/EN) 2950 Hobson Way, Building 640 Wright-Patterson AFB, OH 45433-7765	**8. PERFORMING ORGANIZATION REPORT NUMBER** AFIT-ENP-DS-17-S-027
9. SPONSORING/MONITORING AGENCY NAME(S) AND ADDRESS(ES) POC: MAJ Andrew Decker (andrew.decker.mil@mail.mil) Defense Threat Reduction Agency 8725 John J. Kingman Rd Ft. Belvoir, VA 22060	**10. SPONSOR/MONITOR'S ACRONYM(S)** DTRA **11. SPONSOR/MONITOR'S REPORT NUMBER(S)**

12. DISTRIBUTION/AVAILABILITY STATEMENT
Distribution Statement A. Approved for Public Release; Distribution Unlimited

13. SUPPLEMENTARY NOTES
This material is declared a work of the U.S. Government and is not subject to copyright protection in the United States.

Spectrometry methods are used to identify and characterize point defects in single crystals of lithium tetraborate ($Li_2B_4O_7$) and lithium triborate (LiB_3O_5) doped with silver or copper, and explore the role of these point defects in luminescence. New defects are identified in Ag-doped including: lithium vacancy substitutional-silver-ion defect-pairs (hole trap); isolated lithium vacancies (hole trap); isolated oxygen vacancies (electron trap); interstitial-silver-ion substitutional-silver-ion defect pairs (electron trap); isolated interstitial silver ions (electron trap); and interstitial-silver-ion lithium-vacancy defect pairs (electron trap). Defect models are proposed, and adjustments made to defect models known defects.

Defects in Ag-doped LiB_3O_5 and Cu-doped LiB_3O_5 are identified including: two species of interstitial-silver-ions (electron traps); isolated-substitutional-silver-ion (hole trap); lithium vacancy substitutional-silver-ion defect pairs (hole trap); interstitial-silver-ion substitutional-silver-ion defect pairs (electron trap); a species of interstitial-copper-ion (electron trap); isolated-substitutional-copper-ion (hole trap); and lithium vacancy substitutional-copper-ion defect pairs (hole trap). Based on this assessment, Ag-doped LiB_3O_5 is a promising TL and OSL dosimetry material while Cu-doped LiB_3O_5 is not.

15. SUBJECT TERMS
Lithium Tetraborate, Lithium Triborate, Electron Paramagnetic Resonance, Luminescence

16. SECURITY CLASSIFICATION OF:			**17. LIMITATION OF ABSTRACT**	**18. NUMBER OF PAGES**	**19a. NAME OF RESPONSIBLE PERSON** Dr. John W. McClory
a. REPORT	**b. ABSTRACT**	**c. THIS PAGE**			**19b. TELEPHONE NUMBER** *(Include area code)*
U	U	U	UU	151	(937)255-6565 x7308

Standard Form 298 (Rev. 8-98)
Prescribed by ANSI Std. Z39-18